DIODE LASER GAS SENSING FOR HIGH-SPEED TEMPERATURE AND SPECIATION MEASUREMENTS INSIDE EXPLOSIVE FIREBALLS

BY

CHRISTOPHER M. MURZYN

DISSERTATION

Submitted in partial fulfillment of the requirements
for the degree of Doctor of Philosophy in Mechanical Engineering
in the Graduate College of the
University of Illinois at Urbana-Champaign, 2018

Urbana, Illinois

Doctoral Committee:

Professor Nick G. Glumac, Chair
Professor Tonghun Lee
Assistant Professor Kelly Stephani
Professor Gregory S. Elliot

ABSTRACT

There is a need for fundamental science to defeat weapons of mass destruction. Prompt bioagent defeat strategies invoke energetic materials to generate spore killing temperatures and halogen compounds. Developing predictive models for the bioneutralization efficiency of materials requires accurate experimental data to underpin the computational efforts. Certain thermodynamic parameters such as pressure are easily obtained in explosively driven flows. The temperature and chemistry of the interior of post-detonation fireballs is largely unmeasured at the current time.

The present work was carried out in order to develop, demonstrate, and transfer technologies for making cost effective, high-speed, quantitative measurements of temperature and chemical speciation in near-field, post-detonation fireballs. This document presents the details of a hardened gauge that enables the fielding of a wide variety of proven tunable diode laser absorption techniques in explosive applications. In addition, details of the theory, application, and data analytics for the relevant spectroscopic measurements are also addressed.

The developed hardware and technique were used to measure temperature at 30 kHz in chambered explosive fireballs by sweeping a tunable diode laser over a water vapor absorption band in the near infrared spectrum. Additional efforts were made to characterize the multiphase temperature of explosive fireballs. In addition to measuring temperature, a second tunable diode laser diagnostic was interfaced with the probe to measure atomic iodine in explosive fireballs as it is a halogen useful in agent defeat applications.

Test data presented in this document were collected at a variety of scales ranging from milligrams of spark ignited thermites in a 2-liter chamber, to 10s of grams of aluminized, plastic explosives in an 1800-liter chamber. All data validate the ability of the combined probe and data analytics to survive the implicitly destructive intensity of explosive detonation and make high-speed optical measurements of temperature and atomic iodine concentration inside explosive fireballs.

ACKNOWLEDGEMENTS

First and foremost, I would like to thank my family for their relentless support throughout the entirety of my education. There is no doubt in my mind that I would not have been able to accomplish what I have without your love and presence in my life. Since the beginning, you have taught me the value of an education and showed me the value of work ethic. Thank you.

I would also like to extend a special thank you to Michael Clemenson, Mike Soo, and Joe Kalman. I'm truly grateful for our personal and professional relationships that have extended well beyond our time in graduate school.

Additionally, I would also like to thank the many other graduate students who I have worked in the lab with during my tenure in school. Thank you to Jon Retter, Jose Guadarrama, Chee Haw Chan, Dave Amondson, Emily Weerakkody, Nick Poirier, Brian Read, Rylie Lodes, Joel Schwallier, Jeff Shen, David Allen, and Lance Kingston. A number of extraordinary undergraduates also merit recognition on this page. Thank you to Thomas Skeels, Harrison Greenwood, and Ajay Krish.

This past year, I was afforded the opportunity to work with an extraordinary engineer, Dr. Adam Sims. I am incredibly grateful for your support, encouragement, and mentoring. I would also like to thank Emeritus Professor Herman Krier for his constant encouragement and collegiate insight.

Finally I would like to thank my research advisor, Professor Nick Glumac. Words of gratitude here feel trite. When I started working for you over six years ago, I had no idea of the transformative journey that I was beginning. Sharing your passion for research, instilled in me a scientific curiosity that I will never give up. Thank you for your support, guidance, and this unparalleled education.

This work was supported the Defense Threat Reduction Agency (DTRA) under contract HDTRA1-14-1-0033. The program manager is Dr. Allen Dalton. Additional support was provided by the Naval Surface Warfare Center, Indian Head (NSWC-IH), and the Air

Force Research Laboratory at Eglin AFB under contract FA8651-16-1-0012. James Lightstone, Su Peiris and Stephanie Johnson are the program managers.

for my parents, Patrick and Cheryl

TABLE OF CONTENTS

CHAPTER 1: INTRODUCTION, MOTIVATION, AND OVERVIEW

At the forefront of explosives and energetic materials research is the desire to predictively model warhead performance with computational techniques. The complexity of building accurate models that can characterize explosive detonation and target interaction is an extraordinary feat in and of itself. Comprehensive models will need to account for shock physics, fluid mechanics, multiphase heat and mass transfer, and even the chemistry of reacting flows. As is common across nearly all science and engineering specialties, predictive models must be derived from and verified against experimental measurements and observation.

The common goal of developing these models incites an exceptionally productive collaboration between industry, government, and academia. It brings together specialists and resources from all three to address the mutual need to uncover the fundamental physics and chemistry that governs explosive detonations and the subsequent post-detonation environment. In many explosive applications, the key metrics of importance are the blast (peak pressure) and the impulse (integrated positive phase overpressure) due to their correlation with damage capability [1]. Conversely in the counter-weapon of mass destruction community (C-WMD), the temperature and chemistry of the post-detonation fireball is of prime importance.

The potential of biological attacks from actors of concern has been and continues to be a real threat to the United States of America [2, 3]. For this reason, the Defense Threat Reduction Agency (DTRA) has identified the need for research into the basic science to defeat weapons of mass destruction (WMD) [4]. This involves investigating the ability of explosives and reactive materials to evolve spore killing temperatures and halogen compounds [5]. Conceptually, the detonation of a C-WMD device would couple a prompt thermal defeat mechanism with a long-duration thermochemical one for enhanced spore lethality. In addition to being highly efficient, this defeat strategy needs to avoid further dispersal of any surviving biological agent.

Temperature is such a critical metric inside the explosive fireball due its multidimensional effects. The first order effect is the direct, thermal defeat of biological spores [6]. The second order effect is its governance on both equilibrium speciation and kinetic reaction rates which will dictate the halogen behaviors. Unlike pressure, which has a relatively simple means of collection with piezoelectronics, characterizing the undisturbed temperature and speciation at explosive-relevant time scales requires much more intricate diagnostics. The present work details the diagnostic research and development that was conducted to provide optical techniques for the experimental characterization of post-detonation fireballs.

As for the thermochemical process, much of the recent work in the counter weapon of mass destruction (C-WMD) community has converged on iodine as a probable bio-agent defeat compound [7, 8, 9, 10]. Atomic, molecular, and hydrogenated iodine are all known to have biocidal properties. Iodine also has desirable thermophysical properties such as high vapor pressure for an enduring presence. Balancing the benefits of increased energy for higher temperatures against increased iodine delivery for elevated halogen concentration begets parametric analysis of iodized energetic materials for this application. While other labs are addressing this issue, the Energetic Materials Diagnostics Lab at UIUC is working on the challenge of quantifying material performance by time-resolved temperature and halogen generation.

It can be seen in the Gordon-McBride equilibrium simulation shown in Figure 1 that the overwhelming iodine-containing species in a dilute mixture of moist air will occur in either molecular or atomic form [11]. Another notable behavior in this family of curves is that the transition from nearly entirely molecular to entirely atomic iodine takes place in between 650 and 1250 Kelvin centered around 900 Kelvin. Imagining this transition in the context of a cooling explosive cloud suggests that the presence of atomic iodine will be transient as venting and heat transfer leach energy out of the products. This qualitative scenario is subject to the assumptions of sufficiently fast kinetics to reach equilibrium. Simultaneous experimental measurement of temperature and speciation will be able to confirm the validity of equilibrium assumptions.

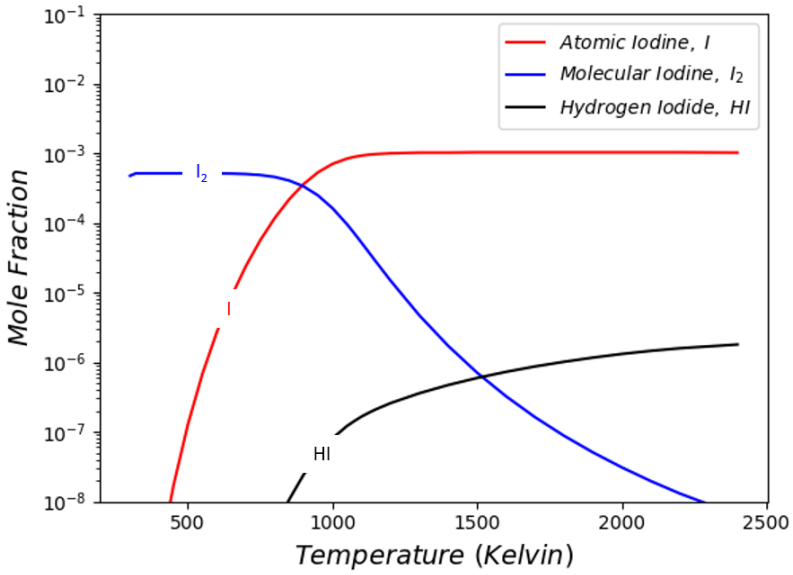

Figure 1: Quantitative equilibrium speciation for the three most concentrated forms of iodine. Simulation is isobaric at 1 atm. with initial relative masses of 10g I_2, 10g H_2O, and 2205 grams dry air. These masses were chosen as an approximate experimental range for tests to be conducted in the 1800-liter blast chamber.

In addition to providing insight as to the range of temperatures where chemical speciation is a strong function thereof, the equilibrium mole fraction will guide the diagnostic design. It is evident that the detection limits should be on the order of 10 ppm to 1000 ppm for explosive testing in an 1800-liter blast chamber according to the model.

There are numerous ways of introducing iodine into an explosive event. One option for producing iodine is through the addition of aluminum (Al) and iodine pentoxide (I_2O_5) thermite. A simple energy balance of this thermitic reaction is compared to the more common reaction of aluminum and molecular oxygen in Reaction 1 and Reaction 2 respectively. Although not the most energetic or most halogenated, working with a stable form of iodine such as that contained in an oxide has operational advantages over options such as pure iodine crystals or diiodomethane.

Reaction 1: Aluminum and Iodine Pentoxide

$$10Al(s) + 3I_2O_5(s) \rightarrow 5Al_2O_3(s) + 3I_2(g)$$

$$\Delta H_{rxn} = -6.04\ kJ/g\ reactants$$

$$\Delta H_{rxn} = -28.44\ kJ/g\ Al$$

Reaction 2: Aluminum and Molecular Oxygen

$$4Al(s) + 3O_2(g) \rightarrow 2Al_2O_3(s)$$

$$\Delta H_{rxn} = -16.43\ kJ/g\ reactants$$

$$\Delta H_{rxn} = -31.05\ kJ/g\ Al$$

The heat of formation for solid alumina (Al_2O_3) was taken as -1,675.69 kJ/mol [12]. The enthalpy of formation for iodine pentoxide was taken as -172.35 kJ/mol which is the average of the three values reported by M.W. Chase [13]. Molecular iodine gas was taken to have an enthalpy of formation of 62.42 kJ/g. The reason for comparing the two reactions side by side is that this highlights the tradeoff in energy per unit mass of reactants that have to be carried in a payload. Carrying the oxidized iodine as a necessary reactant significantly drops the energy density of the payload, especially considering the oxygen in aerobic aluminum combustion will come from the surrounding environment.

The culminating challenge being addressed is the need to probe the inside of the explosive fireball. Almost no techniques exist for measuring the temperature and speciation inside an explosive fireball. Robust thermocouples suffer from slow response times. Surface temperature of explosive fireballs has been successfully measured through numerous emission techniques [14, 15]. In addition to the standard assumptions of excited state equilibrium conditions, these measurements are also limited to characterizing the explosive fireball up to the attenuation length scale. This dimension can be on the order of centimeters in some cases [16]. The challenge with standoff techniques is illustrated in Figure 2.

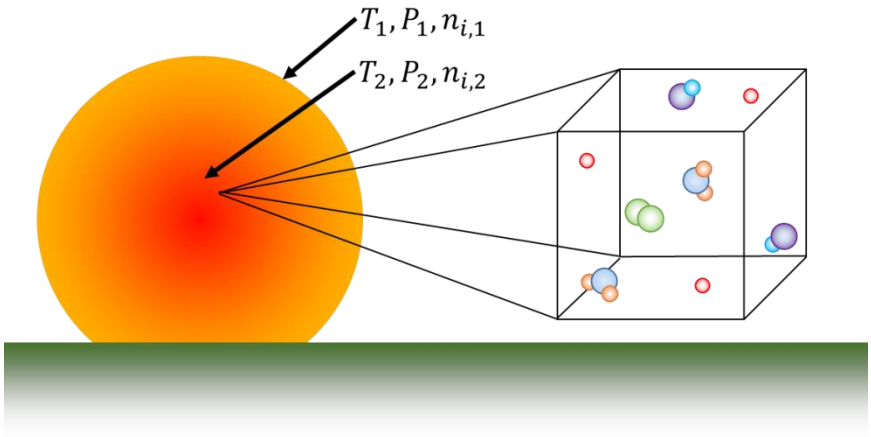

Figure 2: Illustration of the gradient of thermodynamic properties across the expanse of the fireball.

Although pyrometric techniques demonstrate impressive temporal resolution and have been fielded inside of explosive fireballs, there is uncertainty as to whether these measurements characterize condensed or gas phase species in the event [17]. To explicitly measure gas phase temperature inside of explosive fireballs, an optical probe was designed to survive the inherently destructive blast wave and be engulfed in the post-detonation gases. The goal is to measure and model the environment which the spores will be exposed to. This can be done with the highest degree of confidence and accuracy using spectroscopic techniques.

Temperature measurement in combustion scenarios is by no means a nascent science. There are an extraordinary number of techniques available, each with their own pros and cons. Lewis et al. presents a wonderful synopsis on the subject in his compendium of state-of-the-art temperature measurement approaches [18]. Another comprehensive overview of techniques was compiled by Childs et al. [19]. Temperature measurement in explosively driven combustion is a notably niche space that renders some of these techniques more useful than others.

One of the most commonly seen techniques in fireball temperature measurement is the use of thermocouples. The most appealing aspect of this approach is the simplicity of the technique. Thermocouples function by the measuring the change in electrical resistance across a bimetallic interface. The resistance change is a function of the metal temperature which is governed by the gases, liquids, and solids in contact with the interface. Different

metals will provide access to different temperature ranges, typically with a small tradeoff between range and accuracy. Even with the tradeoff, the accuracy of thermocouples is typically very high. This can be a couple of degrees Kelvin, or less than 1.0% [20]. The second most appealing aspect of thermocouples is their low cost. Not surprisingly, explosive detonations are very intense and can often damage equipment so having a negligible replacement cost is very attractive. The main reason that thermocouples are not the gold-standard of temperature measurement is their relatively slow response times. Thermocouple response times are a function of the physical construction of the probe such as wire diameter, weld type, and shielding thickness in some cases. Explosives will drive temperature changes over microseconds, and thermocouples sufficiently robust enough to survive explosions may have time constants on the order of a few milliseconds [21, 22]. The time constant is also only defined as the time to reach 63.2% of the instantaneous temperature change [21]. This raises questions as to the validity of the reported accuracy in scenarios where there is insufficient time for the thermocouple to equilibrate with the surrounding flow.

In addition to the physical response of the probe, which is often measured in liquid immersion, thermophoresis in gas flows and sooting will further change the response time [23]. To maintain the original response time, the tip of the probe needs to be cleaned between tests. The soot deposition on surfaces in explosive testing would lead to fouling that slows the response time even further.

Another very popular approach to thermometry of explosive events is optical pyrometry [15]. Much like thermocouples, pyrometry benefits from simplicity and low cost. A more rigorous discussion of this technique is presented in Section 2.9 of this document. Briefly, pyrometry employs low-resolution spectrometers, or filtered photodiodes to characterize the thermal radiation of an event. Based on the radiative intensity at different wavelengths, a temperature can be inferred.

Pyrometry has been demonstrated across a large range of explosive testing scales from both outside [15] and inside [17] the fireball. The extraordinary amount of light emitted in detonation and post-detonation combustion makes optical pyrometry very appealing. That being said, this highlights an exceptional limitation of these techniques in that they

only provide measurements when temperature is sufficiently high to produce quantifiable emitted radiation. In C-WMD applications, there is interest in the environment throughout all phases of the explosion. That is to say, there is need for the temperature of the event from initiation, through aerobic combustion, and even through the cooling, as that characterizes total thermal exposure during an event. In free-field scenarios, fireball breakup and cooling will significantly shorten the measureable time scales of emission techniques.

In addition to not being able to quantify temperature of the event after emission subsides, pyrometry measurements are plagued with uncertainty. Their signals predominantly reflect the condensed phase material in the event, which has an associated emissivity. The emissivity can be a function of temperature, wavelength, material, and particulate density [24, 25]. In a controlled and reproducible environment, these properties can be measured and corrected for. However in the turbulent and variable environment of explosive fireballs, significant assumptions of these properties can lead to 100's of Kelvin error in calculated temperature.

Using filtered photodiodes to characterize the color temperature of an event presents additional challenges with potential spectral interferences. While many common emission signatures are known and can be avoided with filter choice, it would somewhat hasty to use filtered photodiode pyrometry in an event with unpredictable spectral interferences. The use of a low-resolution, calibrated spectrometer provides an opportunity to overcome this because selective and continuum emission are more easily discriminated in post-processing [26, 17]. This approach does however work against the hardware simplicity of photodiodes because it requires fielding a spectrometer instead, sacrificing the exceptional temporal resolution of single pixel detectors.

One of the larger limitations of emission techniques such as pyrometry is the uncertainty in spatial characterization. Articulated simplistically, it is very difficult to identify where the measured light in a large event originated from. In standoff, the contribution path length along the instrument's line of sight will only see light up to the attenuation length scale. This will have strong wavelength and scattering media dependence but is potentially very short. This limitation would then suggest that emission techniques could

only characterize the outer surface of a fireball, potentially centimeters thick depending on the wavelengths being measured [16]. The wavelength dependence of scattering effects suggests that infrared (longer wavelengths) light could be used to characterize further into a fireball [14, 27]. This is, however, a current field of research and unverified at the current time. Regardless of penetration depth into the fireball, the measured signal from outside will be convolved along the emitting path length which will have a temperature gradient in itself that skews the measurement.

Emission spectroscopy has also been successfully conducted inside of post-detonation fireballs [28]. It is of interest to note that these results showed that at early times in the post detonation fireball, emission was confined to the surface while the interior remained dark. The absence of light during this phase would render emission techniques infeasible at these locations. At later times in the fireball expansion, this work showed that the light measured inside the fireball had minimal difference from that collected from the surface. This is an interesting finding that highlights an additional phase of the explosion where lack of emitted light will obviate the measurement.

With the uncertainty of emission techniques, it becomes pertinent to evaluate optical absorption strategies with application to explosive temperature. Absorption spectroscopy presents the advantage of probing the ground state of atomic and molecular systems as opposed to the excited state which may not be in radiative equilibrium [18, 29]. Additionally, absorption spectroscopy presents an opportunity to be fully quantitative with known path length (albeit averaged) between emitter and detector. In addition, absorption techniques are not limited to times when the measurement media itself is emitting. With a dedicated source, absorption spectroscopy can be used during dark portions of the event.

It is infeasible to present an exhaustive review of all optical absorption techniques in this literature review. Optical absorption spectroscopy has been employed for measuring temperature in combustion scenarios using a host of techniques. Impressive work by Kliewer [30] and Kearney [31] at Sandia has demonstrated highly accurate temperature measurements using coherent anti-Stokes Raman spectroscopy (CARS). CARS has many advantages which make it an incredible thermometry technique including spatial and

temporal resolution as well as its precision. The critical limitation in applying CARS to large scale explosive testing is the cost and complexity of the equipment.

Another promising optical absorption technique is tunable diode laser absorption spectroscopy (TDLAS). TDLAS employs a semiconductor diode laser and a single pixel detector. The current injected into the laser is rapidly modulated such that the emitted light is tunable across a narrow frequency range. With a swept wavelength source, only a single pixel detector is needed. No spectrometer or grating is required. Diode laser gas sensing has been used in countless lab-based [32] and in situ measurements [33]. One of many recent demonstrations was the work of Mattison [34]. He developed a near-infrared sensor to measure the temperature in pulse detonation engines [35]. Not surprisingly, pulse detonation diagnostics will be analogous to ones used in post-detonation explosive diagnostics. Mattison was using TDLAS to monitor a water vapor absorption band near 1390 nm. This band of water vapor was also used by Carney [36] and Koch [37] to measure the temperature of explosive fireballs. Both of these works employed broadband light source that was separated on a grating and projected onto a linear array. The significant equipment involved in this technique makes the fieldability rather challenging. That being said, combining the cost-effective, compact nature of Mattison's technique, with the hardened gauge approach of Carney and Koch provides a conceptual introduction of the application TDLAS in explosive fireballs for high speed temperature measurement. The temperature would be explicitly gas phase and relatively unperturbed by the minimally intrusive probe.

In addition to fielding TDLAS probes in explosive fireballs to obtain gas temperature, such techniques can equivalently provide access to measurement of iodine chemical speciation. Historically, the arc spectrum of atomic iodine was recorded by Evans [38]. Shortly after, Turner reported the absorption of atomic iodine atoms in a gas cell back-illuminated with a carbon arc [39]. These original observational studies were largely conducted for fundamental understanding of atomic and molecular dynamics. More recently, the interest in atomic iodine has been for applications in chemical oxygen iodine lasers (COILs). Briefly, conventional COILs use singlet oxygen $O_2(\,^1\Delta_g)$ to dissociate molecular iodine (I_2) into atomic iodine(I) which subsequently serves as the gain

medium. Newer systems employ multistep chemical reactions to optimize laser performance [40, 41]. A synopsis on the history of COIL technology in the United States was catalogued by Truesdell et al. [42]. The reason that COILs gained popularity in recent decades was their application to military technology. As the 1315 nm transition is the lasing transition in COILs, there is a substantial body of literature on the chemical generation of atomic iodine and the relevant spectroscopic properties [43, 44, 45, 46].

More specifically to the measurement of atomic iodine with spectroscopic methods, there have been several published studies using diode lasers to monitor the 1315 nm transition. The COIL community has benefitted from the development of diode lasers because it has enabled them to have low-cost, low-power techniques for monitoring intercavity atomic iodine concentrations. Manke et al. used a diode laser based monitoring of the (F',F") = (3,4) hyperfine component of the 1315 nm transition to demonstrate the all gas iodine laser (AGIL) [47]. Impressively, Davis developed a suite of distributed feedback (DFB) tunable diode laser sensors for simultaneous monitoring of atomic iodine, singlet oxygen, and water vapor concentration in COIL cavities [48, 49]. As previously demonstrated and discussed here, TDLAS has become a prolific combustion diagnostic. The COIL community has demonstrated using TDLAS to monitor atomic iodine. With respect to monitoring iodine in a combustion scenario, it is logical to harmonize the two technologies and use diode lasers to probe the post-detonation fireball.

In summary, the defense community is looking to model the temperature and speciation of post-detonation fireballs to predict C-WMD performance. The present work conducted at the University of Illinois at Urbana-Champaign was to develop, demonstrate, and disseminate diagnostics that can provide experimental validation for computational modeling of these types of events. The target deliverables were tools and techniques for in situ measurement of post-detonation gas temperature and atomic iodine concentration.

CHAPTER 2: TEMPERATURE MEASUREMENT IN EXPLOSIVE FIREBALLS

2.1. Introduction to Temperature Measurement:

This chapter will detail the development of minimally intrusive optical diagnostics for high-speed temperature measurement inside explosive fireballs. Temperature is one of the most critical thermodynamic properties for explosive diagnostics. Its dictation of chemical speciation and equation of state alone have made its measurement the focus of experimentalists for a long time. Unlike pressure, which has a relatively simple method of collection with piezoelectric transducers, unperturbed temperature of an explosion cannot be readily obtained.

Equations 2.1-2.4 illustrate the central importance of temperature in all thermodynamic modeling [29]. The partition function (Z) is solely a function of constant material energy levels (E_i) and temperature (T). From this we get expected energy ($\langle E \rangle$), specific heat (C_v), and entropy (S) through which we can derive equations of state. From these equations, it is clear that explosive performance and thermal chemistry is intimately aligned with material temperature.

$$Z = \sum_i \exp\left(\frac{-E_i}{k_B T}\right) \tag{2.1}$$

$$\langle E \rangle = k_B T^2 \frac{\partial}{\partial T} ln(Z) \tag{2.2}$$

$$C_v = \frac{\partial}{\partial T} \langle E \rangle \tag{2.3}$$

$$S = \frac{\partial}{\partial T} k_b T ln(Z) \tag{2.4}$$

To measure the internal gas temperature and speciation of explosive fireballs, a probe was developed to house a tunable diode laser (TDL), infrared detector, and pressure transducer. The probe then survives being engulfed in the explosive shock and detonation products, enabling any number of proven TDL combustion techniques to be fielded [34,

35, 50, 33, 51]. The probe is shown mounted in the explosive blast chamber in Figure 3 and is illustrated in Figure 4.

Figure 3: The probe (bottom right corner) mounted in the 1.81 cubic meter explosive blast chamber at the University of Illinois at Urbana-Champaign Explosive Diagnostics Lab.

As previously mentioned, temperature measurement in explosive fireballs using the 1300nm water band has been previously demonstrated at Naval Surface Warfare Center Indian Head (NSWCIH) and Marquette University [36, 37, 52]. As was done in the present work, researchers designed and constructed a hardened gauge capable of witnessing high explosive events. In contrast to the current design's swept wavelength source, their process employed pitching a broadband light source across a slab of explosive product gas and collecting it on a catch fiber to be brought out of the chamber and separated in a spectrometer. This technique was utilized to evaluate a variety of high explosives including non-ideal formulations that are fuel-rich and are therefore expected to produce optically-thick product clouds.

The new technique presented in this document strives to build upon the previous work in the field to enhance both temporal scale and resolution while minimizing cost. These new

developments also extend the ability of the technique to be more readily deployable in the field. To do this, the use of a spectrometer, pixel array, and broadband light source were eliminated in favor of a single pixel detector and a tunable diode laser. The limited amount of data broadcast by the photodiode allows a longer time scale to be collected, and its small size and low cost also allows it to be placed in the hardened gauge in order to extract an electrical signal as opposed to the use of an output fiber, minimizing signal losses. This change also eliminates the need to deploy and calibrate a spectrometer on-location in the case of field testing. These variations, along with a robust processing algorithm, are used to provide a simplified technique and methodology for rapidly deploying a wide variety of lab-proven tunable diode laser absorption techniques to large scale explosive testing.

2.2. Tunable Diode Laser Measurement Technique and Methodology:

A few of the technical challenges overcome in this diagnostic development include blast wave survivability, non-resonant background arising from turbulent flow, broadband thermal emission of explosive products, and substantial pressure broadening of spectral features. In the context of a chambered or partially vented explosive test, not only the initial blast wave, but constructive reflected shocks will cause multiple atmospheres of accumulated pressure. All these obstacles were overcome by both mechanical design of the probe and novel data analytics. A schematic representation of the diagnostic's functionality is shown in Figure 4.

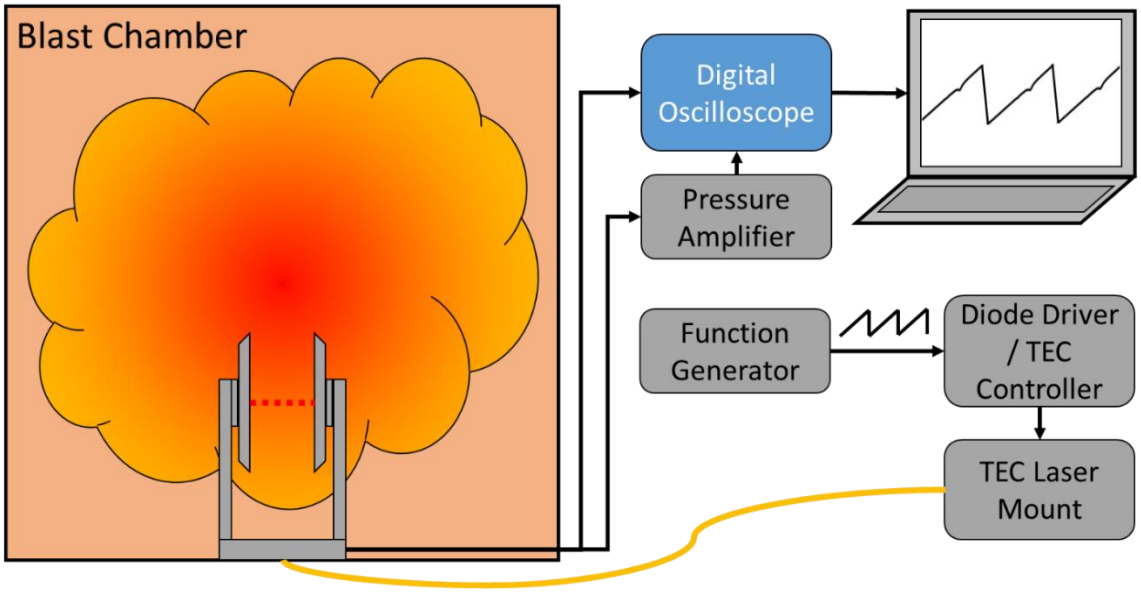

Figure 4: A schematic representation of the probe designed to house the diagnostics package and survive being completely engulfed in explosive gases. The laser is brought into the chamber through a replaceable fiber optic patch cable. The two signal-out cables are the BNC from the photodiode and the pressure transducer's USB.

As previously demonstrated by Mattison et al., this diagnostic employs a 1390 nm tunable diode laser to scan over the water vapor absorption features located at 1389.76 and 1390.05 nm [5, 9]. The laser used was an Eblana Photonics® EP1392-5-DM-B01-FA, being driven by an Arroyo Instruments 6301 ComboSource. Injection current to the diode driver was supplied by a BK Precision 4055 arbitrary waveform generator. The detector used to measure the transmitted laser signal was a ThorLabs DET20C. Dynamic pressures were measured with an Endevco® 8530B transducer, amplified with a 4428A signal conditioner. Pressure transducer and photodiode output voltages were recorded with a PicoTechnology 4424 digital oscilloscope at a rate of 10 MHz. Other off-the-shelf supplies included a FC/APC to FC/PC patch cable from ThorLabs (P#: P5-SMF28E-FC-2), a beam collimator from ThorLabs (P#: F220FC-C), a 1" wedged calcium fluoride window also from ThorLabs (P#: WW51050), a low optical depth thin film filter from Roscolux (100 Frost), a bandpass filter, and a short focal length lens. The remaining parts of the apparatus were fabricated in-house, such as aluminum parts for the probe body, a Delrin® mount for the beam collimator and pressure transducer, and a holder to maintain the angle of the bandpass filter. The configuration of the internal components of the probe is depicted in Figure 5.

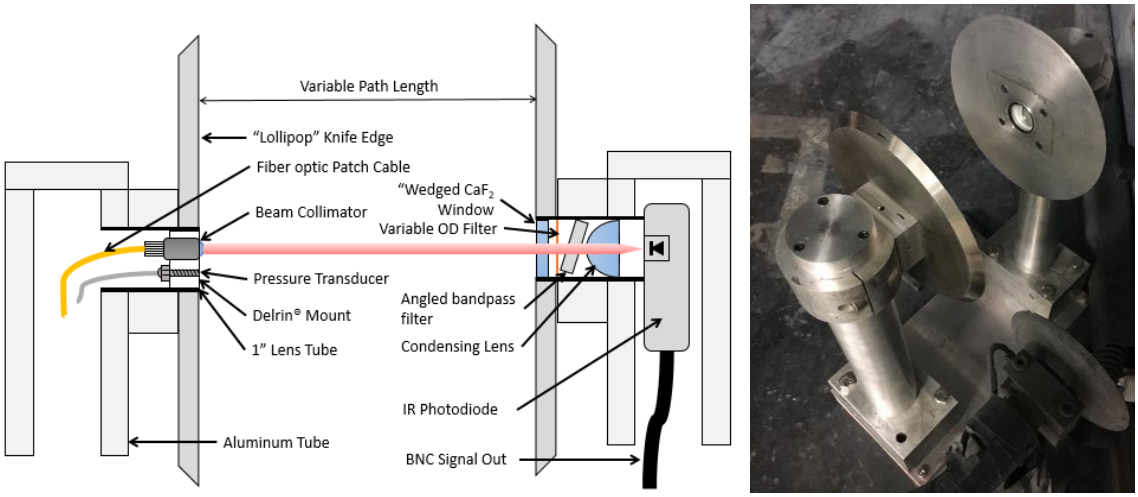

Figure 5: Schematic of the internal layout of optical and barometric components used in this diagnostic. (left) A picture of the probe mounted in the 1.81 cubic meter explosive blast chamber. (right)

As in all absorption spectroscopy techniques, this measurement is path-averaged and thus cannot resolve gradients between emitter and detector. The probe was designed explicitly to have a field-selectable path length. With all the optoelectronics contained in the vertical tubes, having multiple base plates of different lengths with mounting bolt patterns enables custom selection of a path length that can achieve the optimal balance of species absorption depth to total signal attenuation. This is a critical design feature given the dynamic change of water vapor content between ambient, shocked, and combustion air for a given test.

In climates with very little ambient water vapor, it becomes necessary to use a longer path length to quantify shocked air, as that change does not contribute any absorbing species to the signal. The drawback to this is with the increase path length, the beam steering on density gradients can degrade the signal beyond usability and the spatial resolution is reduced. An alternative approach in chambered experiments is to increase chamber vapor content prior to detonation by letting liquid water evaporate or by burning a hydrocarbon in the sealed vessel. In some of the data presented here, a 28 cm path length was used, and chamber surfaces were slightly wetted prior to testing. Other tests were conducted with 13 cm path lengths without any need for added water vapor due to greater ambient humidity. Shorter path lengths provide better signal quality with higher spatial resolution.

Many of the charges tested in this work were assembled from 28-gram PBXN-5 pellets, both whole and fractured to create appropriately sized charges. These charges were initiated with a Teledyne RP-81 detonator. A Teledyne RISI FS-61B fireset was used in conjunction with a Quantum Composers 9520 Series pulse generator for triggering the oscilloscope and charge simultaneously.

For development testing of the probe, the chamber utilized was a 48" cube constructed of ½" thick steel with one side removable for access held on by 24, ¾" bolts. This chamber is well established by the Energetic Materials Diagnostic Lab at the University of Illinois Urbana-Champaign to be able to handle charges of this size. It is equipped with two wall-mounted piezoresistive static pressure sensors, two lollipop-mounted, movable piezoresistive static pressure sensors, and two piezoelectric pencil-style mounted dynamic pressure sensors. These sensors, while not used directly in the analysis, were utilized for verification of pressure data collected by the probe.

2.3. Data Processing, Collection, and Analytics:

Given the overlap of spectral lines in this feature, it is difficult to numerically integrate peaks to obtain absorbance. This problem is only exacerbated with the observed pressure broadening. In line with the work of Carney and Lightstone, it was determined that the most accurate way to extract temperature and concentration was to fit the measured spectra to a physically accurate model [36]. Briefly, transition parameters were taken from the HITRAN 2016 database, and all temperature-dependent properties were scaled appropriately. The partition function (including nuclear contributions) was reconstructed from polynomials; the Voigt function was taken as the real part of the Fadeeva function, and the temperature scaling exponent for pressure shift coefficients was taken to be 0.96 [53, 54, 55]. While much of the accuracy of this model exceeds the resolution of the experimental data, it was rigorously validated with comparison to published models spanning the appropriate temperature and pressure domain [54]. Sample model comparisons are shown in Figure 6Figure 12. The frequency-dependent deviations are differences in line shape model, while the frequency-independent difference such as the -1% residual at all wavenumbers in the 296 K simulation represents a difference in partition function value at that temperature.

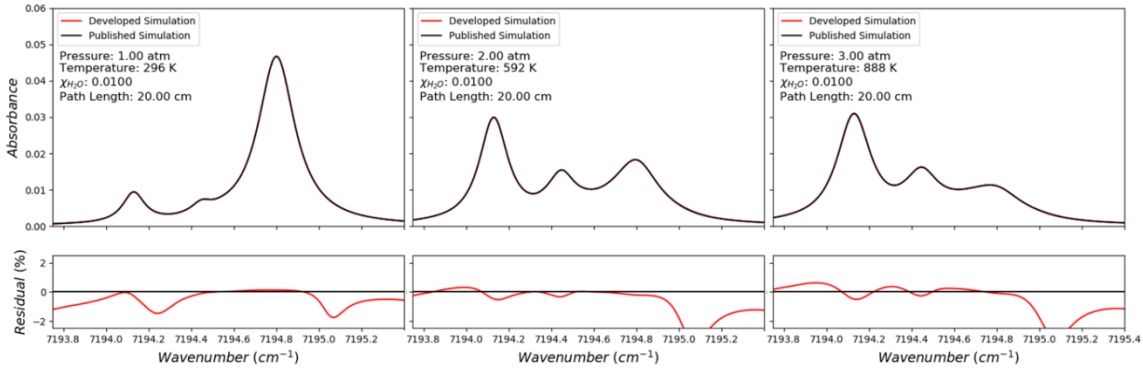

Figure 6: Comparison of developed spectral model to that of Goldenstein et al. that was published in the Journal of Quantitative Spectroscopy and Radiative Transfer [54]. Comparison was used to validate accuracy of the quantitative model developed and used to fit raw data to temperature and mole fraction.

Raw voltages recorded on the digital oscilloscope were separated into individual scans, and a background was reconstructed using a spline fit between two linear regressions of data outside the water vapor absorption band. One regression is drawn backwards from data points above the spectrum, and one drawn forwards from points below it. The sensitivity to background fit is dominant at lower temperatures, where the lower wavenumber transition is substantially weaker. At higher temperatures when both features are well defined, the accuracy of fitted temperature and concentration is obviously enhanced.

A two-parameter (T, X_{H2O}) minimization routine was programmed to fit an in-house model to the measured transmittance spectra [56, 57]. The simulation uses the pressure measured by the probe's transducer located adjacent to the laser beam and iteratively fits each laser scan in time. The minimization algorithm mathematically combines the integrated absorbance with a variable order spectral weighting function to assist with solution uniqueness. The weighting function places an exponential penalty on the integrated absorbance, if the peak transmittance differences at line-center are not simultaneously minimized. The initial guess for this minimization is taken from the measured pressure relative to atmospheric conditions, assuming a constant total number density. Figure 7 shows good samples of the solution that the algorithm converges to with real data from a 40 gram PBXN-5 explosive test. It can be seen in the low temperature

case that even with less than 2% absorption depth and approximate 10:1 signal to noise ratio, this technique is capable of achieving reasonable measured values.

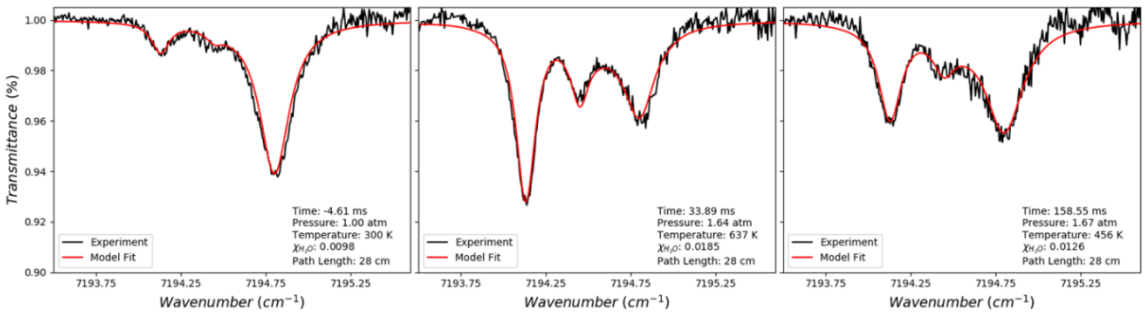

Figure 7: Three samples of algorithm fit to actual experimental data from different points in the event. Pre-trigger is shown on the left, late blast phase is shown in the center, and quasi-static conditions at late time on the right.

In order to elaborate slightly on the fitting algorithm that was implemented, a characteristic model is shown in Figure 8. This illustration shows simulated data in black, a simulated "guess" at the solution in red, and the defined residual being a weighted combination of purple and blue shading between the two spectra. Typical residuals for model fitting use the integrated value of the absolute difference. The program developed in this work functions similarly, but with the addition of a spectral weighting argument. This particular spectrum is temperature sensitive predominantly between the two main transitions. This implies that the accuracy of the temperature calculation is governed predominantly by the residual near the two line centers.

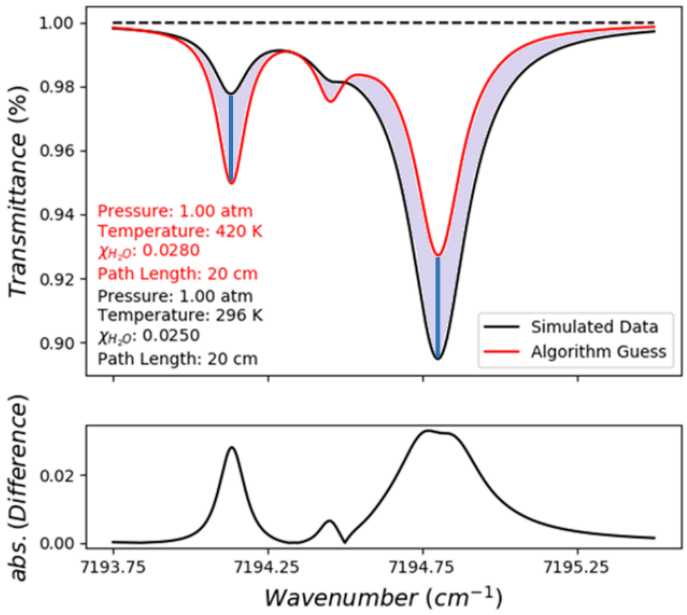

Figure 8: Qualitative illustration of the residual that was developed and used in the fitting algorithm. The figure shows a simulated transmittance spectrum (black) and a simulated solution "guess" (red). The residual is shown in purple and blue shading.

The residual was defined as the integral across the entire spectral feature, multiplied by the residual at line center of the two transitions integrated across a differential. This is shown as purple shading, and blue shading respectively in Figure 8. The line center integral was raised to a variable, but arbitrarily large power to place exponential importance on satisfying that criteria. One benefit to this approach is to say for example, if a piece of debris causes near resonant absorbance, or total attenuation, then the spectrum remains usable because the algorithm is predominantly looking to minimize only the line center residual. This results in fewer scans being rendered unusable due to partial beam chopping and near resonant distortion. There is an additional benefit with respect to accuracy of temperature that is difficult to quantify, but can still be described. As the backgrounds are drawn from spline interpolations of linear regressions from outside the absorption band on each ramp, the temperature sensitive features on the edge are nearer to the regressed data and therefore characterized more accurately with respect to the "true" background. Conversely, an end-to-end band integral of the structure may get fit to a false truth trying to match the middle of the structure which has higher

uncertainty in the accuracy of background. Compared to a single point at line center, utilizing a differential of spectrum around the line center helps retain the robustness against the noise generated by-the-bit resolution in the oscilloscope used.

Since the data processing was a minimization, an additional analysis of the solution uniqueness was conducted. This was done by constructing a matrix of temperature and concentration (T, X) pairs and simulating the water vapor features at each of these. These were then compared to a defined "target" spectrum representing the true temperature and concentration for the minimization. The residual, as described above, was recorded and plotted on a heat map to illustrated two-dimensional parameter space. Two examples of this are shown in Figure 9.

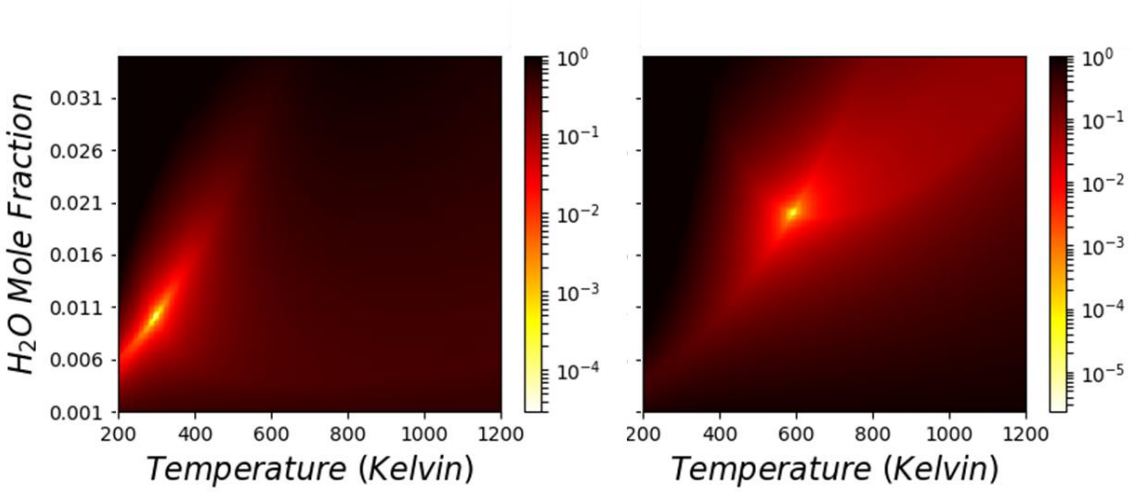

Figure 9: Examples of solution uniqueness investigation. Algorithm residuals compared to a target spectrum simulated at 296 Kelvin, 0.01 mole fraction, 1 atm., with a 20 cm path length is shown on the left. Residuals compared to a target spectrum simulated at 592 Kelvin, 0.02 mole fraction, 1 atm., with a 20 cm path length is shown on the right.

In addition to the examples shown here, many other conditions were checked using this method, and the effects of the initial guess for the routine were also investigated. Any reasonable initial guess had no effect on the final solution, but did change the number of iterations required to find it.

2.4. The Partition Function of Water Vapor:

Temperature is fairly robust against error as it is independent of both path length and partition function. Number density (concentration) is, however, linearly dependent on the

partition sum and therefore subject to any errors in its computation. This section focuses on the potential sources of error owing to the choice of partition function in the spectral model.

The total internal partition sum (TIPS) for water vapor was constructed from the following four methods with their comparative results presented at the end of this section:

i. *Published Polynomial Coefficients*

ii. *Analytical Equations*

iii. *Direct Numerical Summation of Energy Levels up to 1st Dissociation Limit*

iv. *Tabulated Values from Direct Summation of BT2 Line List*

The Published Polynomial Coefficients were formally published by Zhou et al [33]. Those values are reproduced in Table 1 and are used with Equation 2.5. The programmatic advantage of using a polynomial reconstruction is mainly for computational simplicity. As there are also regimes for each polynomial set, it becomes important to be aware of discontinuous curves at the intersection points.

Coefficients	70 < T < 405 K	400 < T <1500 K	1500 < T < 3005 K
a	-4.4405E+00	-9.4327E+01	-1.1727E+03
b	2.7678E-01	8.1903E-01	2.9261E+00
c	1.2536E-03	7.4005E-05	-1.3299E-03
d	-4.8938E-07	4.2437E-07	7.4356E-07

Table 1: Tabulated polynomial coefficients for water vapor partition function.

$$Z_{tot}(T) = a + bT + cT^2 + dT^3 \tag{2.5}$$

Moving on to the more rigorous analytical model, water vapor is a nonlinear, triatomic, molecule with hydrogen nuclei having half-integer spin, thereby making it a Fermi system upon rotation, so it is necessary to account for rotational, vibrational, and nuclear partition functions. Any electronic excitation of water vapor requires energies over 53,800 cm^{-1} and therefore is neglected here [58]. The total partition function is expressed in Equation 2.6.

$$Z_{tot}(T) = Z_{rot}(T)Z_{vib}(T)Z_{nuc} \tag{2.6}$$

Consider next the constituent partition functions for each mode. The rotational partition function $Z_{rot}(T)$ can be calculated from tabulated rotational constants for each principle axis (often denoted A, B, and C), or even more fundamentally from the corresponding moments of inertia (I_A, I_B, I_C) for which numerous sources exist. It is convenient to convert the rotational constants to characteristic temperature, which is a simple conversion of energy from cm^{-1} to Kelvin. In the following equations $A, B, or\ C$ are the rotational constants in wavenumbers (cm^{-1}) corresponding to one of the three principle axis, h is Planck's constant, c is the speed of light, k_B is Boltzmann's constant, $I_{A,B,C}$ is the moment of inertia about the respective axis, T is temperature in Kelvin, and Θ is the corresponding characteristic rotational temperature. σ is the symmetry factor for which water vapor has a value of 2.

$$A, B, C = \frac{h}{\pi^2 c I_{A,B,C}} \tag{2.7}$$

$$\Theta_{A,B,C} = \frac{hc}{k_B} A, B, C * 100 \tag{2.8}$$

$$Z_{rot}(T) = \frac{\pi^{1/2} T^{3/2}}{\sigma \Theta_A^{1/2} \Theta_B^{1/2} \Theta_C^{1/2}} \tag{2.9}$$

A few examples of the water vapor molecular properties available in the literature are provided below in Table 2. The NIST Computational Chemistry Comparison and Benchmark Database provides a sizable number of theoretical predictions for these parameters calculated from a number of different quantum mechanical methods [59]. Similarly, they also provide experimentally measured data for these parameters [60]. It was seen that the subtle differences in which these constants were obtained had a slight effect on the absolute value, which then propagates through any computation of the partition function. It is worth noting that the moment of inertia of any molecule is in itself a function of temperature, and therefore using a constant value is inadequate at elevated temperatures.

Axis (-)	Moment of Inertia (kg / m^2)	Theoretical Constant (cm^{-1})	Experimental Constant (cm^{-1})
A	1.0528E-47	26.5893	27.8770
B	1.9080E-47	14.6716	14.5120
C	2.9607E-47	9.4546	9.2850

Table 2: Samples of tabulated parameters that can be used in the computation of the rotational partition function of water vapor.

The analytical model of the vibrational partition function, $Z_{vib}(T)$, is simply the product expressed in Equation 2.6 for all vibrational modes in the molecule. The zero of energy is taken from the ground vibrational state. In Equation 2.10, Θ_v is the characteristic vibrational temperature in Kelvin calculated from the vibrational frequencies typically provided in wavenumbers.

$$Z_{vib}(T) = \prod_v \frac{1}{1 - \exp\left(-\frac{\Theta_v}{T}\right)} \tag{2.10}$$

Vibrational frequencies can also be found in a number of different sources with very slight discrepancies in value or precision. Samples of tabulated vibrational frequencies from reliable sources are provided in Table 3.

	HITRAN / NIST [53, 59] (cm^{-1})	Atkins [61] (cm^{-1})
Symmetric Stretch (v_1)	3657	3656.7
Bend (v_2)	1595	1594.8
Asymmetric Stretch (v_3)	3756	3755.8

Table 3: Sample vibrational frequencies for the vibrational modes of water vapor.

The final partition function to account for in the analytical model was the nuclear contribution. The nuclear partition function Z_{nuc}, is defined by Equation 2.11 as the product of *2I+1* for all nuclei (*N*) in the molecule, where *I* is the spin quantum number of a given nucleus [54]. In the case of water vapor, both Hydrogen nuclei have ½ spin, and

the central Oxygen has 0 spin. This gives water a temperature-independent nuclear partition function of $Z_{nuc} = 4$.

$$Z_{nuc} = \prod_{N} (2I + 1) \tag{2.11}$$

Although this analytical model is an acceptable method for a wide range of polyatomics in some temperature regimes. Additional sources of error potentially stem from the lack of higher order correction terms ($\omega_e x_e$, $\omega_e y_e$, $\omega_e z_e$, α_e, D_e, etc.) for the rotational-vibration energy coupling in the anharmonic oscillator expansion.

Somewhat as an exercise in statistical mechanics, another model of the partition function was constructed using a direct summation. That is, a numerical summation using Equation 2.1 and one of multiple available energy level lists for water vapor was employed. For this model, the Measured Active Rotational–Vibrational Energy Levels (MARVEL) generated line list was numerically summed over [58]. This line list is very extensive, but still comparatively incomplete to that of the BT2 list which is taken to be the most comprehensive list available. The MARVEL list contains 18,486 energy levels up to the first dissociation limit of water.

As previously mentioned, the exchange of Hydrogen nuclei upon rotation makes water vapor a Fermi system owing to the ½ integer spin of those nuclei. The MARVEL line list is provided with energy levels and the associated rotational quantum number J. In order to appropriately calculate the state degeneracy of each level, Equations 2.12 and 2.13 are used to calculate the state-dependent degeneracy factors [62, 63, 64]. This gives rise to a degeneracy multiplier of three for odd J energy levels ($g_{i,odd} = 3(2J_i + 1)$), and one for even J levels($g_{i,even} = 1(2J_i + 1)$). This correction should be noted when working with HITRAN degeneracies, as those transitions are tabulated with appropriately-corrected nuclear statistics for the upper and lower g values of each transition.

$$\text{Fermi System-Even State:} \quad \frac{1}{2}[(2I_x + 1)^2 - (2I_x + 1)] \tag{2.12}$$

$$\text{Fermi System-Odd State:} \quad \frac{1}{2}[(2I_x + 1)^2 + (2I_x + 1)] \tag{2.13}$$

The final source of the water vapor partition function evaluated in this analysis is the tabulated form generated from the BT2 line list made available through ExoMol [65]. This source represents the most comprehensive data on water vapor transitions (505,806,202) and energy levels (221,097) available. They provide a simple two-column text file with the temperature and total internal partition sum values up to 5,000 Kelvin. Presumably this is computed from a direct, numerical summation over their calculated energy level list. This partition function is simply incorporated into the spectral model in a computationally efficient way using a spline interpolation of the tabulated arrays.

The linear dependence of lower state population fraction on partition function is a direct source of error that is introduced into the final calculation of species concentration. Given the various approximations and sources of the partition function it is critical to know what temperature regimes a given model may be acceptable in. Figure 10 shows all of the computed partition functions as well as their respective deviations from the BT2 computation as that is accepted as the most accurate. A numerical differentiation program was written to calculate the specific heat using Equation 2.3. The reason for doing this was to compare to the NASA polynomial expansions for specific heat, as these are widely accepted across many thermodynamic specialties [11]. This comparison is shown in Figure 11.

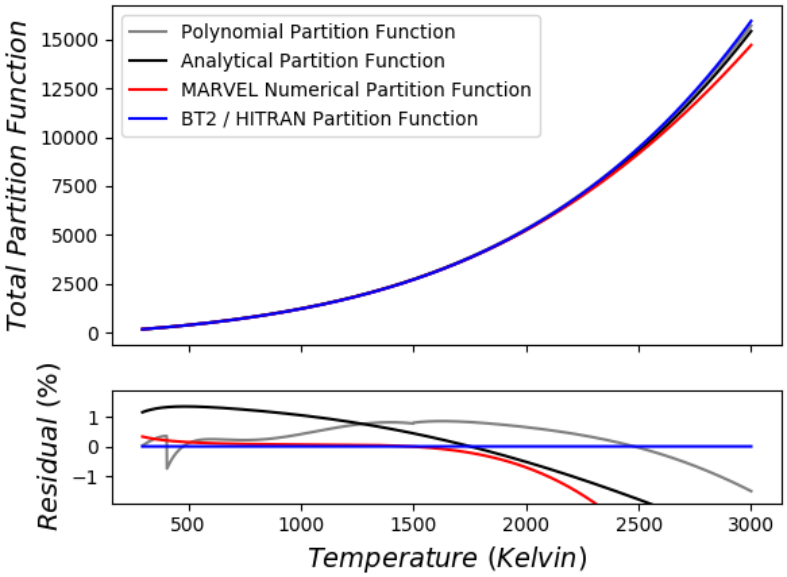

Figure 10: Comparison of polynomial fit, analytical, numerical, and tabulated partition function data for water vapor. (top) Residuals are shown as percent deviation from the BT2 partition function (bottom).

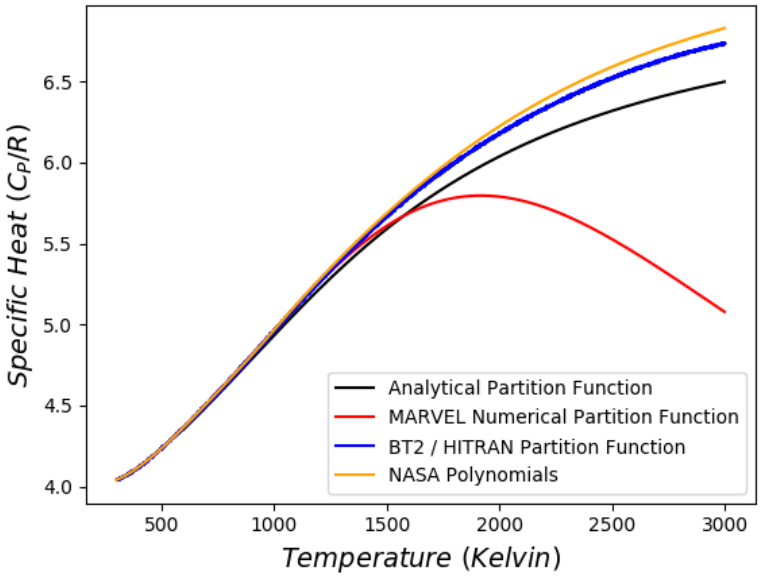

Figure 11: Numerically calculated specific heats of water vapor from the analytical, numerical and BT2 tabulated partition function comparted to the NASA 7 term polynomial coefficient data.

In the present work, where the majority of measured fireball temperatures were measured below 1000 Kelvin, models show that there is nominally less than 1% error introduced by any of the methods discussed. However, there is no doubt that this diagnostic will be

applied to higher temperature systems such as aluminized fireballs and that will necessitate use of the BT2 partition function above 2000 Kelvin.

Pertaining to the calculated specific heat, it is interesting to note that a partition function can be accurate to within a couple percent, while the derived thermodynamic property C_p/R can deviate by substantially more. The observed deviation of the MARVEL calculated partition function is attributed to that list of energy levels only being calculated up to the fist dissociation limit.

2.5. Hardened Gauge Blast Chamber Results:

Testing has demonstrated successful measurement in tests up to 40 grams of PBXN-5, and survival up to 60 grams at standoff distances of 52 cm. Non-dimensional blast scaling suggests a 41.76 gram test at 52 cm standoff scales to 3.6 m from 10 kg of the same type of explosive [66].

Figure 12 shows data for a 28.48 gram explosive test in which temperature was measured across the initial shock wave. The piezoresistive pressure transducer built into the probe has a response time of approximately 2 microseconds and thus does not resolve the peak pressure in a blast wave as well as a piezoelectric sensor does. The 5 microsecond averaged pressure during the blast wave was computationally fit with a modified Friedlander equation given by equation 2.14 [67].

$$P(t) = P_0 + P_{blast}\left(1 - \frac{t}{T^+}\right)\exp\left(-\frac{bt}{T^+}\right) \tag{2.14}$$

An estimate for the shock heated air behind the incident wave was calculated through normal shock relations given in equations 2.15 and 2.16 using the peak of the averaged pressure [68]. Measured temperatures show good agreement with these calculations, despite the limitations of the pressure sensor in resolving peak pressures.

$$M = \sqrt{\left(\frac{\gamma+1}{2\gamma}\right)\left[\left(\frac{P_{blast}}{P_{ambient}}\right) + \left(\frac{\gamma-1}{\gamma+1}\right)\right]} \tag{2.15}$$

$$T_{shocked} = T_{ambient} * \frac{\left(1 + \frac{\gamma-1}{2}M^2\right)\left(\frac{2\gamma}{\gamma-1}M^2 - 1\right)}{M^2\left(\frac{2\gamma}{\gamma-1} + \frac{\gamma-1}{2}\right)} \tag{2.16}$$

As can be seen by the absence of data points around 1 ms in Figure 12, there are portions of the explosion that result in beam chopping or steering that either renders individual scans unusable or produces unreasonable values. But this result demonstrates the diagnostic's capability to accurately characterize temperature fluctuations on the order of tens of microseconds.

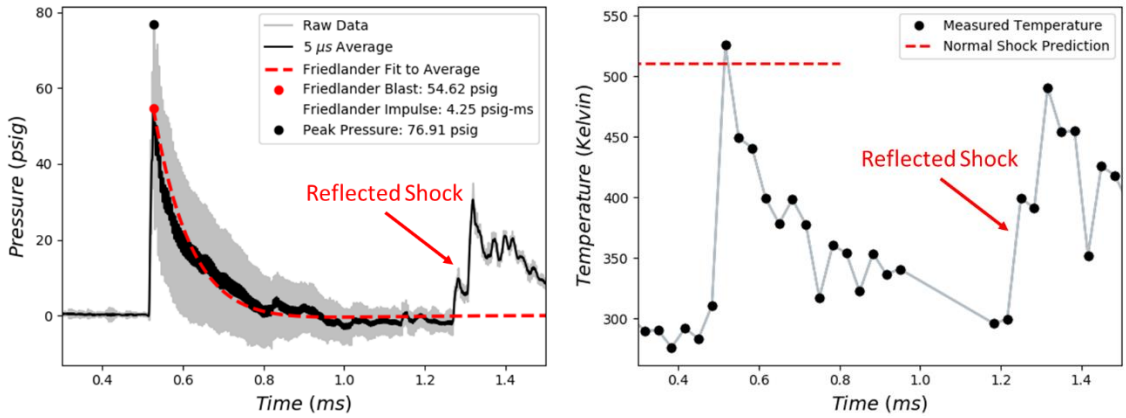

Figure 12: Primary blast pressure (left) and temperature (right) from a 28.48 gram PBXN-5 high explosive test. Probe was mounted at a 21 inch standoff and scanning at 30 kHz. The normal shock predicted temperature was calculated using the peak pressure of 54.62 psig from the Friedlander fit to average.

Preliminary testing not only demonstrated the probe's capability to survive an explosive shock wave, but to also make meaningful measurements across it. Non-dimensional blast scaling arguments were made to predict performance in large scale testing. From equation 2.17 it can be seen that the explosive yield (Y) is only a function of explosive density (ρ, PBXN-5: 1.90 g/cc TMD, 0.86 g/cc bulk density) energy of detonation (E_{Det}), and charge radius (R_c) [66].

$$Y = \frac{4\pi}{3}\rho E_{Det} R_c^3 \tag{2.17}$$

When scaling explosives of the same type, the energy of detonation and explosive density are constant and therefore a blast wave parameter (P) and the radii at which the same property value will occur ($R_n(P)$) are related through equation 2.18.

$$R_2(P_1) = \frac{R_1(P_1)R_{C2}}{R_{C1}} \tag{2.18}$$

Repeated testing of the probe at a standoff distance of 0.5334 meters from nominal charge masses of 28, 40, and 60 grams of PBXN-5 were conducted in a 1.81 cubic meter blast chamber. Data quality decreases with charge size, and therefore data presented in this document does not include 60 gram tests. However the probe did successfully survive the intensity of those tests. Assuming a spherical charge, the results of blast scaling are shown in Figure 13.

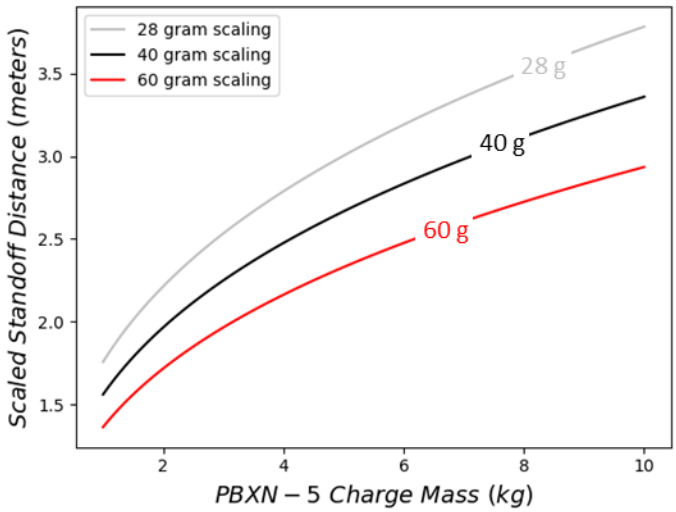

Figure 13: Non-dimensional blast scaling of successful high explosive tests conducted at the small scale in a 1.8 cubic meter blast chamber. Curves correspond to equivalent blast wave properties from gram scale explosive testing at a standoff of 0.5334 meters.

Measuring the blast wave temperature is valuable, but it is the interior of the fireball where this diagnostic is focused. The fireball represents a portion of the explosive event where turbulent mixing and aerobic combustion processes can create a number of different conditions that are very difficult to model. Following the incident blast wave, the probe is engulfed in the explosive product cloud. Data from two different sized explosive tests are presented in Figure 15.

While on the subject of explosive scaling arguments, it is pertinent to discuss the definition of *in-fireball*. Looking to scaling arguments of fireball size and duration as a function of charge mass, it is evident that a minimum standoff for the probe at this charge scale is around 0.5 meters. In his doctoral dissertation, Stephen Gilbert provides a very well-organized synopsis of explosive effects including specifically chemical explosive

fireball scaling [69]. He presents a synopsis of published empirical relations, as well as one derived from fundamental physics that agrees to a high degree with the experimental results. The compendium is broken down into fireballs generated from explosions of hydrocarbons, solid propellants, liquid propellants, and high explosives. He further organizes the document by fireball diameter, duration, temperature, and surface emissive power. In some cases, specific relations are provided for initiation configuration.

Analogous to most blast scaling, fireball properties scale approximately with mass$^{1/3}$. Gilbert includes reference to Gayle and Bransford [70] and Van Dolah and Burgess [71, 72] who report fireball diameter relations of $D = 3.30M^{0.341}$ and $D = 3.77M^{1/3}$, respectively, where D is the fireball diameter in meters and M is the charge mass in kilograms. Gilbert moves on to deriving a theoretical model for fireball evolution based on conservation laws and arrives at a relation, $D = 3.50M^{1/3}$. The results of mapping these relations are overlaid with the nominal charge sizes of the present work in Figure 14.

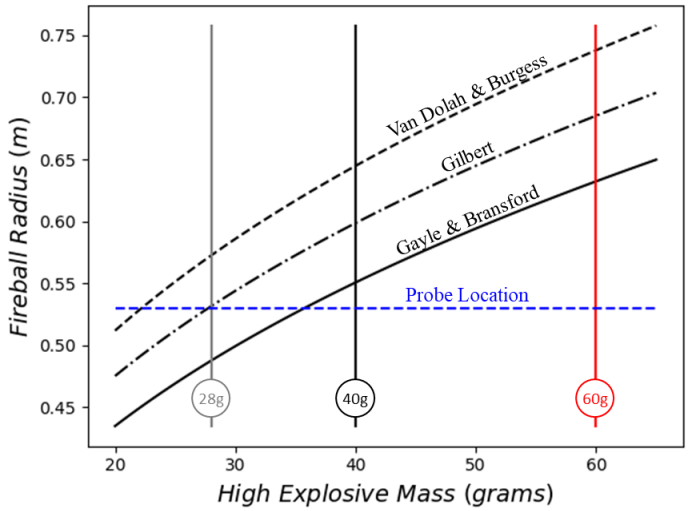

Figure 14: Simulation of explosive fireball radius relative to charge size and standoff distance of the probe at nominally 0.53m (21 in.).

As always, the scaling arguments should be taken as an approximation. The explosive fireball is subject to a huge number of influencing factors. The oxygen balance of the explosive molecule and the degree of polymerization are likely to have a significant effect on fireball properties. Another extreme caveat in this analysis is the presence of

chamber wall interactions. The shockwave driven into the ambient chamber gas in front of the product contact surface will reflect off of the chamber wall and return to the expanding gases, mixing and potentially stagnating them. Compared to free-field fireballs, chambered ones will also experience very different cooling phenomenon that play a role in the size and duration thereof. As a final note, following the scaling arguments of Strehlow and Baker for TNT fireball duration suggests charges (of TNT) at this scale produce fireballs that persist on the order of 80 to 120 ms [69, 72, 73]. This is longer than emission signals from testing suggest.

The temperature profile in the 28.48 gram test shows the superposition of slowly-diffusing explosive products and the reflected shock heating of turbulent air. The temperature history shows a combination of high frequency fluctuations (5 ms period), superimposed on much slower ones (25 ms period). These are thought to be the combination of turbulent mixing due to reflected shock interaction and mass diffusion of explosive product. No steady state in temperature was observed in the 200 milliseconds of data recorded. This observation is in stark contradiction to the pressure which reaches its global equilibrium by 60 milliseconds. Questions remain as to whether a stable temperature can be reached before wall heat transfer losses become significant.

For the case of the 41.76 gram explosive, the temperature profile appears to be making much slower oscillations around the equilibrium prediction and still differs greatly even past 200 milliseconds. Again, the temperature profile shows strong temporal agreement to water vapor concentration but not pressure. The measured pressure in this test was slightly lower than what is expected at equilibrium. This result is likely attributed to variations in completeness of afterburn oxidation, which is strongly influenced by chamber mixing and will be scale-dependent.

Both of these tests highlight the difference in relaxation time between temperature and pressure. The interplay between these two properties is exceptionally complex. In chambered explosive tests, shock waves will produce gas dynamic heating of ambient air that cools rapidly behind the expanding wave. After that, chamber interaction will produce complex three-dimensional reflections that dramatically change the aerobic combustion of the post-detonation fireball through turbulent mixing. This observation

highlights a critical fact that the temperature measured by the probe is going to be a strong function of its location relative to the chamber and charge. It certainly demonstrates the assumption of a homogenous chamber even at this scale would be inappropriate.

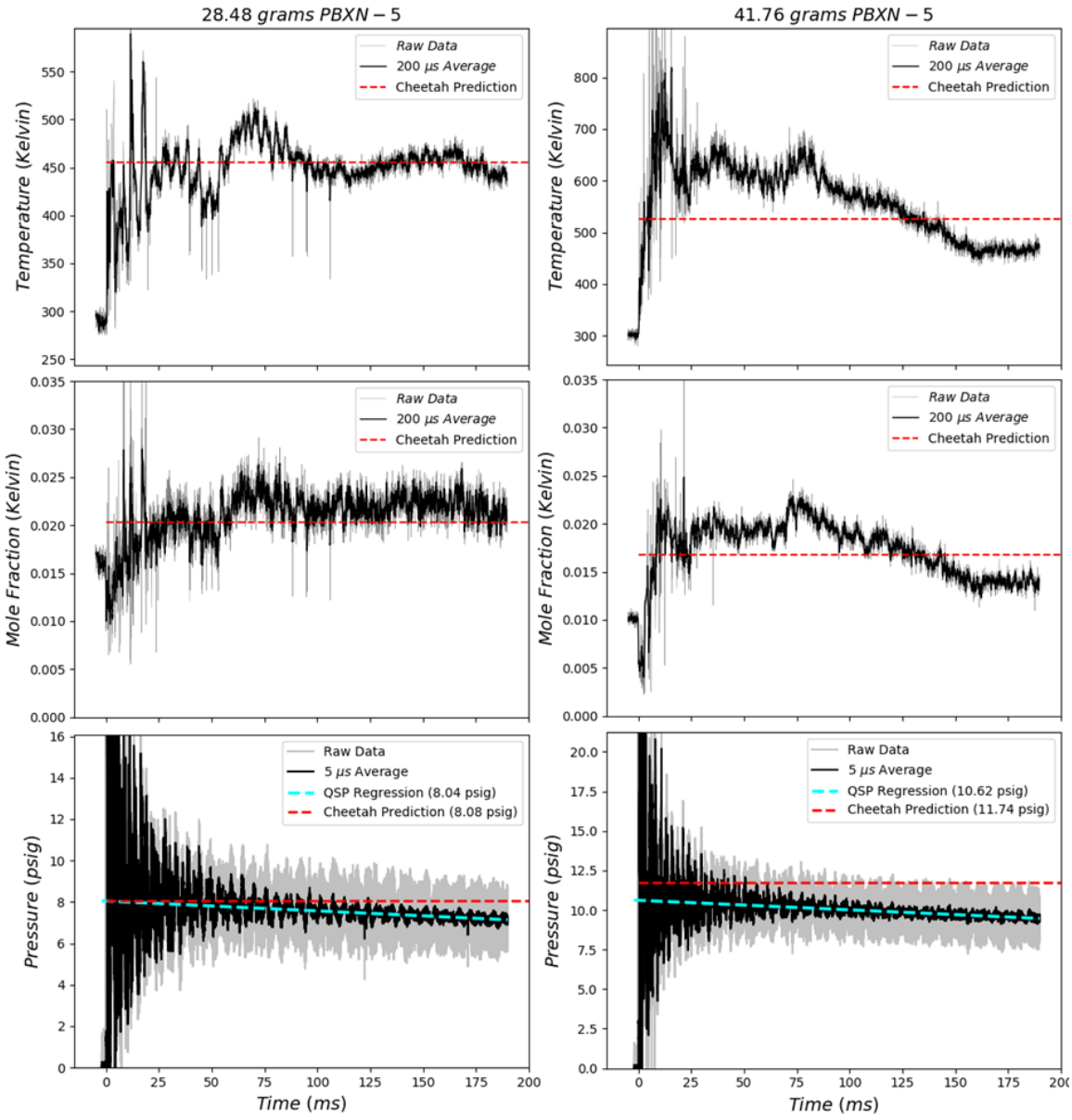

Figure 15: From top to bottom in each column, the temperature, water vapor mole fraction, and pressure from a 28.48 gram (left) and 41.76 gram (right) PBXN-5 explosive test. Scan rate was 30 kHz and probe was at a 21 inch standoff distance.

An important result taken from the temperature, pressure, and speciation curves is the characteristic differences between temperature and pressure. Given the comparatively

small explosive mass (40 grams) relative to the mass of air in the chamber (2120 grams), it would be tempting to assume an ideal gas relation between the two properties given the near constant number density in the chamber. While the temperature data shows very little adherence to the equilibration rate of the pressure, it agrees to a high degree with the characteristic behavior of water vapor concentration in all tests. This may be attributed to the arrival of detonation product gases. This observation also clearly depicts that the turbulent mixing and mass diffusion of hot explosive products is much slower to equilibrate than the global pressure.

2.6. Validation at Equilibrium:

Temperature is easily approximated at atmospheric conditions for verification of pre-trigger data, and shock front temperatures are calculable through pressure and Mach number relations. Given a lack of accurate predictive models in the intermediate phase of an explosion, it is difficult to validate the data collected in this regime. The Cheetah thermochemical code was used to calculate equilibrium conditions for the quasi-static temperature reached at the end of the 200 millisecond timeframe collected [74, 75]. This calculation is performed with knowledge of the charge size, detonator composition, volume of the chamber, and ambient mole fraction of water vapor. This software predicts a final temperature of 456 K and 526 K for charges of 28.48 grams and 41.76 grams, respectively that are presented in Figure 15.

It is important to note that the chamber is considered to be rigid and insulated in this analysis. However, the steel chamber itself has a substantial heat capacity and is at room temperature. Another note is that this software calculates a fully-combusted and mixed equilibrium, and therefore factors in the full oxidation of all carbon with oxygen in the chamber. As with many explosives, PBXN-5 is oxygen-deficient in its own structure and continued oxidation may not be completed in the time scale measured. In fact, it is clear when opening the chamber that there is carbon deposition throughout, a clear sign of incomplete oxidation, even though the chamber contains many times more air than is required for full oxidation of the charge.

In order to account for non-ideal chamber effects, the software prediction is also compared to the measured quasi-static pressures. This comparison is made by evaluating

the quasi-steady pressure at late time and regressing this information back to the initiation of the explosive. The purpose of the regression is to account for the minor leaks in the chamber and if wall heat transfer in the initial first few hundreds of milliseconds is relevant.

In the two explosive tests shown in Figure 15, there are two interesting features to note in the approach to equilibrium of the temperature profiles. The first is that both masses of explosive depict a "double-hump" at approximately the same time. This is believed to be due to the fact that these shots were tested back-to-back and so the location of charge and probe within the chamber were highly consistent with each other. The other fact is that the smaller mass of explosive achieved much more complete energy release with respect to equilibrium predictions. It was questioned as to whether this can be attributed to the same source of energy loss as the $\text{mass}^{2/3}$ scaling laws used for blast analysis, or whether the incomplete energy release is non-ideal, edge effects from the shape of the explosive charge at detonation. Both of these tests show that the thermochemical equilibration time was relatively long, so there remains questions as to whether a stabile temperature is reached by the end of data collected or before non-ideal energy losses will take place.

In a separate set of explosive tests with similar mass and configuration, the temperature, and concentration histories depict a different behavior. These data are shown in Figure 16. Shot-to-shot variation is not surprising considering the effects of turbulence, shock and chamber interaction, and other uncontrollable factors. These two tests however have very different approaches to equilibrium compared to those shown in Figure 15. Comparatively these do show an apparent stability in temperature with a sharp approach to it near 60 ms. Given this observation, a similar approach was applied to the measured temperature and concentration as was done to the pressure. That is, a linear regression of the stable values at later times was regressed back to time = 0.0ms and compared to full conversion predictions. In these tests, the behavior is fascinating. The temperature of the fireball remains well above equilibrium, likely due to mixing and/or ongoing aerobic combustion. It takes an almost linear cooling to the equilibrium prediction, and then very shortly after moves into a different, but still linear, continued cooling. It is unclear what causes this behavior, but both masses of explosive depicted the same trend. The late-time temperature decay (slope of the regression) was -89.5 K/s and -518.2 K/s for the 28.57g

and 40.63g, respectively. The pressure decay was -3.10 psig/s and -5.26 psig/s, respectively.

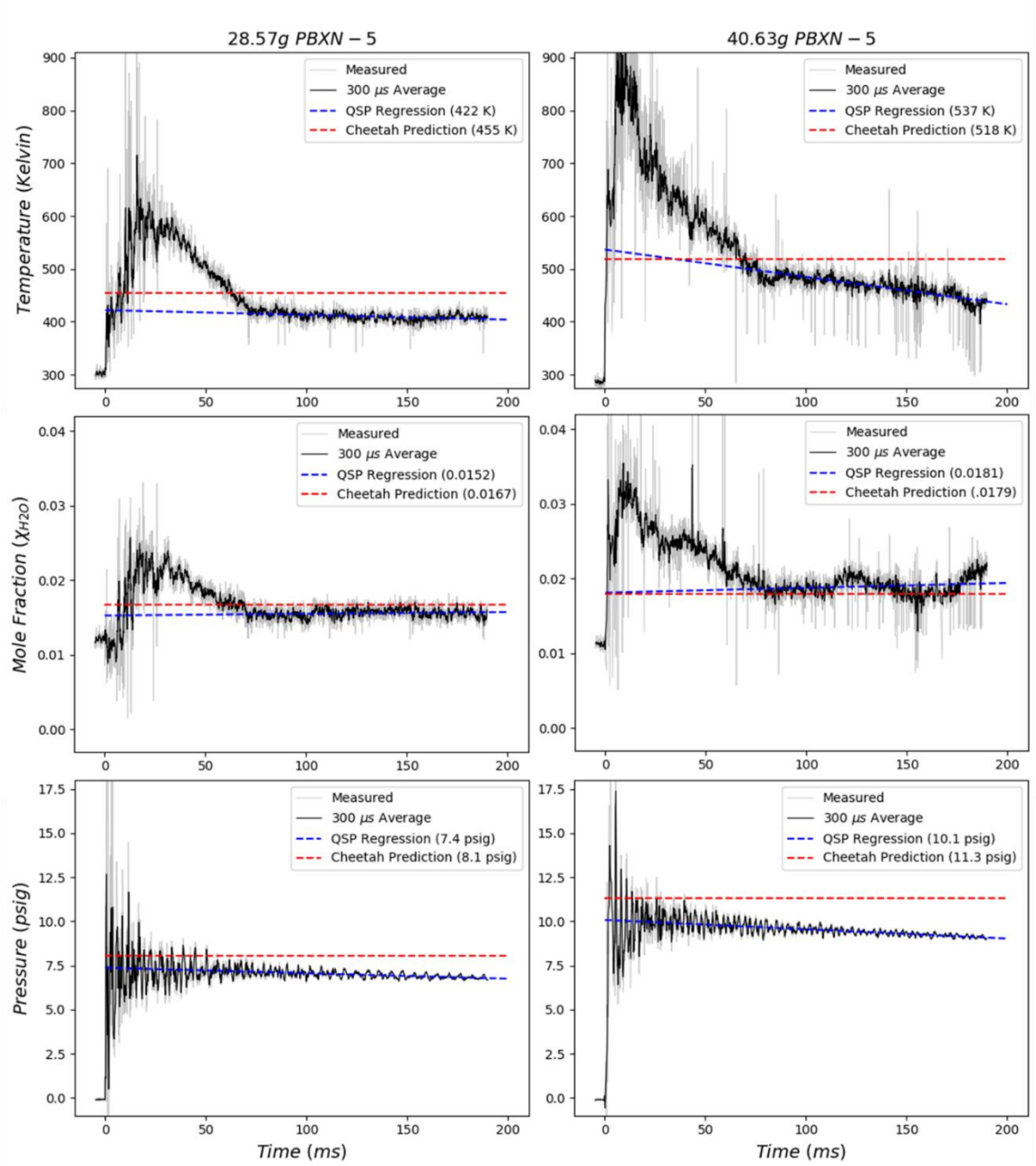

Figure 16: Secondary test series evaluating thermodynamic approach to equilibrium as a function of time. In each column, temperature (top row), water vapor mole fraction (middle row), and pressure (bottom row) for 28.57g PBXN-5 (left column) and 40.63g PBXN-5 (right column). Regressions from apparently stable QSP time ranges are regressed to zero (blue dashes) are compared to fully combusted and mixed equilibrium prediction (red dashes).

2.7. Variation of Explosive Mass and Type

Preliminary results of high explosive testing with this probe technique demonstrated its ability to measure temperature across the expanding shock wave in air, as well as characterize the approach to quasi-steady equilibrium [76]. These data also showed that acoustic equilibration times can be multiple times shorter than thermal ones. Chamber gases appeared thermally stratified past 150ms while pressure had stabilized prior to 50ms. Another key observation in this original work was that the smaller mass (28g PBXN-5) almost perfectly matched equilibrium predictions, while the larger mass tested (42g PBXN-5) showed signs of incomplete energy release in pressure, temperature, and speciation. This observation motivated the current study's cursory comparison of charge mass and explosive type (oxygen balance) on completion of energy release and fireball temperature histories.

In order to investigate this observation, additional explosive tests of two different masses of TNT, and Primasheet 1000® were tested in nominally the same manner as the PBXN-5 measurements previously described. The reason for testing these explosives is that they are structurally very diverse. The PBXN-5 is HMX based with an extremely high mass fraction of explosive. The TNT is purely explosive, but has a strongly oxygen-negative molecular structure. The PETN based Primasheet has a very oxygen balanced explosive, but a significant mass fraction of binders with heavily under-oxidized structures. Any reactants not converted in the detonation are limited to releasing their energy in the post-detonation fireball if possible. This aerobic portion of the fireball can represent a significant portion of the total energy release and is again the critical phenomenon in C-WMD applications. Example charges can be seen in Figure 17 and their relevant constituent properties are tabulated in Table 4 [77, 78].

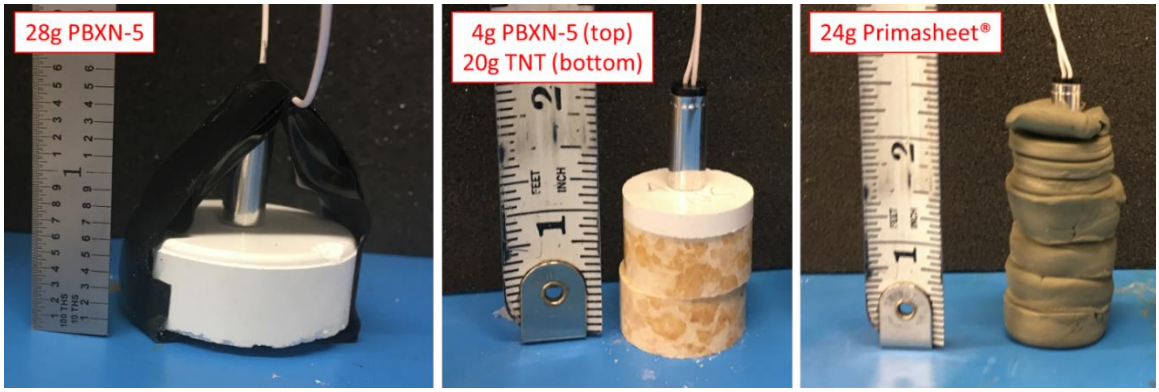

Figure 17: Examples of the charges used in the temperature measurement of fireballs driven by varied explosive type. PBXN-5 is shown on the left. Pressed TNT with a small PBXN-5 booster is shown in the center. A stack of 1" diameter, Primasheet cutouts is shown on the right.

	Explosive (% mass)	**Binder (% mass)**	**Oxygen Balance (%)**
PBXN-5	HMX (95)	Viton (5)	-24.2
TNT	TNT (100)	-	-74.0
Primasheet	PETN (63.5)	Citroflex (28.5) Nitrocellulose (8)	-63.9

Table 4: Collection of the relevant explosive properties for the materials tested with calculated oxygen balance

The oxygen balance was calculated using Equation 2.19 where X is the number of carbon atoms, Y is the number of hydrogen atoms, and Z is the number oxygen atoms in the compound [79].

$$OB(\%) = \frac{-1600}{Mol.Weight\ HE} * \left(2X + \frac{1}{2}Y - Z\right) \tag{2.19}$$

Figure 18 shows the results from these various tests. The six panes are temperature (left column) and water vapor concentrations (right column) with the top row as previously published tests for PBXN-5, the middle row is pressed TNT with a small N-5 booster, and the bottom row is highly polymerized Primasheet1000®. All charges were initiated with Teledyne RISI RP-80 detonators.

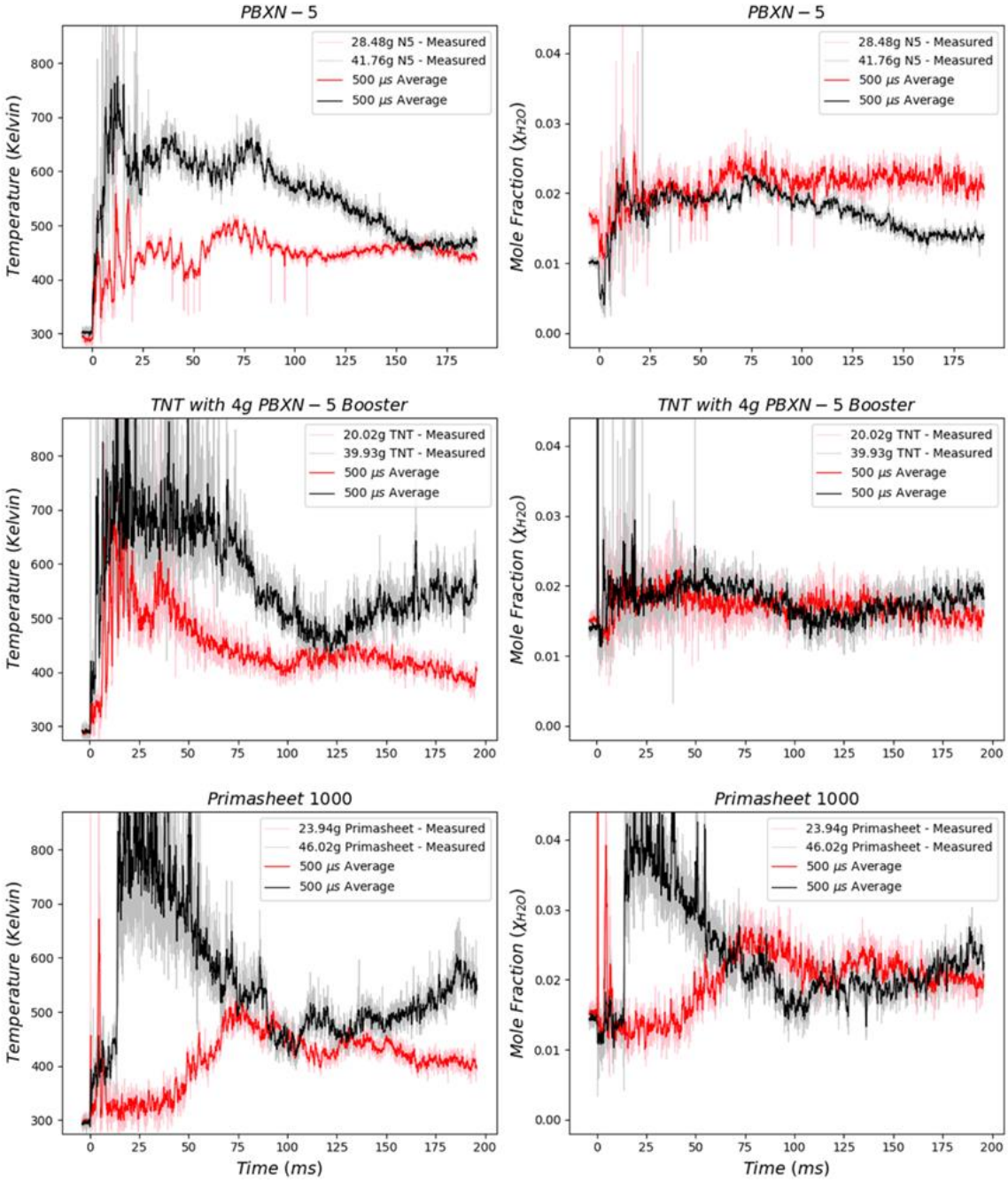

Figure 18: Six pane figure showing time-resolved temperature and water vapor concentration for two different masses of three different types of high explosive. Left column shows temperature. Right column shows water vapor concentration. Top row is PBXN-5, middle row is TNT, and bottom row is Primasheet 1000.

These data show extremely different fireball thermal histories. Data depict notable differences in both explosive type and mass. Early time behavior differs in the delay and rate of temperature increase. This is thought to be due to their individual oxygen

balances and constituents. PBXN-5 shows only a short delay between shock heating and slow rise in temperature attributed to product arrival. Comparatively, it can be seen that both TNT and Primasheet® depict a step-wise increase in temperature with the arrival of the shock wave, but then multiple milliseconds of stagnation prior to a second, sharp temperature rise associated with their explosive products and afterburn. In the case of TNT, the stagnation persists for approximately 3ms and 6ms for the large and small masses respectively. For the Primasheet, the delay was approximately 13ms and 40ms respectively.

All explosive tests have shown strong correlation between temperature and water vapor concentration (i.e. HE products). As PBXN-5 has very little binder, the damped rise and fall of temperature in that case was thought to arise from reflected shocks stagnating products near the center of the chamber and thus taking a longer time to reach the probe. The magnitude of the delayed temperature rise in the Primasheet® may suggest that the later arrival of thermal energy is not due to stagnated products, but instead is associated with the after burn of energy-dense hydrocarbon binder. This conclusion is also supported by the higher peak temperatures in this case, compared to the relatively modest peak temperatures of the PBXN-5. The measured global changes are reported in Table 5. The final properties were taken as the average of the last 20 milliseconds of data collected.

Explosive (mass, g)	**Measured ΔT (Kelvin)**	**Measured ΔX_{H2O} (E-3)**	**Measured ΔP (atm.)**
PBXN-5 (28.48)	156	5.1	0.55
PBXN-5 (41.76)	164	3.8	0.72
TNT[1] (20.02)	105	0.4	0.52
TNT (39.93)	259	4.5	1.00
Primasheet (23.94)	109	4.8	0.39
Primasheet (46.02)	261	8.5	0.84

Table 5: Tabulated global changes in the thermodynamic properties of the chamber as measured with the probe.

Data from the various explosives confirm that a significant amount of thermal energy is released in the post-detonation fireball. This is thought to be due to late time oxidation of binding agents and fuels not fully consumed in detonation. In addition, despite having ample oxygen available in the chamber, all metrics (T, P, X_{H2O}) confirm that complete conversion of reactants to products does not take place in the first 200ms.

In addition to the thermodynamic measurements already discussed, the application of diode laser gas sensing inside fireballs is always going to be subject to optical depth effects. That is, the nonresonant absorption and scattering that limits laser throughput in optically dense fireballs will be a major challenge with any of these diagnostics. Attenuation length scales can be extremely short (a few centimeters) in some fireballs, and therefore balancing path length to achieve sufficient resonant absorption above the background can be extremely challenging. The peak of each laser ramp is used as a metric of optical depth in a region with no selective absorption from atmospheric or

[1] TNT charges had 4.0g N-5 boosters in addition to the mass listed.

combustion gases are present. This metric is normalized to pre-trigger laser intensity, and corrected for path length to obtain a quantitative absorbance value. For the tests in the present work, the data are depicted in Figure 19.

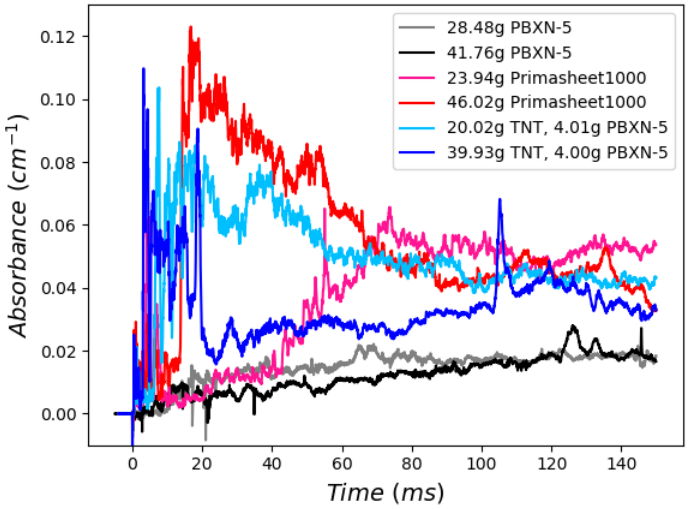

Figure 19: Non-resonant absorbance near 1390 nanometers in explosive fireballs generated by different types and masses of high explosive.

Attenuation length scales are governed by a number of factors, including scattering media size, temperature, and wavelength of light. These new data characterizing optical depth of fireball interior show that the more oxygen negative explosives have dramatically increased optical depth. This observation is not surprising considering soot formation due to competition for resources in the aerobic phase of the expanding and cooling fireball. In the cases of TNT and Primasheet, the peak absorbance of approximately 0.10 cm^{-1}, suggests 99% attenuation length scales of around 40 to 50 cm in this kind of test environment.

2.8. Accuracy and Uncertainty in TDL Temperature Measurement:

Due to the large number of convolved factors that affect the final values, it is difficult to quantify a universal uncertainty in calculated temperature and concentration. Slight variation in the alignment causes nonlinear distortion to the background. This necessitates the slight adjustment of background fit parameters between tests. The variation is caused by the angle and location that the beam intersects the optical components. Also, the

turbulence of the explosive cloud has consequences on the uncertainty of the results, due to the layers of varying density along with debris carried within the flow. These flow conditions are highly dynamic within a single shot, let alone shot to shot differences based on individual experiment factors such as location, exact orientation, and charge size. These flow conditions also produce a non-uniform temperature profile through the analyzed gas slab. Published analyses have shown that absorption measurements are extremely sensitive to colder temperatures [80]. As water vapor is both an ambient and explosive product, the temperature calculated is a path average skewed by the colder pockets of gas. This vulnerability will cause a lower temperature to be reported than explicitly those for explosive products.

In general, the largest hurdle to overcome in the realm of error minimization is the fitting of the background. As mentioned with alignment and flow conditions, the background is dynamic. The background fit, as described previously, is produced by a spline fit between two liner regressions. The parameters controlling this fit are set for each shot, and constant across a given test. However, the exact shape of the background deviates due to the variation in raw data outside of the water vapor absorption feature in each scan. Variation in this data can, therefore, affect how the background is fit near the spectra, causing error in the absorption depth. These errors, when significant, are thrown out as recognized outliers, but can be contained within the final data if the calculated temperature and mole fraction are within the bounds set for the experiment.

It is clear that the spread of calculated values is particularly sensitive at the extremes of the usable temperature range for this band. This is due to the fact that the calculated temperature is dominated by the two primary peaks at 7194.141 cm^{-1} and 7194.805 cm^{-1}. At ambient conditions, the 7194.141 cm^{-1} feature is exceptionally weak and, conversely, at elevated temperatures the feature at 7194.805 cm^{-1} is suppressed. This line sensitivity can result in absorption depths less than 1% for the weaker feature, as can be seen in Figure 20.

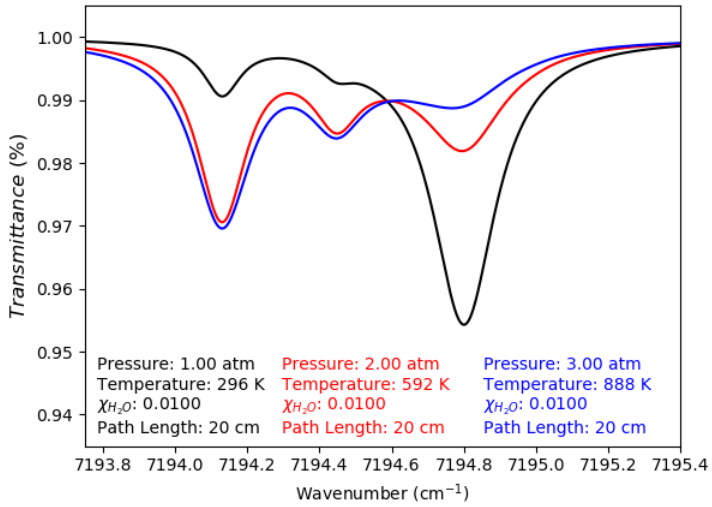

Figure 20: Simulated transmittance spectra spanning the spanning the temperature and pressure parameter space with a fixed mol fraction and path length.

As the temperature is roughly a function of the ratio between these two absorptions, it renders relatively low (< 300 K) and high (> 750 K) temperatures extremely sensitive to the accuracy of the background fit. The limits of temperature sensitivity for this diagnostic could be tailored to monitor a different temperature regime by selecting a different spectral band and utilizing a corresponding laser [33, 81].

Given these factors, it was determined that the most unambiguous way to provide some metric of uncertainty due to the hardware and data processing, was to calculate the standard deviation of the temperatures and mole fractions measured prior to detonation. This figure, while not a universal value applicable to all portions of the explosive event, provides a reliable metric for the minimum uncertainty in the final data. For the results reported in Figure 15, standard deviations for the temperature and mole fraction were found to be 7.3 Kelvin and 1.1×10^{-3} for the 28.48 gram explosive test and 6.2 Kelvin and 4.0×10^{-4} for the 41.76 gram explosive test, respectively.

2.9. Multiphase Temperature Measurements in Explosive Fireballs:

The true definition of temperature internal to explosive fireballs is vastly more complicated than a single measurement technique can resolve. Even barring the improbable case of non-equilibrated energy modes ($\Theta_{trans} \neq \Theta_{rot} \neq \Theta_{vib} \neq \Theta_{elec}$), there is bound to be thermal stratification between materials of different phases and level

of participation in the detonation. That is to say that product gases generated in the detonation will take time to mix and equilibrate with the ambient gases which were raised to the final temperature as opposed to cooling down to it. In addition, condensed phase sooting is produced in almost all high explosive testing and will lead to particulate that begins the event at very high detonation-level temperatures and subsequently cools through convective heat transfer to the surroundings. Even though hydrocarbon combustion systems are thought to produce small particulate (5nm-80nm), this phenomenon introduces another time scale for thermal equilibration to occur on [82]. Although not a factor in all explosives, metalized systems will have an additional reacting particle temperature and time scale which is well known to be a function of the particle size and combustion environment [83, 84, 85].

As a conclusion to this work but also the beginning of a much more rigorous diagnostic, the laser absorption gauge was retrofitted with a fiber bundle and collection optic schematically shown in Figure 21. The purpose for this addition was to allow the collection of emitted light from the same slab of gas being probed in absorption. This emission signal was then brought out of the probe and used in a 3-color pyrometer for a gray body temperature measurement. Although not demonstrated, further emission diagnostics that could be employed with this hardware are discussed in Section 4.2.

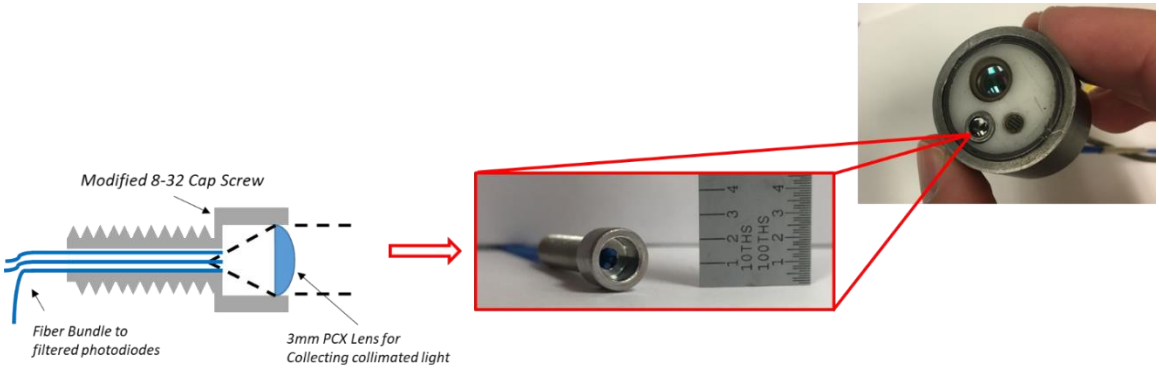

Figure 21: Schematic representation of highly compact, fiber optic collection system retrofitted to the laser absorption gauge to allow access to emission temperatures with nearly equivalent spatial resolution to the laser absorption temperatures.

The optic added is a customized 8-32 cap screw that mounted a 4mm diameter, 8mm focal length, plano-convex (PCX) lens (Edmund Optics, #45-225) to collect collimated

light onto a fiber bundle. Although scattering and reflection throughout the measurement media raises uncertainty about the source location of collected light in emission, the PCX lens was chosen so as to sample predominantly from the column of light immediately adjacent to that being probed with laser absorption. The fiber bundle was constructed of five, 400 μm core, 0.39 NA, multimode, low OH fiber (Thorlabs, #FT400EMT). Three of the five available fibers were coupled to amped silicon photodiodes (Thorlabs, #PDA36A) with 800 nm, 900nm, and 1000nm central wavelength bandpass filters (Thorlabs, #FB800-10, #FB900-10, #FB1000-10). All optical filters have a 10 nm FWHM.

Pyrometry as a temperature diagnostic has been thoroughly scrutinized for error and accuracy through numerous studies [86, 87]. The nuanced details of the technique are not the focus of this work. Instead, the present experiments are looking to successfully demonstrate the capability to conduct spatially resolved optical pyrometry in the novel probe presented here. The intended measurement is first order accuracy of condensed phase material temperature and equilibration time. A spectral model of the pyrometer configuration used in this work is shown in Figure 22. It can be seen that given the band selection, this pyrometer is going to be more useful for temperatures above 1500 Kelvin.

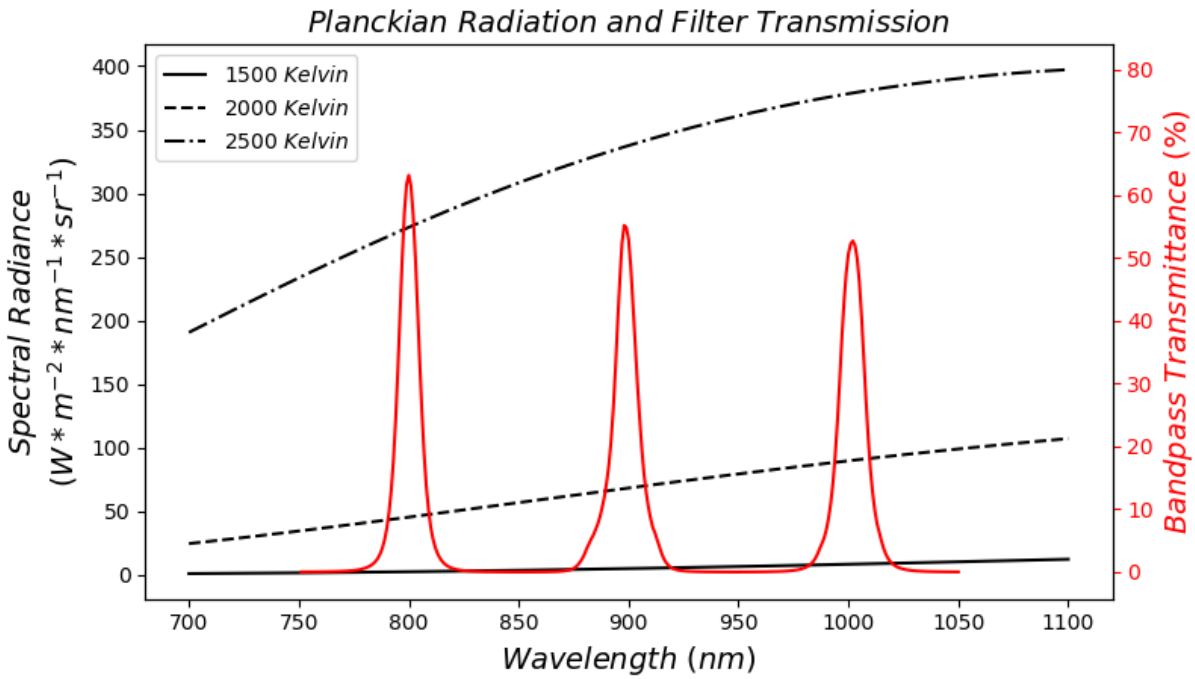

Figure 22: Spectral model of Planckian Blackbody radiation (black) in the spectral range of 3-color pyrometer. Optical filter transmission profiles provided by the manufacturer are overlaid in red.

The method used to calculate the temperature from measured intensities follows a derivation close to that of Bonefacic and Blecich without their application of the Wein approximation [88]. In some multi-color pyrometric methods (# colors > 2), the relative intensities are all simultaneously fit to a single Planck distribution. In this work, the data was reduced to three intensity ratios resulting in three temperatures which are averaged to report a cumulative temperature.

Although not a novel or comprehensive derivation of the technique, a brief summary and discussion of the calculations is presented here. The well-known equation for Planckian radiation is shown in equation 2.20, where $C_1$and C_2 are $2hc^2$ and $\frac{hc}{k}$ respectively. These coefficients are terms collecting Planck's constant h, the speed of light c, and Boltzmann's constant k. ϵ_λ is the emissivity term that can be a function of wavelength and temperature in theory.

$$E_\lambda(T) = \epsilon_{\lambda,T} \frac{C_1}{\lambda^5} \left(\exp\left(\frac{C_2}{\lambda T}\right) - 1 \right)^{-1} \tag{2.20}$$

Taking the ratio of Equation 2.20 at two different wavelengths but equal temperature results in Equation 2.21. The assumption of a thermally and spectrally independent emissivity is used here and allows its cancellation in Equation 2.21.

$$\frac{E_{\lambda 1}(T)}{E_{\lambda 2}(T)} = \left(\frac{\lambda_2}{\lambda_1}\right)^5 \left(\frac{\exp\left(\frac{C_2}{\lambda_2 T}\right) - 1}{\exp\left(\frac{C_2}{\lambda_1 T}\right) - 1}\right) \tag{2.21}$$

The relation between the ratio of emitted intensities at the source $E_\lambda(T)$ and the ratio of measured intensities at the detector $L_\lambda(T)$ are related through a temperature-independent transfer function A shown in Equation 2.22. This correction factor is a representation of the non-zero bandwidths of the filter, the spectral transmissivity of the material, and the efficiency of the detector. It is not a function of temperature.

$$\frac{E_{\lambda 1}(T)}{E_{\lambda 2}(T)} = A\frac{L_{\lambda 1}(T)}{L_{\lambda 2}(T)} \tag{2.22}$$

Rearranging Equation 2.22, plugging in Equation 2.21 and solving for A it can be seen that with a source of known temperature, A can be measured experimentally. The pyrometer in this work was calibrated with a quartz tungsten halogen lamp (Newport, 6332) with a published color temperature of 3300 Kelvin. The intensities of the calibration bulb were corrected for spectrally dependent emissivity with the manufacturer's provided irradiance assuming negligibly small area of collection optics at the half meter standoff.

$$A = \frac{L_{\lambda 2}(T)}{L_{\lambda 1}(T)}\left(\frac{\lambda_2}{\lambda_1}\right)^5 \left(\frac{\exp\left(\frac{C_2}{\lambda_2 T}\right) - 1}{\exp\left(\frac{C_2}{\lambda_1 T}\right) - 1}\right) \tag{2.23}$$

The final step in the calculation is to rearrange equation 2.23 and solve for temperature (T) in terms of the correction factor, A, and the measured intensity ratio $\frac{L_{\lambda 2}(T)}{L_{\lambda 1}(T)}$. This results in Equation 2.24 which can be seen as implicit and therefore solved iteratively.

$$T = \frac{C_2}{\lambda_1 \ln\left[1 + \frac{L_{\lambda 2}(T)}{L_{\lambda 1}(T)}\left(\frac{\lambda_2}{\lambda_1}\right)^5 \left(\frac{1}{A}\right)\left(\exp\left(\frac{C_2}{\lambda_2 T}\right) - 1\right)\right]} \tag{2.24}$$

Data from the 3-color pyrometer was reduced using a minimization routine that iteratively solves Equation 2.24 for temperatures. It is noted that temperature can also be explicitly calculated more simplistically using Wein's approximation as is presented by Bonefacic et al. Data and sensitivity analysis were compared to this method for verification.

The calibration of the pyrometer used a Newport QTH 6332 tungsten halogen bulb. The reason for using this source as opposed to a thermal blackbody cavity was that the published color temperature of the bulb is 3,300 Kelvin which is closer to the relevant range expected in explosive applications. The calibration was corrected for slightly non-gray behavior by using the manufacturer-supplied spectral irradiance data. The 10nm-spaced data was spline interpolated when needed. This process is quantitatively shown in Figure 23.

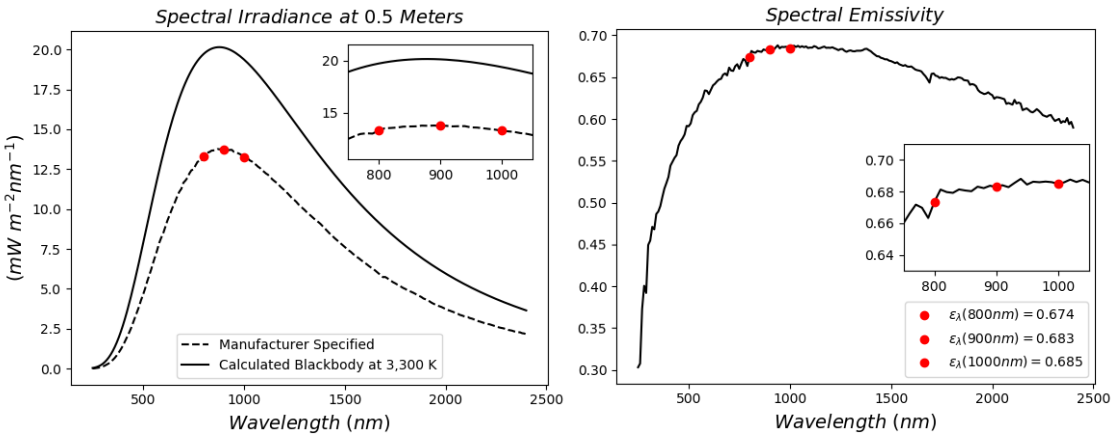

Figure 23: Quantitative illustration of the spectral emissivity correction that was conducted for slightly non-gray behavior of the Newport QTH 6332 tungsten halogen bulb. Red dot markers represent the 800, 900, and 1000 nm channels of the pyrometer in the present work.

The experimental procedure involved taking a background (no light source) and a calibration (tungsten halogen bulb) between each test. The reason for doing this was it was unknown if the calibration of the pyrometer would significantly change based on fouling of the collection optics or movement of the fibers in the explosion. After each test, the probe's optics are wiped clean to a reasonable level. A quantitative illustration of how pyrometer data is reduced is shown in Figure 24 with step-by-step data reduced from a 28.76 gram PBXN-5 shot with the probe mounted at a 20 inch standoff.

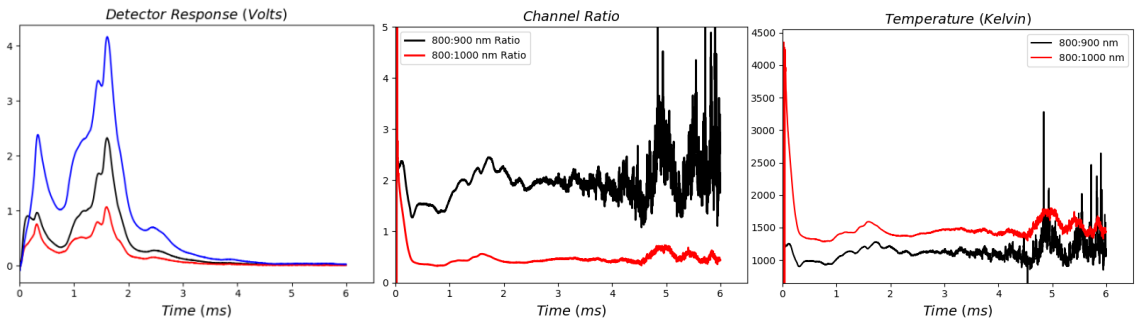

Figure 24: From left to right, the measured response on the three channels of the pyrometer, the two ratios that yielded meaningful temperatures, and the fully reduced temperature from the reflected light of the break out temperature.

It was shown after testing that the 900nm to 1000nm ratio is mathematically not an ideal design ratio for pyrometry. This point is presented and analyzed in the following section on uncertainty and errors. For this reason test data is reported only with the 800:1000nm and 800:900nm ratios. Many tests were conducted, but only two selected sets will be presented and analyzed here.

All of the data collected by the probe in a single shot is compared on a shared time axis in Figure 25 . From top to bottom, the top pane is the detector response of the pyrometer. The 2nd pane is the temperatures calculated from two of the ratios of the pyrometer. The third pane is the water vapor temperature as measured (and smoothed) at 30 kHz with the tunable diode laser. The 4th pane is the gauge pressure as averaged across each laser sweep. Note that at 33 microsecond averaging, the blast wave is accurate in time but not magnitude. The 5th pane is the water vapor concentration as measured by the TDL. The bottom pane is the peak of each laser ramp taken as the off resonant absorbance. This metric correlates to an optical depth measurement near 1390nm for non-resonant scattering and attenuation.

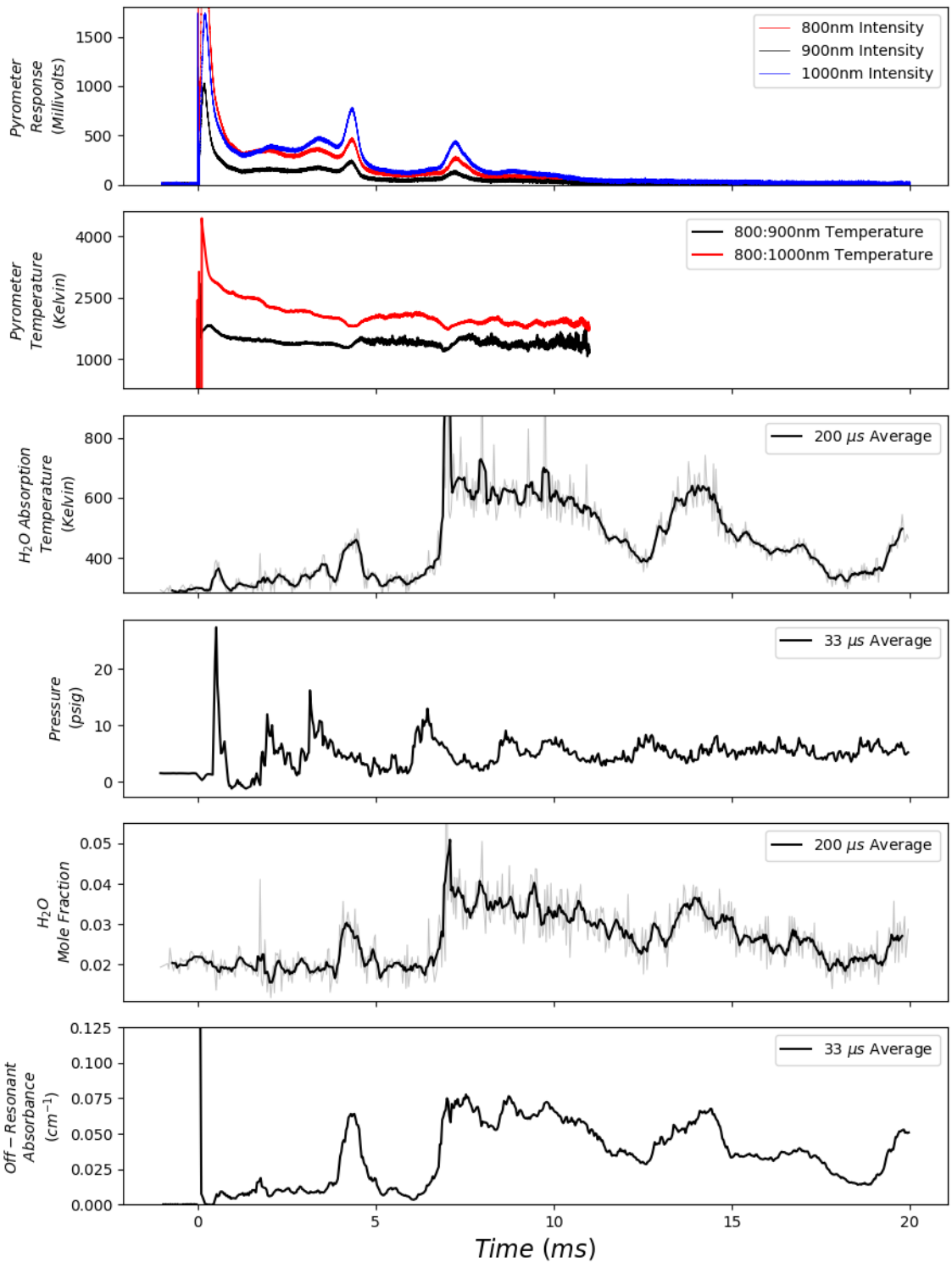

Figure 25: Single shot data collected by the probe for a sphere of 11.88 grams of Primasheet 1000 surrounded by 1.5 grams of loosely packed German Flake aluminum powder.

Interpretation of this amount of data requires a brief discussion of chamber and article configuration. One of the most critical observations was that almost all of the pyrometer signal was recorded prior to the permanent increase in off-resonant absorbance that is associated with condensed phase material arriving at the probe itself. This implies that despite the pyrometer being designed to interrogate emission from material in the path of the laser, it was actually measuring light diffusely reflected off the detector arm of the probe, and therefore caught the extremely high temperature flash of detonation and subsequent cooling as the post-detonation emitting material expands while being transported to the probe. The schematic shown in Figure 26 illustrates how the fixed position relative to the detonation source drives the temporally staggered measurements as they are received by the probe.

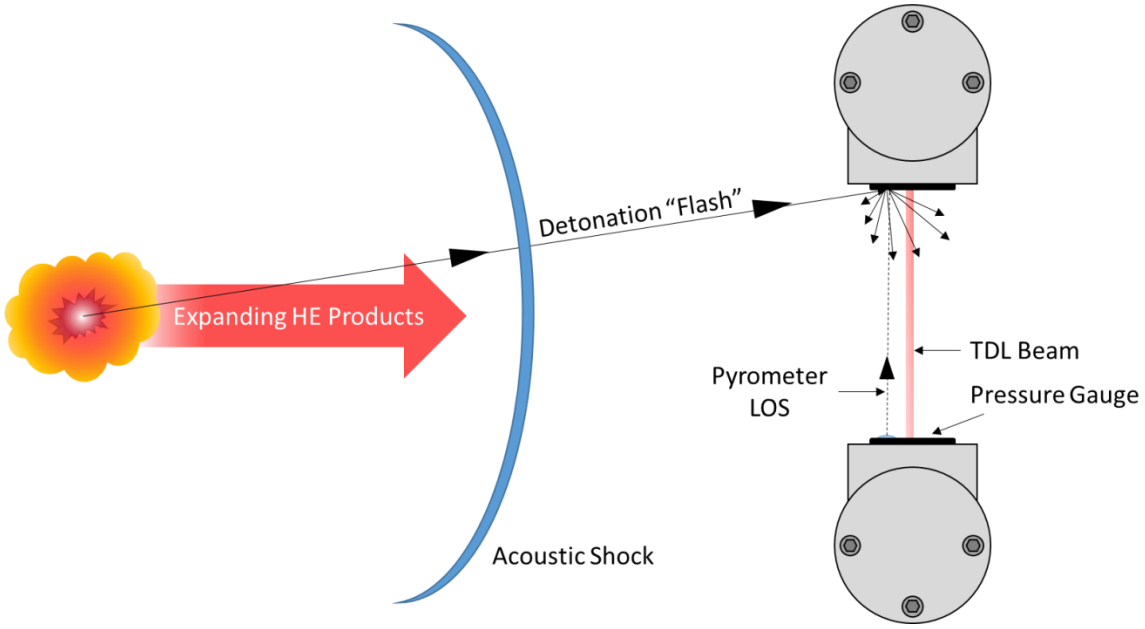

Figure 26: Top-down schematic illustrating the source of time dependence in the temperature, pressure, and speciation as they were measured in the probe for the multiphase temperature explosive tests.

With this initial interpretation on how the pyrometer data was received, a detailed analysis can be conducted. The following bullets reflect a selection of the analysis of the data set shown in Figure 25.

- The pyrometer saw the material emission temperature during a portion of the event before arrival of materials to the probe. Not the intended design, but a

surprisingly useful metric as it provides a nearly complete temperature-time history.

- The pyrometer, despite being optimized at higher temperatures, cools to within a few hundred kelvin (~1100 K) of what the laser absorption temperature measurement reads (~750 K) as the gas phase explosive products arrive at the probe. Given that the absorption temperature is path averaged across non-equilibrated ambient water vapor this level of agreement was surprising. This may suggest that the condensed phase material is equilibrated with the gas phase explosive products at this time.
- The shocked gas temperature was successfully measured with the arrival of the incident blast wave.
- Near 4ms, there is an arrival of material that contributed emission on the pyrometer and simultaneously attenuated the diode laser while also raising gas temperature and water vapor concentration.

2.10. Accuracy and Uncertainty in Pyrometric Temperature Measurement:

As previously mentioned, pyrometry as an optical temperature measurement technique suffers from several assumptions. One of these being the gray body behavior of the emitting material. It is also known that the final calculated values will be directly proportional to the accuracy of the radiometric calibration. To evaluate the effects these assumptions as well as additional sources of error introduce, a sensitivity analysis was conducted using several of the equations from Section 2.9 of this document.

The following analysis evaluates the ratio between radiometric intensity measured at 800 nm and at 900 nm as one of the three temperature calculations in this work did. Using Equation 2.24 and the actual implicit solution algorithm used to reduce data, Figure 27 was generated. What these data represent is the effect on calculated temperature from this ratio as function of error in the calibration correction coefficient. In addition, the error in calculated temperature that would be introduced using Wein's approximation is also shown.

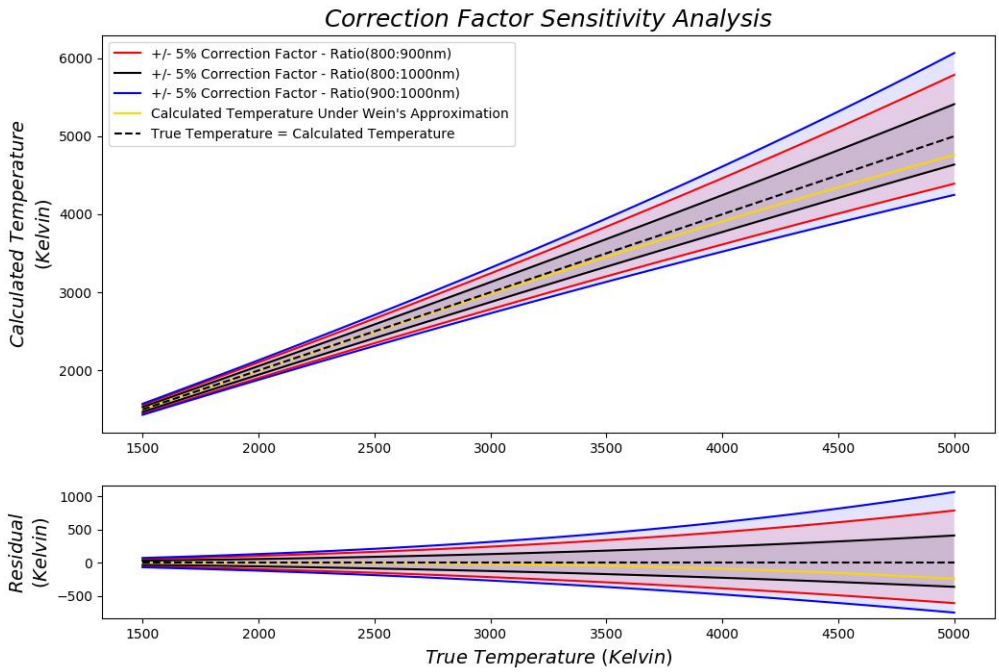

Figure 27: Envelope plot showing the effect on calculated temperature that ±5% error in the measured correction coefficient will introduce in the 800nm to 900nm ratio.

Following the observation that small errors in the correction coefficient can lead to 100's of Kelvin of uncertainty in the calculated temperature, it is pertinent to look at sources of error in the measurement and calculation of that value. As previously discussed and shown in Equation 2.23, the correction coefficient A is calculated by exposing the collection optics to a source of known temperature and spectral emissivity. In the present work, this was a tungsten halogen bulb with published color temperature of 3,300 Kelvin. As this temperature is not measureable in our lab, we assume from the manufacturer that operating the bulb at the appropriate voltage will reproduce their published quantities.

Using Equation 2.23 and taking all three ratios into this analysis, it is shown in Figure 28 that errors of a couple percent in the correction factor can be easily introduced if the bulb temperature was not actually at the defined 3,300 Kelvin.

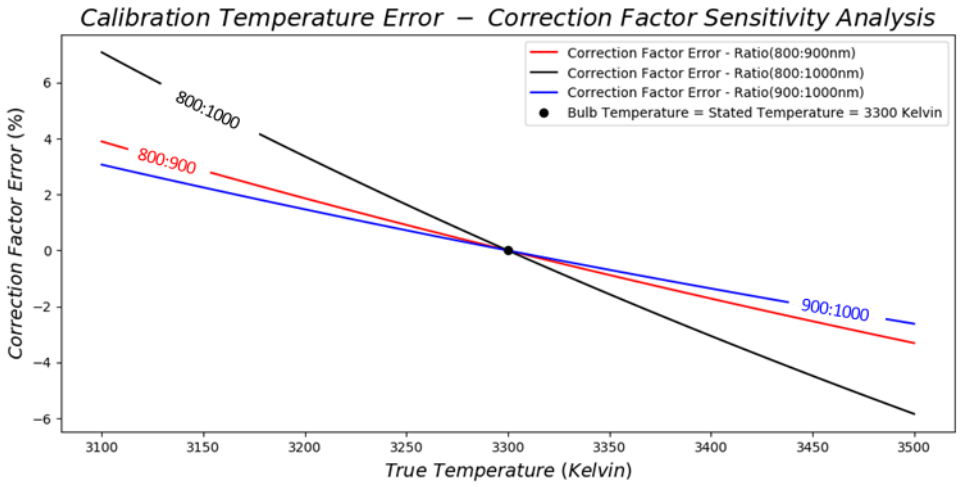

Figure 28: Error in the correction factor for the three ratios used for pyrometry in this work. The errors are shown as a function of true calibration temperature, but calculated using the published value of 3,300 Kelvin.

As was mentioned in the presentation of data for the pyrometer testing, the 900 nm to 1000 nm ratio proved to be highly erroneous due to the discontinuity in the equations. Looking at Equation 2.24, or Equation 10 of Bonefacic, it can be seen that there is a mathematical discontinuity in the equations relating intensity ratio and temperature. A sensitivity analysis under Wein's approximation shows the relationship between measured intensity ratio and the calculated temperature. This is illustrated theoretically (i.e. with no correction factor, A=1) as well as experimentally for the measured correction factors under Wein's approximation from the test shown in Figure 25 ($A_{800:900}$ = 0.2030, $A_{800:1000}$ = 0.7028, $A_{900:1000}$ = 3.4615) in Figure 29. In the range of temperatures of this test, the effect of Wein's approximation has a very minimal effect on calculated values, but the test data was still calculated by solving the implicit equation without it.

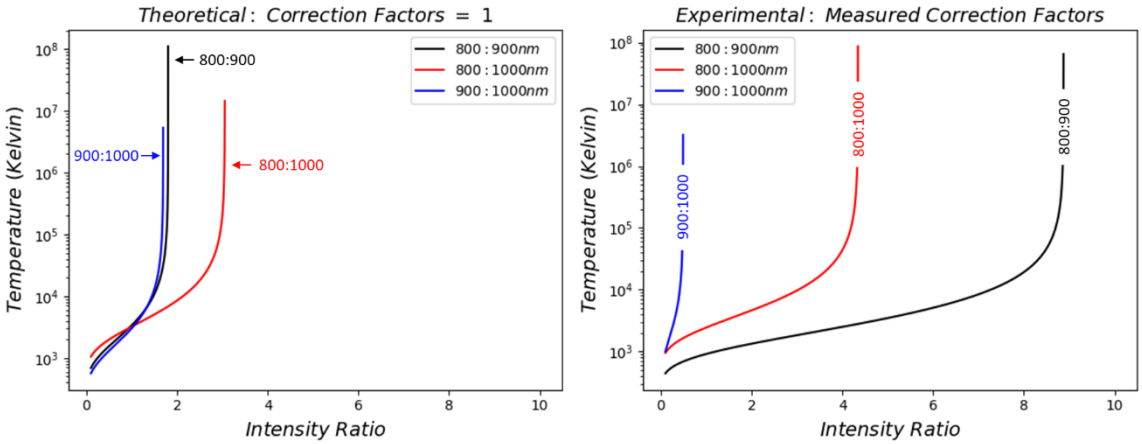

Figure 29: Theoretically calculated temperatures as a function of measured intensity ratio with no correction factor (i.e. A=1) (left). Calculated temperature as a function of measured intensity ratio with the application of experimental correction factors as measured in actual explosive testing during this work.

First looking to the mathematical discontinuity with no correction factors, it is illustrated that the ratio with 200nm separation has less sensitivity than those with only 100nm. This makes logical sense with Planckian behavior, and suggests that the 800:1000nm calculated temperature in this work is the most accurate. This is only true if the gray body assumption of soot holds at the larger separated wavelengths. This suggests that there is tradeoff between closely spaced wavelengths for more consistent spectral emissivity, and larger spaced wavelengths for more accurate temperatures. It can also be seen that the application of experimental correction factors helps improve the robustness of this technique against the discontinuity by shifting it to much higher ratios. The take away from this analysis is that the combination of 100nm spacing at longer wavelengths (900nm and 1000nm) with a large correction factor owing to the hardware led to this ratio not yielding meaningful temperatures. The asymptotic behavior at low ratios lead to unusable error as the noise in oscilloscope was sufficient to drive thousands of Kelvin of fluctuation.

In addition to these quantifiable errors, there must be a discussion of the unmeasurable ones in this technique. What is potentially the largest and most uncontrollable error is that which arises from the assumption of graybody emissivity in the condensed phase material. The condensed phase material could be incandescent soot (carbon) from binders

in heavily plasticized explosives. In metalized explosives, it could be aluminum oxide. In cased explosives, it could be dense fragment materials.

Material emissivity measurements are a dedicated dissertation in themselves. In the context of the present work, it is relevant only to acknowledge them as a probable shortcoming in the data collected thus far and present potential strategies for overcoming them in the future extensions of this work. An excellent study of the emissivity of soot (carbon) particulate at combustion relevant length scales (20 and 50 nm) and particle loading densities was published by Stull and Plass [24]. Another publication on the spectral emissivity of alumina with respect to optical pyrometry explicitly of explosive fireballs was published by Lynch et al. [25]. This study shows there is not only spectral and thermal dependence, but also particle size dependence. These variations in the emissivity propagate directly into the calculated temperature, and illustrate the complexity of assumptions in applied pyrometry. With particle agglomerations it can be difficult to estimate particulate size in even the most controlled explosive experiments.

When pointing a pyrometer at a large fireball, the soot has sufficient contribution path length to achieve optically thick conditions that likely better approximate gray body emissivity [14]. In comparison, the pyrometer in the probe was explicitly configured so as not to collect light from the entirety of the fireball. It was instead positioned between the two arms of the probe to interrogate the same material that was simultaneously being characterized with the laser absorption technique. This led to challenges of optically thin conditions with sufficiently cooled soot to not emit measurably from the volume of material between the arms of the probe. As the signal measured was actually reflected off of the arm of the probe from the early time fireball, there introduces a secondary spectral efficiency to factor in. That is, the spectral reflectance of aluminum which is unfortunately highly irregular around 800nm where the pyrometer was configured [89, 90].

CHAPTER 3: IODINE MEASUREMENT IN EXPLOSIVE FIREBALLS

3.1. Introduction to Atomic Iodine Measurement:

This chapter details the optical technique developed to monitor atomic iodine in biocidal explosions. To reiterate, the need for these measurement techniques is that iodine is a highly probable compound for use in prompt agent defeat strategies. Its biocidal properties make it a desirable material for chemically disabling spores such as anthrax or smallpox.

The effectiveness of the iodine will be proportional to the amount generated. In order to monitor the transient density of atomic iodine in practical explosions, novel diagnostic techniques and hardware were developed. This technology can be used to evaluate material performance and optimize iodized, agent defeat materials.

3.2. Atomic Iodine Monitoring Technique and Methodology:

In this diagnostic, a tunable diode laser was scanned over the F'=3 triplet of the hyperfine structure in the 1315 nm atomic iodine transition. These lines belong to the $^2P_{1/2}$ to $^2P_{3/2}$ transition coupling the ground and lowest-lying electronic states of neutral iodine (I^{127}). This transition is very well documented in the literature owing to its applications in chemical oxygen iodine lasers (COILs). This transition has a fairly complex structure, as the involved electronic energy levels are both split into hyperfine components due to the nuclear spin of 5/2. The splitting is well characterized by Tate et al. and reproduced for clarity here in Figure 30 [91].

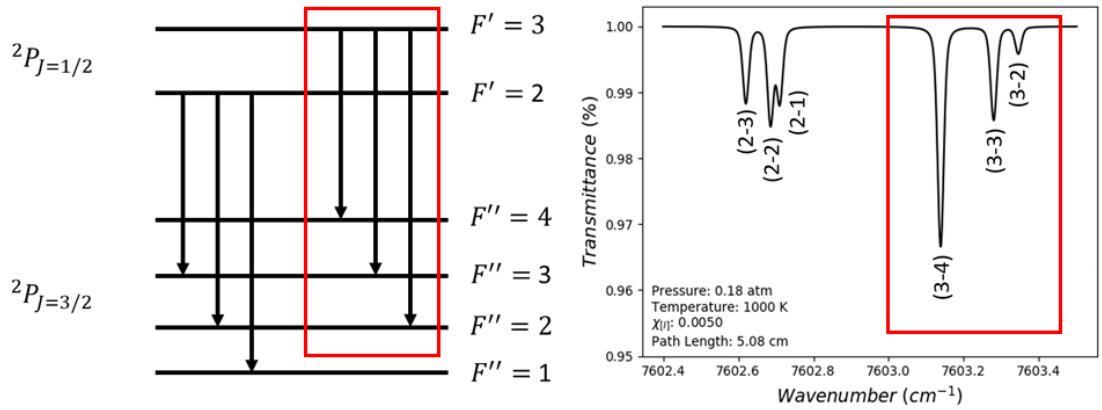

Figure 30: Energy level diagram (left) and a simulated, low pressure transmittance spectrum (right) of the hyperfine splitting in the $^2P_{1/2}$ to $^2P_{3/2}$ electronic transition in neutral atomic iodine [91]. *The triplet investigated in this diagnostic is boxed in red.*

3.3. Spectral Physics and Modeling of the 1315 nm Atomic Iodine Transition:

The transition line centers were calculated theoretically and measured experimentally by Tate et al. [91]. The experimental values were used in the present work. Lower state energy values, including the hyperfine distortion components, were taken from Zuev et al. [92]. Each F level is 2F+1 degenerate. The Einstein coefficients for each transition were calculated following the methodology published by Padrick et al. [93]. In summary, Derwent and Thrush published an integrated transition probability for all of the transitions between $^2P_{1/2}$ to $^2P_{3/2}$ of 5.9 s^{-1}, and similarly Zuev et al. published a value of 5.4 s^{-1} [44]. To partition that amongst the various hyperfine components, Padrick et al. takes the average of the two experimental values and multiplies this by the relative theoretical distribution published again by Zuev et al. For example, the F=3-4 transition has an Einstein A coefficient of 5.65 * (5 / 7.7) = 3.67 s^{-1}.

An approximation to the spectral line shape parameters was obtained by weighting published broadening coefficients for specific gases with standard atmospheric mole fractions (78% N_2, 21% O_2, 1% Ar) to mimic the standard HITRAN tabulated air-broadening coefficient [45, 46, 53]. Some values were converted from full width at half maximum, to half width at half maximum in order to be consistent with HITRAN formatting. A temperature scaling coefficient of 0.99 was used as the T^1 scaling closer related the extrapolated measurements of Engelman [45] to those published by Davis et

al. [46]. All hyperfine transitions were assumed to share the same broadening coefficient as those published for the (3-4).

Collision Partner	Broadening Coefficient (cm^{-1}/atm.)
O_2	0.06338
N_2	0.06971
Ar	0.06464
I	0.05450
I_2	0.1306

Table 6: Summary of partner-specific broadening gases obtained from the literature and used to create more commonly available air- and self-broadening coefficients for spectral line shape functions. Molecular Iodine broadening coefficient is included as well.

The summary of properties collected from various sources and used in simulations and calculations of the current work are presented in Table 7.

Transition (F'– F")	Line Center (cm^{-1})	Lower Energy (cm^{-1})	g'	g"	Einstein A_{ul} (s^{-1})	γ_{air} (cm^{-1}/atm.)	γ_{self} (cm^{-1}/atm.)
(2 – 3)	7602.6202	-0.02800	5	7	1.76104	0.0683	0.0545
(2 – 2)	7602.6858	-0.09400	5	5	2.20130	0.0683	0.0545
(2 – 1)	7602.7104	-0.11800	5	3	1.68766	0.0683	0.0545
(3 – 4)	7603.1384	0.11300	7	9	3.66883	0.0683	0.0545
(3 – 3)	7603.2794	-0.02800	7	7	1.54091	0.0683	0.0545
(3 – 2)	7603.3450	-0.09400	7	5	0.44026	0.0683	0.0545

Table 7: Transition properties of the hyperfine splitting in the $^2P_{1/2}$ to $^2P_{3/2}$ electronic transition in neutral atomic iodine. Gamma values correspond to the air- and self-broadened Lorentz half width at half max in line with the HITRAN database style.

To validate these spectral parameters, we compare a quantitative model to some of the high resolution spectra with experimental gas cell parameters reported in the literature, as well as our own experimental data which is shown in Figure 31 [45].

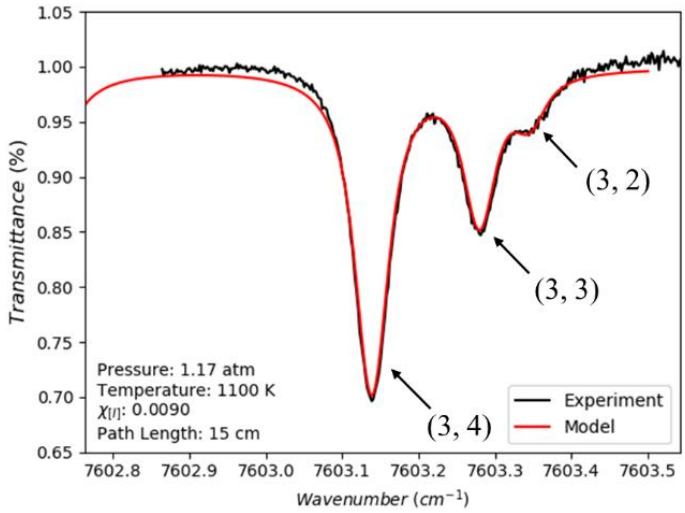

Figure 31: Sample comparison of spectral model and experimental data using values from Table 6 and Table 7. Structure is the F'=3 triplet of the 1315 nm atomic iodine absorption line. Model is shown in red, and experimental data from explosive test is shown in black. Pressure was measured, and temperature was inferred. Hyperfine triplets are labeled by (F', F")

3.4. The Partition Function of Atomic Iodine:

Calculation of the lower state number density by means of the Boltzmann fraction typically requires the total partition function to be evaluated. I^{127} has a spin quantum number of 5/2 and therefore a nuclear contribution to the statistical weight. The total degeneracy of each J electronic state is given by the product of nuclear and electronic degeneracies. This product is also equal to the summation of hyperfine degeneracies for each F state within a given J state. This is expressed in equation 3.1.

$$(2I+1)(2J+1) = \sum_{F} (2F+1) \tag{3.1}$$

From the NIST Atomic Spectral Database, the second excited electronic level of neutral I^{127} has an energy of 54,633.46 cm^{-1} which corresponds to a characteristic temperature of approximately 78,600 K [94]. This is sufficiently high to neglect contributions to the total partition function. Drawing on this, the partition function can be calculated numerically using the hyperfine energy level values from Zuev et al. [92].

The partition function is always a function of temperature. However, without an accurate method to quantify the explicit temperature of the absorbing atomic iodine during the reaction, it cannot be directly evaluated. Shown in Figure 32 is the total internal partition sum for atomic iodine. It was calculated with a direct summation over the J electronic levels as tabulated by NIST, as well as a direct summation over the hyperfine states in Table 7 to verify the contributions from hyperfine degeneracy. The red dots represent a direct numerical summation taking the hyperfine levels as 2F+1 degenerate. The solid black curve represents a direct summation over 2J+1 degenerate electronic states with the multiplied 2I+1 nuclear term representing the 5/2 spin contribution [94].

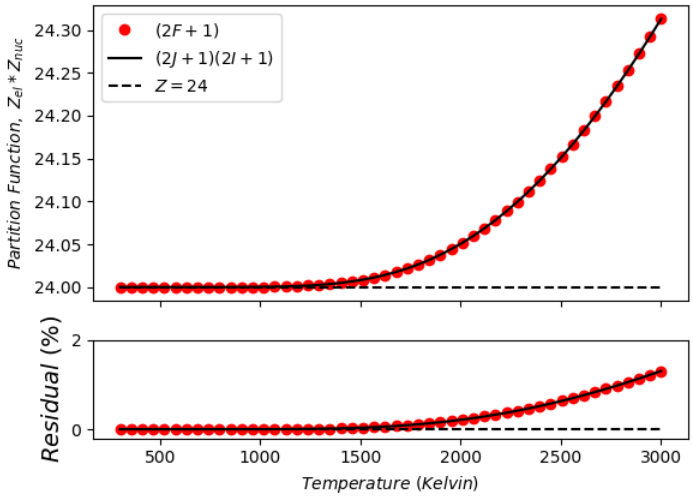

Figure 32: Atomic Iodine partition function calculated with two different sets of quantum numbers. Shown in red is the direct summation over the 2F+1 degenerate hyperfine levels. Shown in black is direct summation over the 2J+1 degenerate electronic levels with the 2I+1 nuclear degeneracy. Dashed line represents the partition sum at 0 Kelvin. Residual represents the percentage difference of true partition sum from fixed value of Z=24.

The two separate computations verify the absolute value of the sum, as well as demonstrate that for this particular atom, the total partition function is not a strong function of temperature. That is, the absolute value of the partition function does not change substantially over the range of temperatures expected in these explosions. At 1500 K, the deviation of true partition function value from a fixed value of 24 taken at STP is 0.03%. For this reason, the partition function can be considered temperature-

independent in this work, and is taken at a value of Z=24 without introducing substantial error.

3.5. Quantification of Atomic Iodine in Practical Applications:

To reduce the spectra to a quantified number density in these experiments, some approximations were needed. Those approximations and the errors that they introduce are discussed here. The lower state energies for atomic iodine, although spin-split, are not separated by substantial energy. This makes temperature measurement not possible with the relative population of the hyperfine components. In principle, the line shapes can be fit to a temperature. However, this will be limited by the accuracy of the broadening model, background fit, and instrument resolution. To avoid such limitations, a numerical integration approach is applied in this work.

In addition to the partition function, the Boltzmann factor for each lower state population fraction has a temperature dependence. Fortuitously, these transitions are absorbing from the ground electronic state where energy ~ 0 cm^{-1} and so the $\exp(-E_i/k_BT)$ term is very close to 1 and the population fraction is solely proportional to the 2F+1 degeneracy of the lower level involved in the transition. The combination of the temperature-insensitive partition function and population fractions enables direct quantification of total iodine number density without knowledge of material temperature.

With the limitation of the TDL only having sufficient bandwidth to scan over the F'=3 triplet, the process used to quantify total number density needed to reflect that fraction of the total electronic transition. In addition, the triplets are not distinct at atmospheric or above pressures, and so an integrated approach is necessary. The number density of atomic iodine was calculated with equation 3.2 which is derived later in this section.

$$n_{iodine} = 24\left[\frac{\left(\frac{cW_{lu}}{h\tilde{\nu}B_{lu}L}\right)}{g_i + g_j + g_k}\right] \tag{3.2}$$

W_{lu} is the integrated absorbance over all three hyperfine transitions shown earlier in Figure 31. B_{lu} is the summation of all Einstein B coefficients for the F'=3 transitions being scanned over. As the integrated absorbance includes contributions from all three

hyperfine states, $g_i + g_j + g_k$ is the summation of all 2F+1 degeneracies of the hyperfine components in the blended triplet structure. The partition function is taken at a fixed value of 24, L is the path length, c is the speed of light, and $\tilde{\nu}$ is the transition wavenumber as defined in Equation 3.3. Although a negligibly small correction, this formula statistically weights the triplet's line center by the number of atoms making a given transition.

$$\tilde{\nu} = \frac{g_4\tilde{\nu}_4 + g_3\tilde{\nu}_3 + g_2\tilde{\nu}_2}{g_4 + g_3 + g_2} \tag{3.3}$$

A brief derivation of Equation 3.2 is presented here with the transitions F',F'' = (3, 4), (3, 3), and (3, 2) labeled i, j, and k respectively. The quantification was derived from the statistical contributions of each hyperfine level.

Hyperfine Population Fractions in the i, j, and k Components of Ground State ($E_{i,j,k} = 0$ cm^{-1}):

$$n_i = \frac{n_T}{Z}\left[g_i \exp\left(\frac{-E_i}{k_B T}\right)\right] = \frac{n_T}{Z} g_i$$

$$n_j = \frac{n_T}{Z}\left[g_j \exp\left(\frac{-E_j}{k_B T}\right)\right] = \frac{n_T}{Z} g_j \tag{3.4}$$

$$n_k = \frac{n_T}{Z}\left[g_k \exp\left(\frac{-E_k}{k_B T}\right)\right] = \frac{n_T}{Z} g_k$$

Mathematically Combined Number Density in the i, j, and k states:

$$n_i + n_j + n_k = \frac{n_T}{Z}\left(g_i + g_j + g_k\right) \tag{3.5}$$

Integrated Number Density in the i, j, and k states [29]:

$$n_i + n_j + n_k = \frac{cW_{lu}}{h\tilde{\nu}B_{lu}L} \tag{3.6}$$

Integrated, Total Number Density (Equating 3.5 and 3.6):

$$\frac{n_T}{Z}\left(g_i + g_j + g_k\right) = \frac{cW_{lu}}{h\tilde{\nu}B_{lu}L} \tag{3.7}$$

Total Number Density (Partition Function, Z=24):

$$n_T = 24\left[\frac{\left(\frac{cW_{lu}}{h\tilde{\nu}B_{lu}L}\right)}{g_i + g_j + g_k}\right]$$

The presence of the integrated degeneracy in the final form seems surprising in contrast to the form of this equation in Laurendeau's text [29]. That being said, its presence is actually necessary for agreement between Zuev [92] and Simeckova [95] in that each of the triplets have separate transition probabilities equal to the total J electronic state owing to the non-additive properties of Einstein A coefficients expressed in Equation 3.7 [95].

$$A_{e'v'J'-e''v''J''} = \frac{1}{d_{J'}}\sum A_{e'v'J'F'-e''v''J''F''} \tag{3.8}$$

In the case of atomic iodine, the $\frac{1}{d_{J'}}$ is ½ because the multiplicity of the excited J state is 2. This equation also agrees with Zuev's theoretical distribution of the probabilities.

3.6. Small Scale Testing of Spark Ignited Thermite Dust Explosions:

Preliminary iodine testing was conducted at the milligram scale in the 2.18 L agent defeat blast chamber at the University of Illinois at Urbana-Champaign Energetic Materials Diagnostics Lab. Photographs of the chamber can be seen in Figure 33. These sub-gram scale dust explosions were variations of reactant size, stoichiometry, chamber atmosphere, and initiation mechanisms involved in aluminum iodine pentoxide (Al, I_2O_5) thermite.

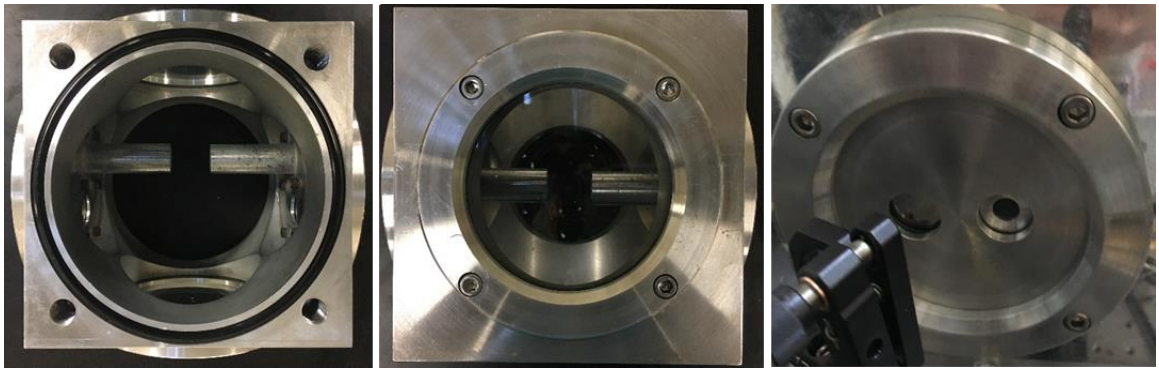

Figure 33: Photographs of the 2.18 liter agent defeat blast chamber. Top-down image of the interior of the chamber (left). Side-on optical axis port for reference imager (center). Side-on laser access ports for mounting wedged CaF2 windows and path length reducers (right).

In addition to the atomic iodine monitoring laser, tests were conducted with the water vapor temperature diagnostic, a Phantom 5 high-speed reference imager, and a piezoresistive pressure transducer. The placement of these diagnostics relative to the agent defeat chamber are shown in Figure 34.

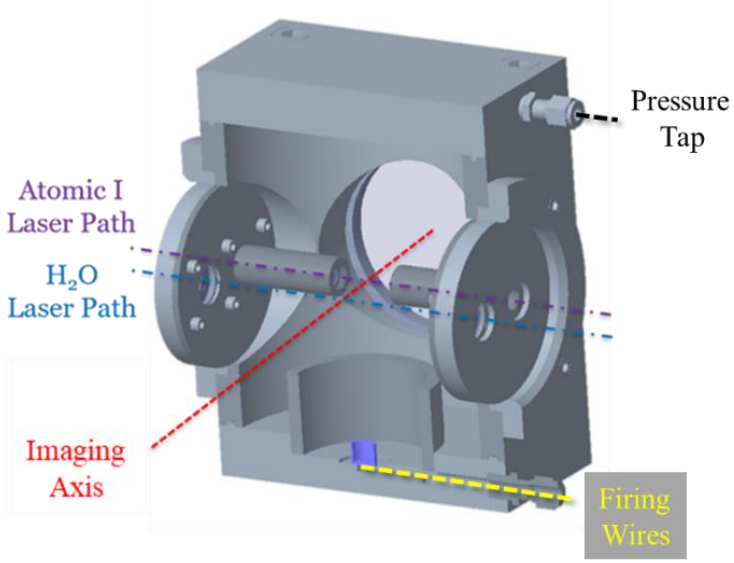

Figure 34: Schematic of the 2.18L agent defeat chamber with sketched paths of the utilized diagnostics. The atomic iodine laser was pitched through the path length reducers that can be seen in the cutaway model.

A sample data set collected in this type of benchtop test is shown in Figure 35. The dust explosion is clearly concentrated in the center of the chamber. This spatial dependence can lead to number densities measured above the equilibrium concentration under a homogenous chamber assumption.

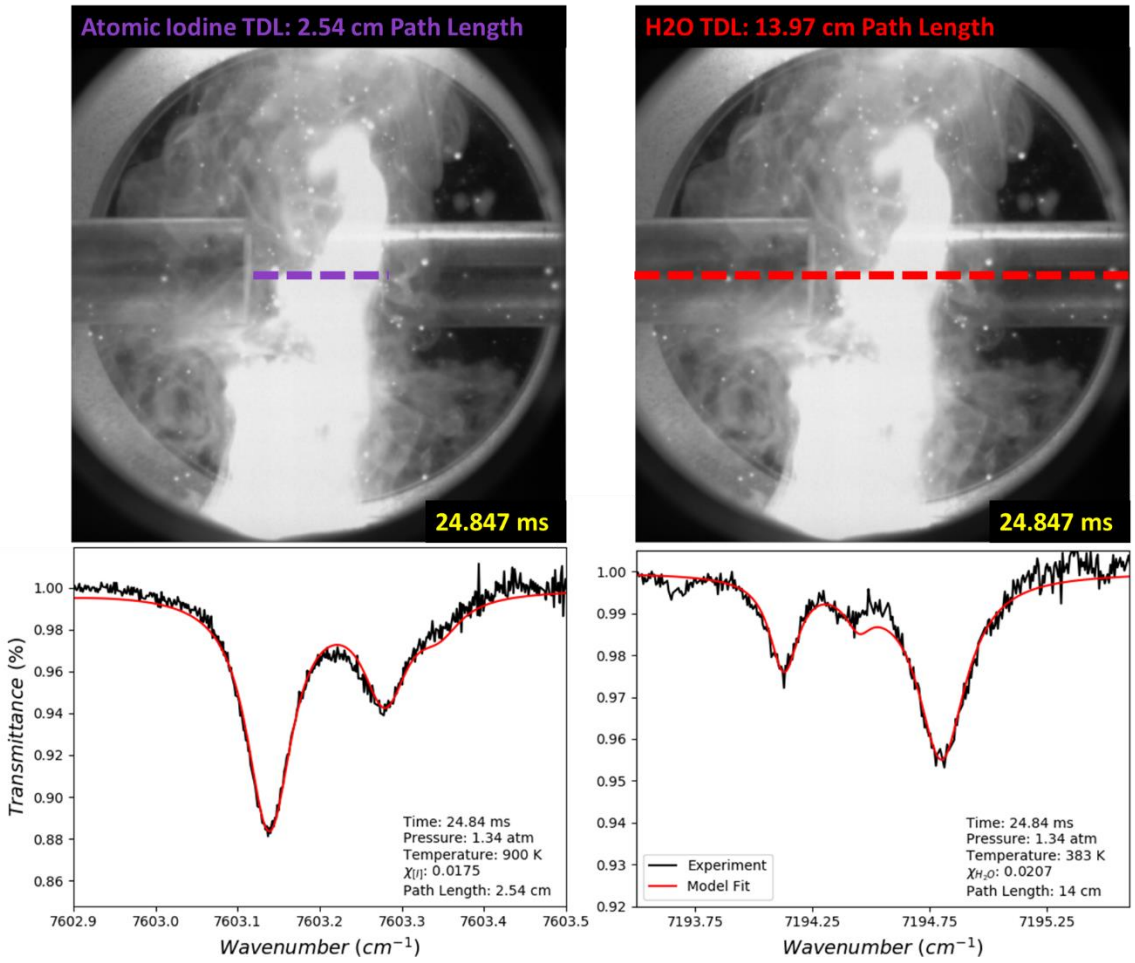

Figure 35: Data from an iodine pentoxide, aluminum, and potassium perchlorate dust explosion. Phantom 5 reference image with overlaid atomic iodine tunable diode laser (TDL) beam location (top left). Phantom 5 reference image with overlaid water vapor beam location (top right). F'=3 atomic iodine spectrum fit to theoretical model (bottom left). Water vapor spectrum fit to theoretical model (bottom right). Spectra correlate to image in time with less than 10 microsecond difference.

To demonstrate the capability of these diagnostics, a comparative study discriminating the performance of differently sized aluminum iodine pentoxide thermites was conducted. Results from this comparison are shown in Figure 36. It should be noted that spark ignition of these thermite contributes no substantial amount of hydrogen nuclei from the fuel or oxidizer. This implies that the temperature measured from the water vapor spectra represent the raising of ambient chamber gas through thermal diffusion with the combustion products.

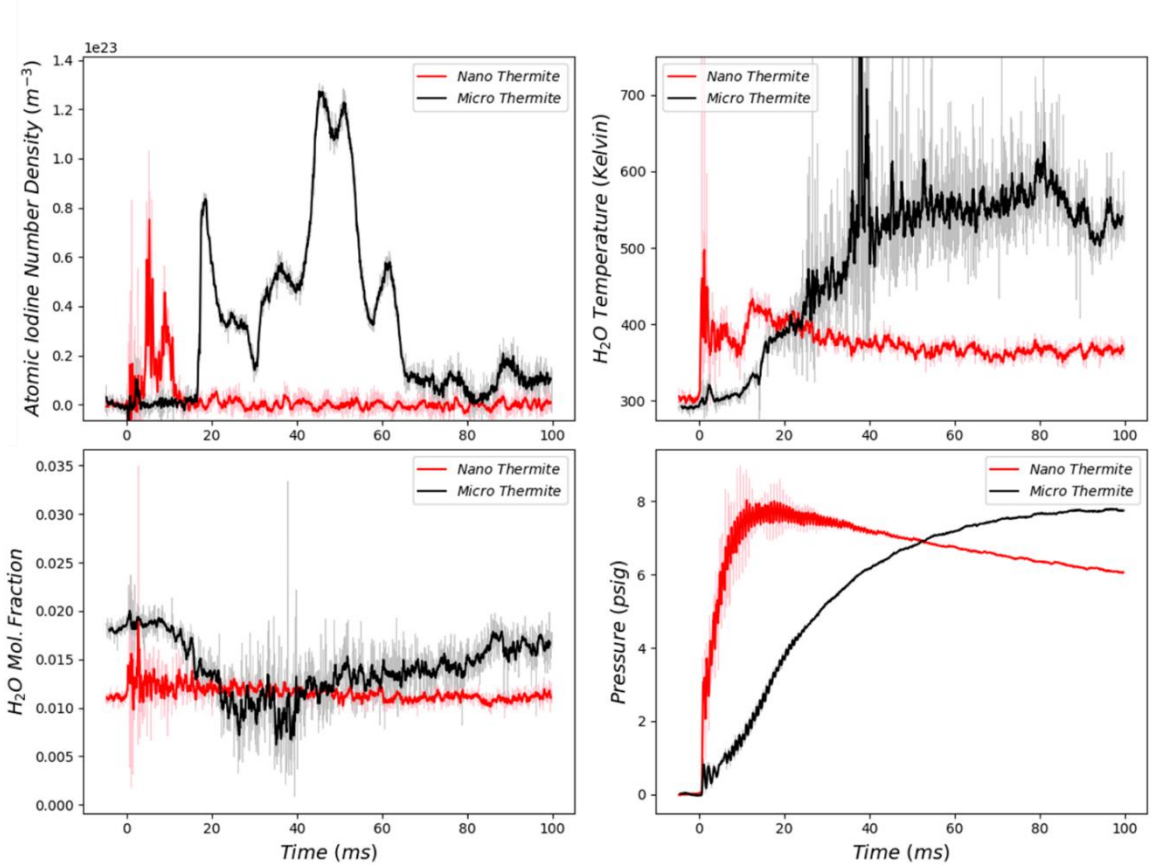

Figure 36: A composite of temporally resolved atomic iodine number density (top-left), water vapor temperature (top-right), pressure (bottom-left), and water vapor mole fraction (bottom-right) in both nano- and micro-scale thermite reactions.

It can be seen in all thermodynamic metrics, the micro thermite reacted on a slower timescale compared to the nano fuel mixture. This is not surprising given the well documented combustion timescales associated with aluminum particles of different sizes. What is surprising is that with identical masses of halogenated oxidizer, the micron sized thermite appears to have generated substantially more atomic iodine.

Data suggest that in spark initiation, this thermite system remains dependent on the ambient oxygen to propagate a dust explosion as opposed to reacting with the I_2O_5. If nano-scale fuel particles are burning with the ambient oxygen, then the halogenated oxidizer will remain unreacted in a non-biocidal format. To investigate this phenomenon, nano thermite tests were conducted in a Nitrogen (N_2) purged chamber and compared to the equivalent test done in air. We interpret that the inert atmosphere test quantifies the portion of iodine generation from explicitly the thermite reaction, while the air-only shot

represents that concentration in addition to the added iodine release from the subsequent thermal decomposition of I_2O_5 during a dust explosion. This hypothesis is supported by the repeated failure in ignition of micro-scale thermites in inert atmosphere. These data confirm that completion of the halogen release will be a strong function of the surrounding environment as well as fuel particle size.

3.7. Scaled up Testing of Explosively Initiated Iodized Thermite Reactions:

Building on the results from benchtop testing of spark-initiated dust explosions, larger scale tests were conducted in the 1800-liter blast chamber. These tests were conducted in order to demonstrate diagnostic capability in a test that more closely replicates the true conditions of an iodized, explosive detonation. In order to monitor the transient presence of atomic iodine, the hardened gauge was utilized with the 1315 nm TDL, thus confirming the previous claim that the probe is generic and can readily monitor a different species with minimal modification. Analogous to the benchtop experiments, scaled up explosive tests were conducted with both nano and micro aluminum iodine pentoxide as well as varied initiation geometry.

In addition to the hardened gauge for fielding the atomic iodine TDL, standard explosive diagnostics available in the 1800-liter blast chamber were also leveraged in this campaign. Two of these are 4-channel, Cooke high-speed framing cameras (HSFCs) that provide article “break out” images and visible emission spectra. The details of these diagnostics are thoroughly discussed in the Ph.D. thesis by Michael Clemenson [96]. In addition, a Phantom 5, CMOS high-speed camera was used to image a wider field of view and longer duration of the post-detonation fireball. A schematic representation of the relevant diagnostics in relation to the event is depicted in Figure 37.

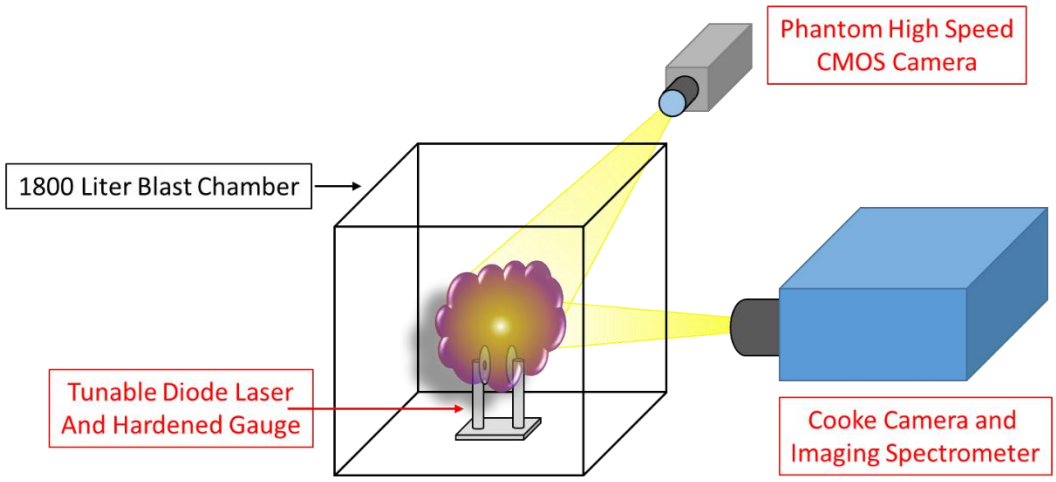

Figure 37: Qualitative depiction of the optical diagnostics fielded in the large scale explosive initiation of aluminum iodine pentoxide thermite.

The first test article presented in this document was a Primasheet 1000® annulus surrounding a core of stoichiometric Al/I_2O_5 thermite. A group of images and illustrations showing the assembly and configuration of this test article are shown in Figure 38. The article was created by stacking cutout discs and annuli of plastic explosive to create an internal pocket that can hold the thermitic material. The functional reason to test this configuration was the observation in small scale that the thermite reaction is not implicitly completed in a dispersing event. As previously mentioned, it was hypothesized that the aluminum was able to react with the ambient oxygen faster than the iodine pentoxide. This design of this article was intended to force the thermitic reaction by confining the fuel and oxidizer in close proximity to each other for an extended period of time.

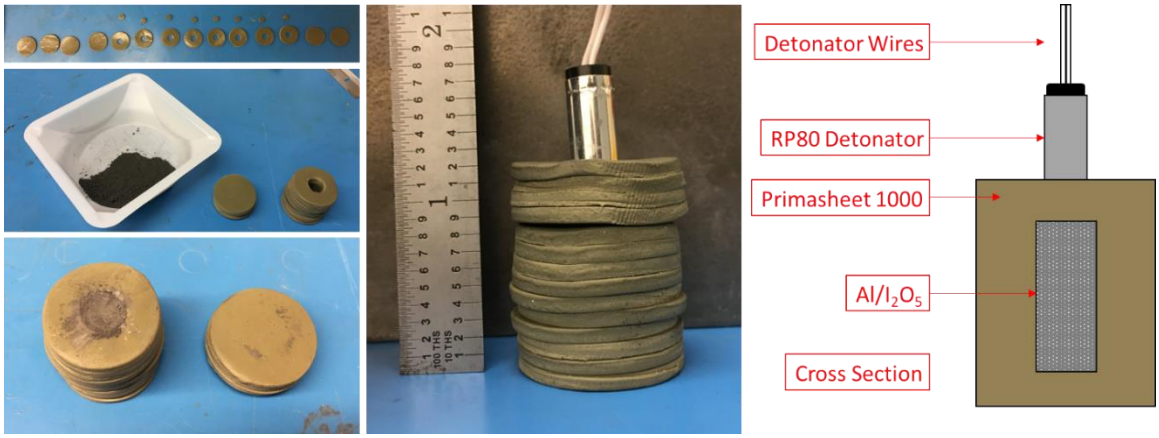

Figure 38: Depiction of the Primasheet® charge used to explosively initiate the Al/I_2O_5 thermite in a configuration that prolongs the exposure of fuel and oxidizer to one another.

The framing camera images and spectra are valuable additions to the tunable laser absorption gauge data because they characterize a vastly different portion of the event. While the laser gauge is designed to probe the cooler, late time post-detonation fireball in absorption, the framing camera spectra represent the extremely high temperature "break out" of the event characterized by emission. In short, the extreme temperatures in the first microseconds of the event may elucidate chemical species not present or not observable in the later portions of the explosion. Analyzing these spectra could potentially provide information on short lived species with rapid consumption such as iodine monoxide (IO) or iodine dioxide (OIO) which have been observed in the portion of the electromagnetic spectrum [97, 98]. The framing camera data collected for this test article are shown in Figure 39. Images were taken with 60 nanosecond exposures, while spectra were collected with 200 ns. The framing camera images were horizontally cropped for this document to better emphasize the details of the article breakout.

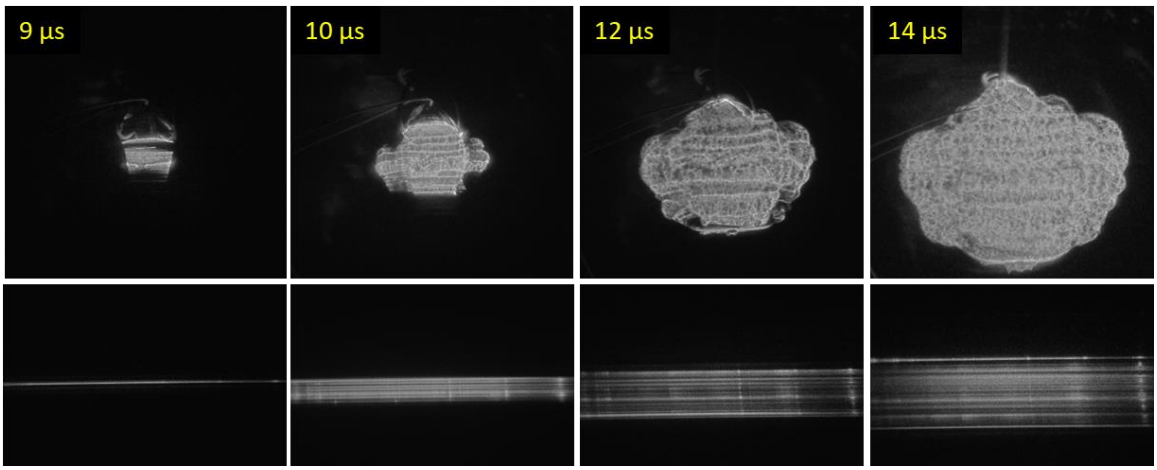

Figure 39: Cooke framing camera images and corresponding spectra collected at break-out times of the Primasheet® annulus test article.

Processing the imaging spectra followed well established techniques. Forgoing the vertical spatial resolution to achieve higher signal to noise ratios, rows of the focal plane array (FPA) were vertically binned across the selected portions of the chip. It can be seen in the spectra shown in Figure 39 that there is significant curvature of the spectra from row to row due to the aberration of the collection lens. This was compensated for by implementing a shift-and-add algorithm. Briefly, a mercury calibration spectrum is taken at a longer exposure to provide the necessary emission lines across a majority of the rows on the FPA. From this, each row is separately calibrated independent of the neighboring rows. Using a cubic spline interpolation routine, each row can be aligned with respect to wavelength and therefore vertically binned without artificially appodizing the data.

Interpreting the imaging spectra from the framing cameras is challenging given the coarse resolution and complexity of the event. Assigning specific material emission lines would be inappropriate with the precision of these data. However, to investigate possible iodine contributions to the feature-rich data sets, the experimental spectra were compared to reference spectra from other events using the same instrument to rule out features from detonators (Cu, Zn, Al, AlO) as well as impurities of high explosives and binders (e.g. Na, Ca, Fe). The 10µs delayed spectrum from the article shown in Figure 38 is analyzed in Figure 40. The entire spectrum is shown in the top of the figure, although only a portion of it was binned in the analysis.

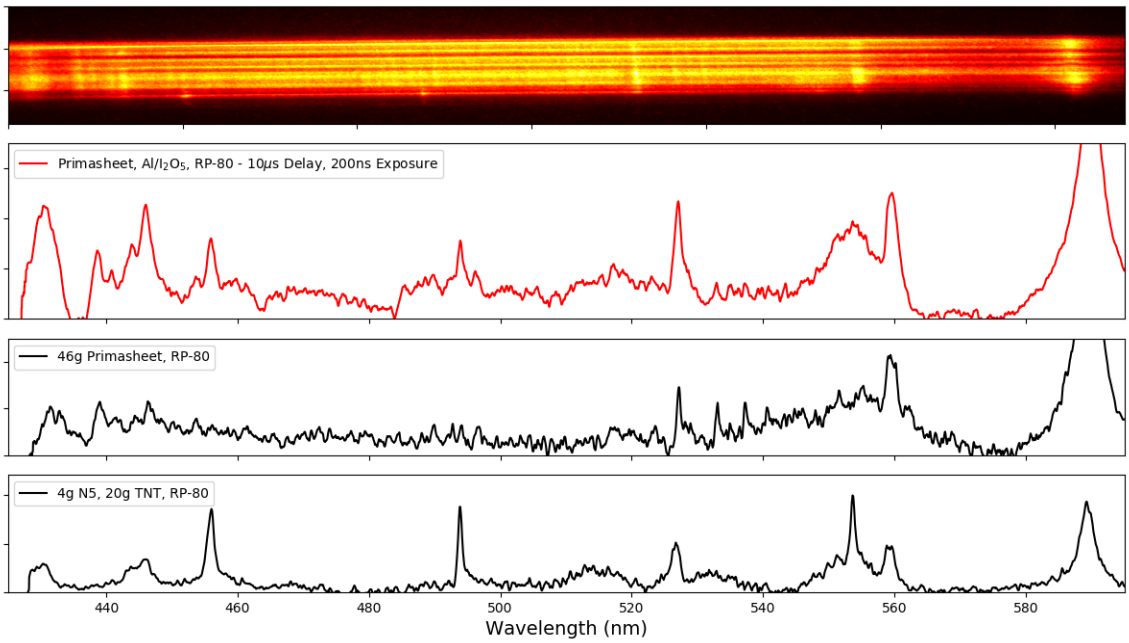

Figure 40: 10μs delayed imaging spectrum from the detonation of Primasheet 1000 surrounding a core of stoichiometric, Aluminum Iodine pentoxide thermite (2nd row, red). A spectrum from the detonation of purely Primasheet initiated with an RP-80 detonator (3rd row, black). A spectrum from the detonation of 20g TNT boosted with 4g PBXN-5 and initiated with an RP-80 (4th row, black).

It is clear that even though there is significant spectral information in the test article emission signature, almost all features can be attributed to the Primasheet and detonator contributions. The notable feature on the right present in all spectra is the unresolved Sodium D-line doublet (588.995, 589.59 nm) [94]. This feature is observed in almost every explosive fireball.

In addition to observing no oxides of iodine in the detonation spectra, no atomic iodine was recorded in the laser probe fireball data. The absence of atomic iodine in the fireball where the gauge was mounted is a key result. However it also shows that the configuration tested potentially stagnates the iodine gas in a small pocket of the chamber as opposed to dispersing it throughout. In this shot, the gauge was mounted slightly off center from the chamber for this test, and so for future tests it was moved directly (30 cm) below the article to witness earlier times of the fireball as it is expected that atomic iodine is extremely transient with expansive cooling. For this reason, in addition to changing the probe location, the article configuration was also changed for future tests.

In comparison to the initial configuration driving the aluminum and iodine pentoxide together, later test articles were designed to be dispersing charges that drive the materials outward into the chamber. Test articles were 2 grams of Al/I_2O_5 loosely placed around a central puck of 10g PBXN-5. An example of this dispersing charge is shown in Figure 41. Teledyne-RISI RP-80s were used to initiate.

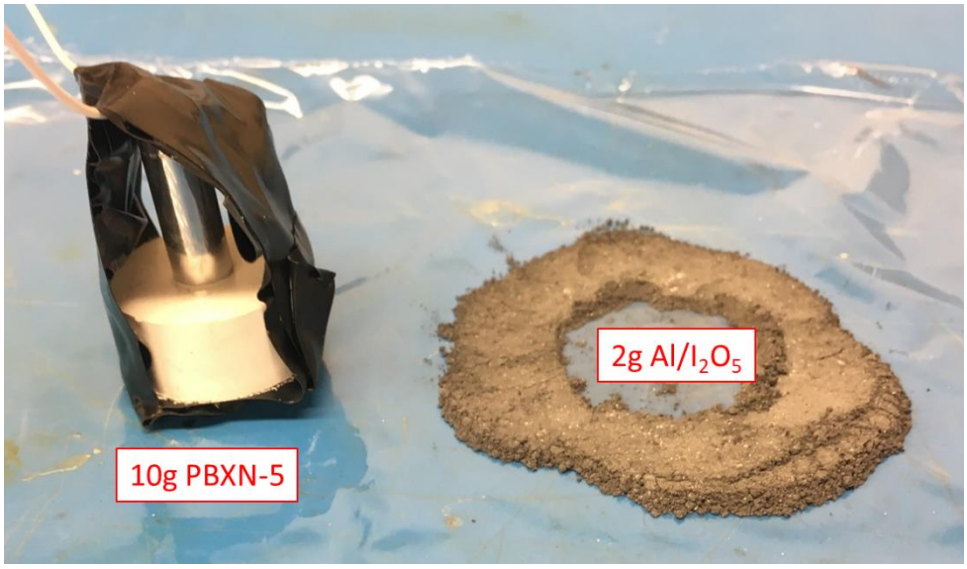

Figure 41: Disassembled explosive dispersing charge used in scaled up iodine testing. Aluminum Iodine Pentoxide was mechanically mixed and then loosely arranged around the 10g explosive puck. Plastic film was used to loosely hold the thermite against the HE. Charges were hung from the top, nominally in the center of the 1800-liter blast chamber.

Initial tests of these dispersing configurations yielded extremely complex data on the atomic iodine gauge given the extraordinary optical depth known to occur in aluminized explosive fireballs. Despite these conditions, transient atomic iodine was detected in the explosively dispersed, thermitic cloud. In order to analogize the small scale experiments, the probe was placed directly under the charge for comparative tests of explosively dispersed and initiated nano- and micro- fuel thermites. The images, spectra, and analysis of framing camera data for the explosively dispersed mico-aluminum iodine pentoxide are presented in Figure 42 and Figure 43. The data for the atomic iodine TDL system is presented at the end of this section in order to compare performance of the two thermites.

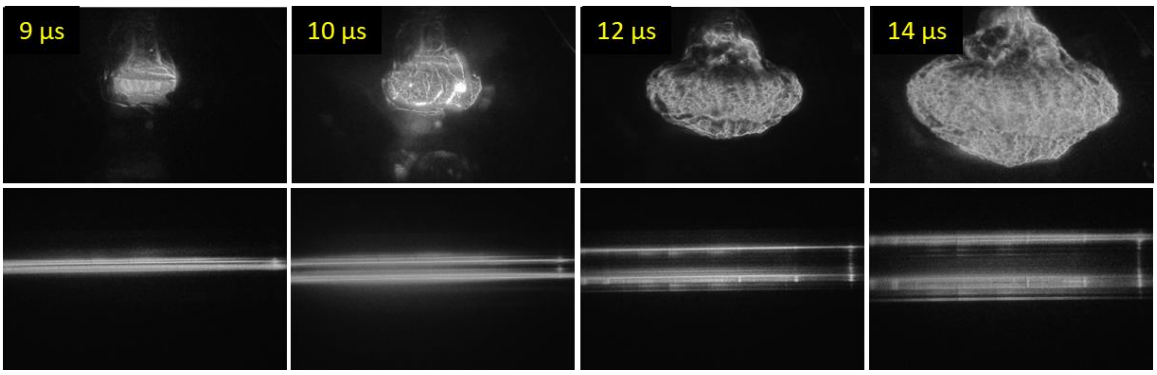

Figure 42: Cooke framing camera images and spectra from the detonation of 10g of PBXN-5 surrounded by 2g of stoichiometric aluminum iodine pentoxide thermite (German Flake aluminum) initiated with an RP-80 detonator.

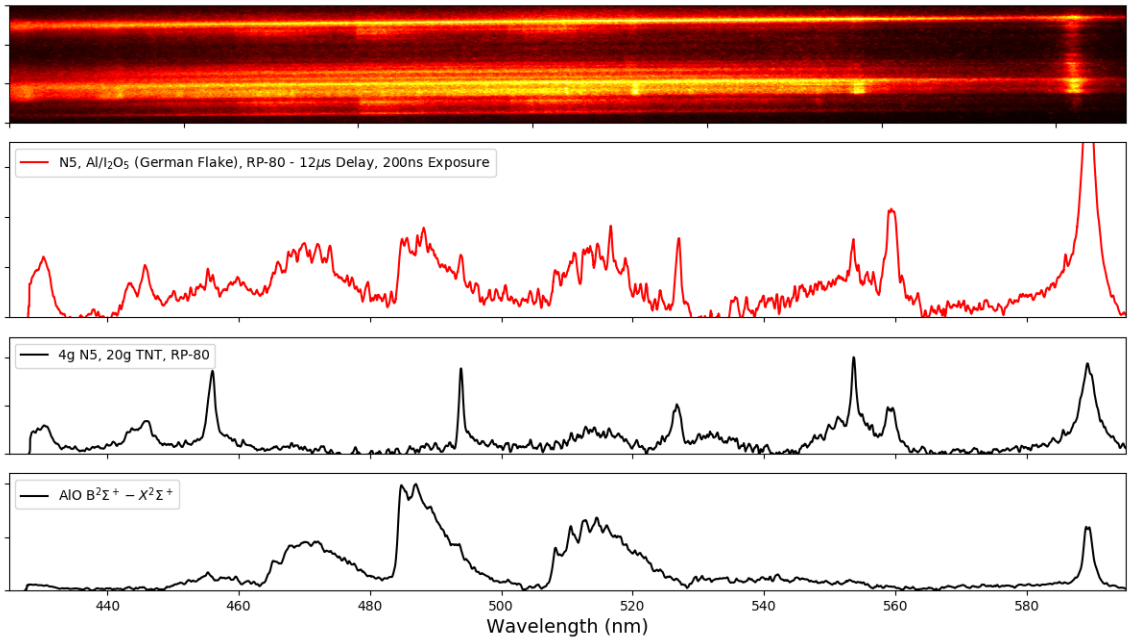

Figure 43: 12µs delayed imaging spectrum from the detonation of 10g PBXN-5 surrounded by stoichiometric, Aluminum Iodine pentoxide thermite mixed from German flake Al (2nd row, red). A spectrum from the detonation of 20g TNT boosted with 4g N5 and initiated with an RP-80 detonator (3rd row, black). A spectrum from collected with the Cooke framing cameras depicting the well-known aluminum monoxide B-X electronic structure. (4th row, black).

The comparison of spectral data show that again, all significant emission features in the test can be attributed to the explosive, the detonator, and the well-documented aluminum monoxide $B^2\Sigma^+ - X^2\Sigma^+$ blue-green spectrum [99, 100]. The AlO structure of the test spectrum does show a severe amount of distortion due to optical thickness evident in the relatively equal intensities of the Δv = -1, 0, and 1 branches.

The framing camera data from the nano-aluminum iodine pentoxide test is presented in Figure 44. The framing camera delay times were extended in order to investigate slightly later portions of the event. This is clearly evident in the expansion of the 22 μs image expanding beyond the field of view of the lens.

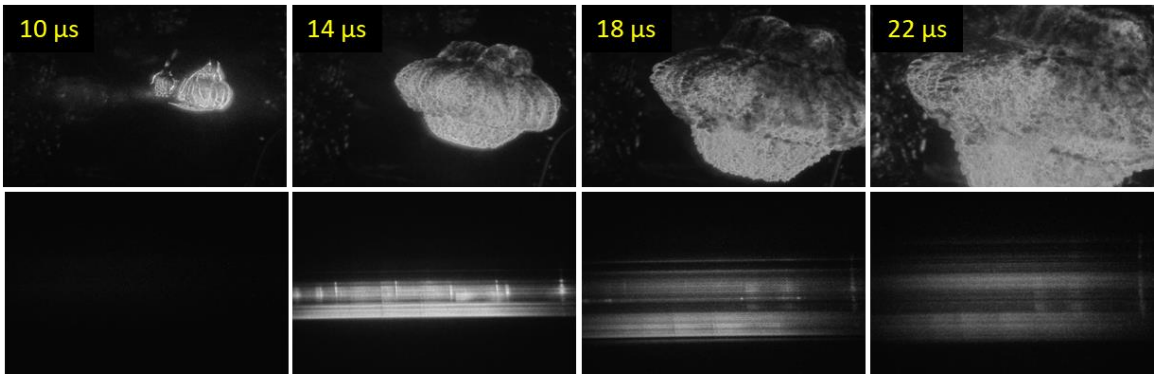

Figure 44: Cooke framing camera images and spectra from the detonation of 10g of PBXN-5 surrounded by 2g of stoichiometric aluminum iodine pentoxide thermite (40-50nm aluminum) initiated with an RP-80 detonator.

It can be seen that the 14-microsecond delayed spectrum has a significant amount of information and therefore is reduced in Figure 45. It is also noted that the spectral image shows significantly different spatial information. The top of the spectrum has the features believed to be associated with the detonator and PBXN-5, while the bottom portion of the image is almost entirely thermal continuum until the 18μs spectrum which shows the saturation subsiding to reveal the predictable presence of aluminum monoxide.

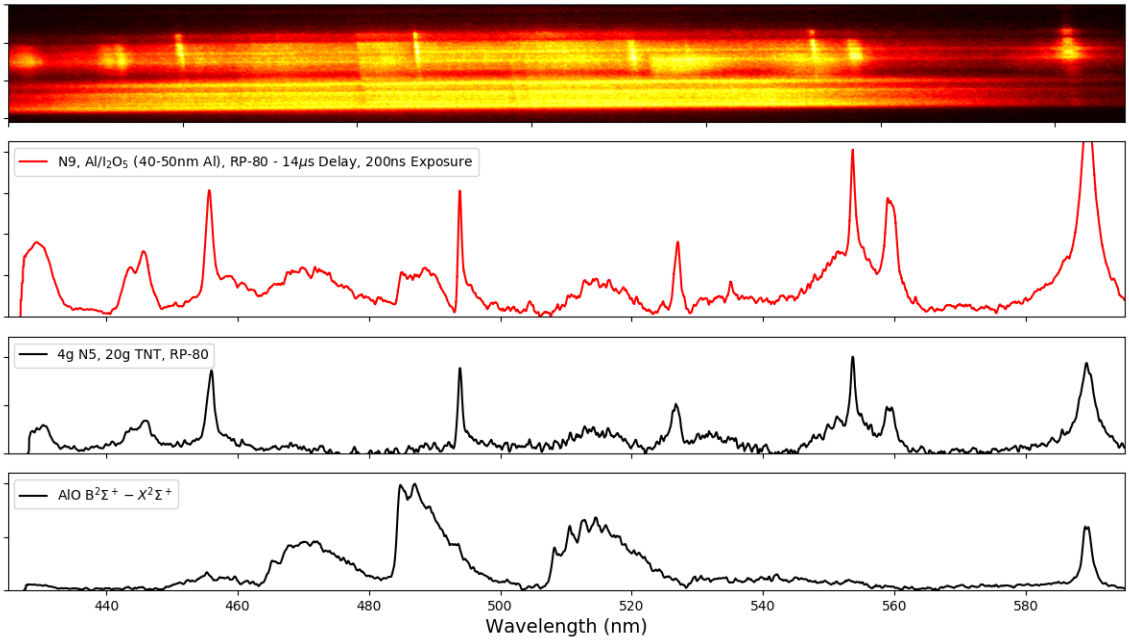

Figure 45: 14μs delayed imaging spectrum from the detonation of 10g PBXN-5 surrounded by stoichiometric, Aluminum Iodine pentoxide thermite mixed from 40-50nm Al (2nd row, red). A spectrum from the detonation of 20g TNT boosted with 4g N5 and initiated with an RP-80 detonator (3rd row, black). A spectrum from collected with the Cooke framing cameras depicting the well-known aluminum monoxide B-X electronic structure. (4th row, black).

Much like in the case of the micro-aluminum thermite, the features in the framing camera spectra of the nano-thermite dispersion can predominantly be attributed to the high explosive, and aluminum monoxide. There is however one additional feature defined above the "noise" near 535 nm by this calibration that is not evident in the reference PBXN-5 spectrum.

As previously mentioned, the tunable diode laser was able to detect the brief presence of atomic iodine in the post-detonation fireball. As previously mentioned, the optical challenges of probing the heavily aluminized fireball with lasers rendered data quality significantly lower than in the small-scale testing. The measured atomic iodine number density and laser throughput during the explosive tests are shown in Figure 46. Data were collected at a rate of 20 kHz, and presented both raw and with a 500 μs moving boxcar filter. Due to the total signal attenuation during the first 1 ms of the fireball, no spectra from that time were recorded and the filter represents the interpolation of pre-trigger and measured data after 1 ms.

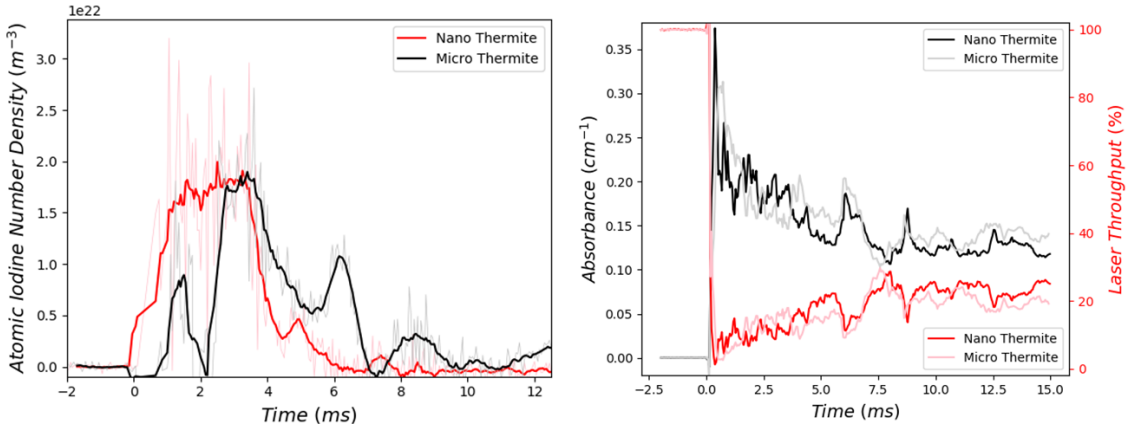

Figure 46: Atomic iodine number density from explosively driven nano- and micro- aluminum iodine pentoxide thermite fireballs (left). The combined resonant, and non-resonant laser attenuation history from the same tests shown as arbitrary laser signal throughput as well as path length corrected absorbance.

The number density of atomic iodine is shown to persist for no more than 10 milliseconds in either case. The German Flake aluminum (micro-) based thermite does portray a slower decay, although trends in these limited sets would be hard to interpret given the significant role of turbulence and temperature on measured atomic iodine.

The laser throughput and calculated absorbance quantify the extreme measurement challenges of this environment. Data were collected with roughly 10-15 % of the laser throughput. Although there is room for improvement, these tests concretely demonstrate that the developed probe and atomic iodine diagnostic can be quantitatively employed in practical, halogenated explosive tests where significant turbulence and signal attenuation are present. A storyboard of the reference images taken with the Phantom 5 high-speed camera showing the probe being engulfed in the reacting product cloud of the nano-thermite is shown in Figure 47.

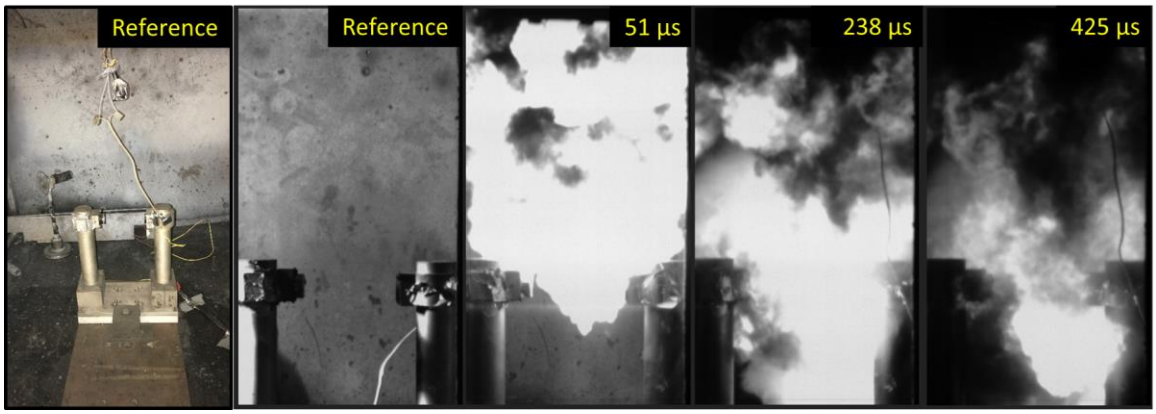

Figure 47: Phantom 5 reference images of the first 0.5 ms of the post-detonation fireball generated from 10g PBXN-5 with 2 g aluminum iodine pentoxide (40-50 nm Al) thermite surrounding the explosive puck. Charge was initiated with an RP-80 detonator. Images depict the hardened gauge fielding the atomic iodine monitoring tunable diode laser being engulfed in the aluminized product cloud.

3.8. Accuracy and Uncertainty in Atomic Iodine Measurement:

The assumptions made due to the lack of material temperature have already been discussed with respect to their effect on number density. In addition to those small mathematical sources of error, there is an unavoidable systematic error introduced when the resonant absorption depth is significant. This error is due to the combination of hardware limitation and background fitting of the spectra. Identical to the processing method described for the water vapor spectra, the background of each laser sweep is fit using a spline interpolation of regressions drawn from data outside the strong absorption features.

The challenge with the laser sweep of this system is that the while the F'=3 triplet is fully covered by an allowable current sweep, the F'=2 triplet extends beyond the maximum tunable range. At low pressures and number densities, the transmittance between the triplets is very close to 1.0 implying that it is reasonable to take this region of spectrum as a usable background. However at higher number densities, this assumption breaks down, and using the top of the laser sweep as a portion of the background artificially reduces the number density by cutting into the integrated absorbance. This is illustrated in Figure 48 with simulated data as it may appear if the laser was swept over the entire structure of the absorption spectrum. The actual portion of the spectrum swept with the current instrument is shown in solid lines, and the unmeasured F'=2 triplet is shown in dashed

lines if the current sweep was continued. The figure is depicting that even though the triplets are substantially separated, the spectral gap between the two actually begins to be consumed when sufficient number density and/or pressure broadening is present. The background can deviate 2% even at modest mole fractions. With broadband attenuation arising from flow conditions changing on the order or in excess of the laser modulation frequency, it's impractical to construct the background from only one side of the absorption band.

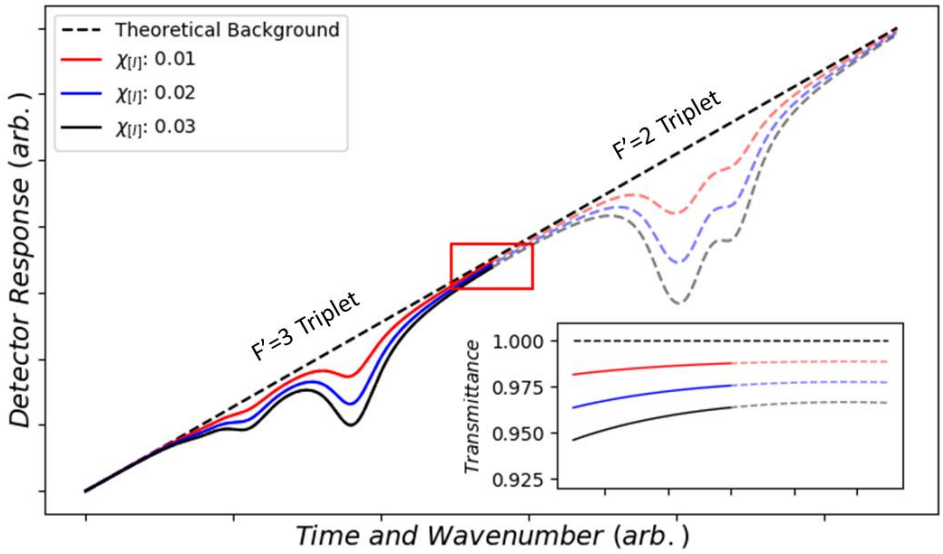

Figure 48: Theoretical model of the laser sweep as it would be measured scanning over the entire hyperfine structure of the 1315nm atomic iodine transition. Model was done at 1.5 atm., 1000 Kelvin, and a 10 cm path length.

This error is then a function of actual number density itself. That is, the absolute error in number density increases with the true amount of iodine present in the flow. Although second order errors are also introduced based on the distorted slope at the end of the laser sweep, those are extremely complicated to accurately account for. A simplified error estimate is calculated through the area of integrated absorbance artificially removed by assuming that the spectrum returns to the background at each end of the sweep. This effect of the background fitting, and how it translates into calculation error is illustrated in Figure 49.

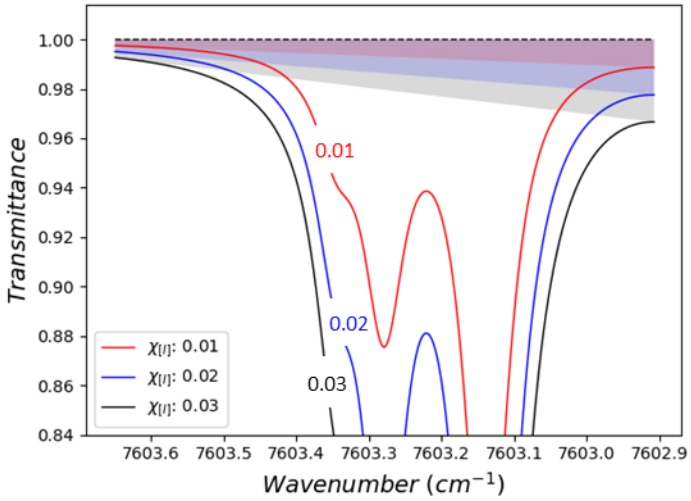

Figure 49: Illustration of the systematic error introduced in the numerical integration of band structure for atomic iodine number density assuming that the wings of the laser sweep are acceptable background references.

The error was measured by modeling the spectrum at a range of concentrations across the spectral domain from an actual sweep of the laser used in this work at a temperature of 1000 Kelvin and path length of 10 cm. The non-zero values of the absorbance spectrum at each end of the domain were recorded and used to calculate the integrated area if the background were drawn linearly between those points as opposed to the true zero. This artificially removed integrated absorbance was converted to number density using the process detailed previously in this document. Results from this analysis are shown in Figure 50.

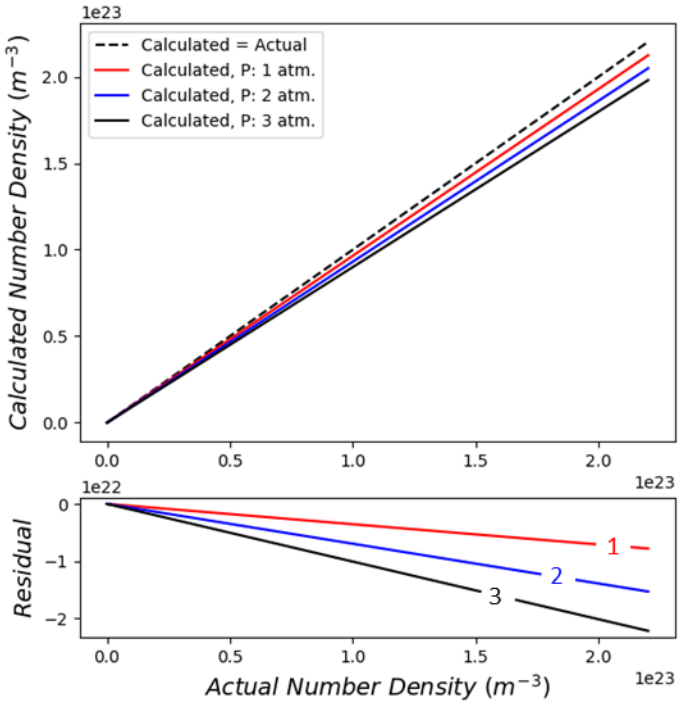

Figure 50: The calculated error in number density arising from background fitting error. The errors were calculated at 1000 Kelvin with a 10 cm absorbing path length. The error has a pressure dependence due to the broadening of features across the background. Consequently, the minimum error belongs to the 1 atm curve (red) and the most severe to the 3 atm curve (solid-black).

As previously mentioned, the absolute number density error is dependent on concentration itself. This is clearly shown in the plotted values. However, looking at the relative error in concentration (Calculated / Actual) reveals a less obvious phenomenon in that the percent error is nearly constant across the modeled range of data. The 1 atm. analysis yielded an error of -3.55 ± 0.01% across the range of number densities in Figure 50. The 2 atm. analysis yielded an error of -6.96 ± 0.01%. The 3 atm. analysis yielded an error of -10.08 ± 0.01%.

The detection limit of atomic iodine is estimated based on our assumed ability to discriminate a 1% absorption depth above the noise floor of the signal. In an optically thin gas cell this value could be significantly lower, but in the context of a turbulent, optically thick fireball, it is estimated that a number density of $7x10^{20}$ m^{-3} with a 14 cm absorbing path length.

CHAPTER 4: CONCLUSIONS AND FUTURE RECOMENDATIONS

4.1. Conclusions from Temperature Measurement Diagnostics:

With the goal to combine predictive modeling and experimental validation, the ability to simultaneously measure multiphase temperature, pressure, and speciation inside of an explosive fireball is invaluable. This work provides an apparatus and procedure for fielding a wide variety of proven combustion diagnostics in practical explosive tests. The laser beam is brought into the probe using an off-the-shelf fiber-optic patch cable, and therefore it can be switched seamlessly to monitoring a different temperature range or chemical species simply by connecting a different diode laser outside the chamber. The pyrometer can readily be configured and optimized to monitor cooler soot temperatures simultaneously using the additional fibers already installed.

The data validate the ability to model early-time temperature using gas dynamic relations, as well as predicts long term equilibrium behavior with thermochemical codes [16, 17]. The most useful application of this diagnostic is to measure the transient thermodynamics between the shock and equilibrium timescales that are not easily characterized with established models. Figure 51 shows extremely high-fidelity measurements on very short time scales during the intermediate phase of the explosion.

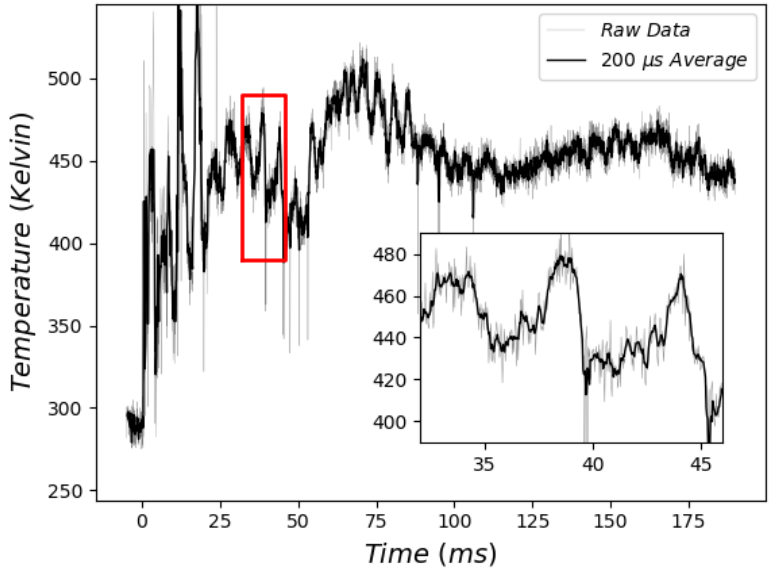

Figure 51: A 200 millisecond temperature profile from a 28.48 gram PBXN-5 explosive test, with an inset figure showing the diagnostic ability to characterize sub-millisecond temperature fluctuations with an approximate ±5 Kelvin uncertainty during some portions of the explosion.

The generalized nature of this diagnostic opens the door for application of a huge range of tunable laser sources to be applied.

4.2. Recommendations for Temperature Measurement Diagnostics:

The temperature and chemistry of complex, multiphase explosively-driven flows can be probed in practical near field testing with derivatives of this work. This section provides recommendations for improvements to the current diagnostic, as well as recommendations for future extensions of it.

- **Recommendation 1:** The lollipop blades can be reduced in size or completely removed from the design. A two or three inch diameter blade might provide sufficient flow control to retain blast temperature capabilities, but eliminate the "sail-type" behavior of the larger blades that resulted in flexing of the probe's arms.
- **Recommendation 2:** The end caps to the probe arms could be machined as wedges. This will help in cases where the probe is directly pointed at or

positioned below the charge. It will also help deflect fragments that would otherwise impact a normal surface and deliver a jarring vibration to the optics.

- **Recommendation 3:** The temperature sensitivity range of the spectral features in this work is a limitation. The application of different TDLs to capture higher temperatures is critical.
- **Recommendation 4:** Reconfigure the existing pyrometer to have better temperature measurements. Potentially switch the 900 nm filter to 750nm or 800nm.
- **Recommendation 5:** As it sits, the probe has two viable optical fibers that went unused in the present work. It seems pertinent to measure colder soot temperatures. Applying the spare fibers to a mid-infrared, two-color pyrometer to capture lower temperatures at later times would be an excellent extension of this work.
- **Recommendation 6:** For a substantial continuation of this work, another probe needs to be fabricated to accommodate two lasers. The key to the success of the current design was accommodating all of the optoelectronics into Delrin mounts and lens tubes. The current probe used 1" lens tubes and could only accommodate a single emitter and detector. If a slightly larger probe was fabricated, a 2" lens tube could be accommodated and within that, each arm could support an emitter and a detector. This will enable the simultaneous fielding of two swept wavelength lasers. The probe could then monitor the same transition in multiple optical depths. It could monitor different transitions for high accuracy in different temperature ranges. It could monitor two different species where one is explicitly an explosive product (i.e. carbon monoxide, nitric oxide, etc.) so that the path averaged water vapor (product and ambient) can be compared explicitly to that of the explosive products. This represents characterization of thermal diffusion and gas mixing in the chamber.

4.3. Conclusions from Atomic Iodine Measurement Diagnostics:

A variety of energetic material tests were conducted at different scales, and with varied article configurations. At the small scale, spark-ignited stoichiometric, aluminum iodine pentoxide thermite mixtures were initiated in a 2.18-liter blast camber. At the larger scale, 10 grams of PBXN-5 were surrounded by 2 grams of Al/I_2O_5 to explosively disperse and initiate an iodized dust cloud in the 1800-liter blast chamber. The purpose of these tests was to design and demonstrate an optical diagnostic capable of monitoring halogen (atomic iodine) presence in practical explosive flows.

- **Conclusion 1:** Tunable diode laser absorption spectroscopy can be used to rapidly sweep over the 1315nm atomic iodine transition to provide time-resolved measurement of atomic iodine concentration.
- **Conclusion 2:** Using the 1315nm atomic iodine transition, concentration can be calculated with minimal error from spectral measurements without explicit knowledge of material temperature (below a certain temperature). This is possible due to the fact that the partition function is only a weak function of temperature due to material energy level spacing, and because the $^2P_{1/2}$ to $^2P_{3/2}$ transition (1315nm) is absorbing from the ground state where $E_{ground} = 0\ cm^{-1}$. This implies that the Boltzmann fraction is strictly proportional to the constant hyperfine degeneracy.
- **Conclusion 3:** The tunable diode laser system can readily be adapted to a hardened gauge and used in true post-detonation fireballs. Successfully demonstrating this feat in a heterogeneous dust explosion with micron sized-particulate confirms that the developed diagnostic is fully capable of high-speed, quantitative measurements in the most complicated, practical detonation fireballs.
- **Conclusion 4:** Although not an exhaustive test matrix, the large scale testing where the laser gauge was engulfed in the flow suggests that the atomic iodine presence is very transient at this scale (< 10ms) likely due to rapid cooling. More importantly though, changing the location of the probe relative to the charge suggested that the chamber gas stratification and direction of material ejection

from the charge will always strongly influence the spatial location of iodine in the fireball.

4.4. Recommendations for Halogen Measurement Diagnostics:

This work successfully demonstrated a diagnostic for monitoring atomic iodine. This section will present a select few improvements to the existing diagnostic, but also discuss opportunities for branching the demonstrated technology to other compounds of interest to the C-WMD community.

- **Recommendation 1:** Use a tunable wavelength laser that is capable of sweeping over the entire hyperfine structure of the 1315nm transition. Given the systematic error introduced when fitting backgrounds, it makes sense to use hardware that can provide more non-resonant spectrum that will help more accurately characterize the background in each sweep. This will enable more accurate measurement of integrated absorbance and provide improved robustness against error due to pressure broadening.
- **Recommendation 2:** The conventional approach to producing iodine in explosives by using solid state reactive materials results in extraordinary optical depth. This was seen in the thermite explosions presented here. Developing a two-detector system where each detector is optimized for different optical depths will enable measurement when the transmitted laser intensity is much lower than it was in the present work.
- **Recommendation 3:** The observation of the spatial dependence of atomic iodine within the fireball suggests that monitoring various locations in the chamber is useful. This can be accomplished with multiple detectors and lasers, or conversely a single laser with higher power and a system of beam splitters. It is estimated that 10 mW per location is sufficient power.
- **Recommendation 4:** The concept of target interaction is another logical application of this diagnostic. The question being posed is, does contact between the explosive cloud and surrounding ambient temperature surfaces rapidly condense iodine out of the flow or cool it and convert it to molecular iodine? It is

recommended that a controlled explosive test be conducted by measuring atomic iodine concentration at various standoff distances from a plate of steel or the chamber wall. If the experiment is conducted with a dedicated target plate, the temperature of that could be varied with back mounted resistive heating bands.

- **Recommendation 5:** Although iodine is the focus of the present work, other halogen compounds may be of interest that could readily be monitored with analogous techniques. For example, one might consider the monitoring of hydrogen fluoride (HF) in biocidal explosions [101]. TDLAS measurement of HF is not novel, and with the newly developed TDL hardened gauge, those can be applied to explosive application with relative ease [102]. A distributed feedback (DFB) TDL with a narrow sweep could leverage the high temperature band head that forms in the R-branch of the overtone to make high-speed temperature and concentration measurements with relative ease. Conversely, an external cavity tunable diode laser (ECTDL) with a larger seep range could potentially cover the entire R or P branch of the overtone providing a thermometer with exceptional range. If the P branch was swept over, the known water vapor interferences in those wavelengths could also provide a secondary species measurement in the same spectrum. With the simplicity of single pixel mid infrared detectors, the fundamental band of hydrogen fluoride is also accessible for lower detection limits. This concept may also enable measurement of the fundamental band of hydrogen iodide (HI) as it is much stronger than the overtone, but further into the mid infrared. The detection limit of HI could be further lowered by applying wavelength modulation spectroscopy (WMS) [103].

REFERENCES

[1] J. E. Greenspon, "Study of Isodamage Prediction for Enhanced Payloads," Defense Special Weapos Agency, Alexandria, 1998.

[2] D. A. Henderson, "Smallpox as a Biological Weapon," *JAMA, Journal of the American Medical Association,* vol. 281, no. 22, pp. 2127-2137, 1999.

[3] T. V. Inglesby, "Anthrax as a Biological Weapon," *JAMA, Journal of the American Medical Association,* vol. 281, no. 18, pp. 1735-1745, 1999.

[4] Defense Threat Reduction Agency, "Government Call, Fundamental Research to Counter Weapons of Mass Destruction (C-WMD)," 2016.

[5] J. Henderson, "Experiments and Modeling for Biocidal Effects of Explosives," *Propellants, Explosives, and Pyrotechnics,* vol. 40, no. 5, pp. 712-719, 2015.

[6] "Mechanism of killing of spores of Bacillus anthracis in ahigh-temperature gas environment, and analysis of DNAdamage generated by various decon tamination treatmentsof spores of Bacillus anthracis, Bacillus subtilis and Bacillus thuringiensis," *Journal of Applied Microbiology,* vol. 116, pp. 805-814, 2013.

[7] B. R. Clark and M. L. Pantoya, "The Aluminum and Iodine Pentoxide Reaction for the Destruction of Spore Forming Bacteria," *Physical Chemistry and Chemical Physics,* vol. 12, pp. 12653-12657, 2010.

[8] C. Farley and M. Pantoya, "Reaction Kinetics of Nanometric Aluminum and Iodine Pentoxide," *Journal of Thermal and Analytical Chemistry,* vol. 102, pp. 609-613, 2010.

[9] G. Zhao, D. Kumar, C. He, J. P. Hooper, G. H. Imler, D. A. Parrish and J. M. Shreeve, "New Generation Agent Defeat Weapons: Energetic N,N'-Ethylene-Bridged Polyiodoazoles," *Chemistry - A European Journal,* vol. 23, no. 66, pp. 16753-16757, 2017.

[10] S. Wang, M. Schoenitz, S. A. Grinshupun, M. Yermakov and E. L. Dreizin, "Biocidal Effectiveness of Combustion Products of Iodine-Bearing Reactive Materials Against Aerosolized Bacterial Spores," *Journal of Aerosol Science,* vol.

116, pp. 106-115, 2018.

[11] B. J. McBride, M. J. Zehe and S. Gordon, "NASA Glenn Coefficients for Calculating Thermodynamic Properties of Individual Species," NASA Center for Aerospace Information, Hanover, 2002.

[12] M. Chase, "NIST-JANNAF Thermochemical Tables, Fourth Edition," *Journal of Physical Chemistry Reference Data,* 1998.

[13] M. Chase, "NIST-JANNAF Thermochemical Tables for the Iodine Oxides," *Journal of Physical and Chemical Reference Data,* vol. 25, no. 5, pp. 1297-1340, 1996.

[14] K. C. Gross, "Phenomenological Model for Infrared Emissions from High-Explosive Detonation Fireballs," Wright-Patterson Air Force Base, 2007.

[15] S. Goroshin, D. L. Frost, J. Levine, A. Yoshinaka and F. Zhang, "Optical Pyrometry of Fireballs and Metalized Explosives," *Propellants, Explosives, and Pyrotechnics,* vol. 31, no. 3, pp. 169-181, 2006.

[16] J. M. Peuker, P. Lynch, H. Krier and N. G. Glumac, "Optical Depth Measurements of Fireballs from Aluminized High Explosives," *Optics and Lasers in Engineering,* vol. 47, no. 9, pp. 1009-1015, September 2009.

[17] L. S. Lebel, P. Brousseau, L. Erhardt and W. S. Andrews, "Measurements of the Temperature Inside an Explosive Fireball," *Journal of Applied Mechanics,* vol. 80, May 2013.

[18] W. K. L. e. al., "Time-Dependent Temperature Measurements in Post-Detonation Combustion: Current State-of-the-Art Methods and Emerging Technologies," Defense Threat Reduction Agency, Fort Belvoir, 2016.

[19] P. R. N. Childs, J. R. Greenwood and C. A. Long, "Review of Temperature Measurement," *Review of Scientific Instruments,* vol. 71, no. 8, pp. 2959-2978, 2000.

[20] "Thermocouple: Different Types, What It Is, and How to Replace One," Omega, [Online]. Available: https://www.omega.com/prodinfo/thermocouples.html. [Accessed 15 September 2018].

[21] T. R. Time, Omega, [Online]. Available: https://www.omega.com/techref/ThermocoupleResponseTime.html. [Accessed 15 September 2018].

[22] D. L. Frost, S. Goroshin, M. Cairns, R. Ripley and F. Zhang, "Temperature Measurements in a Multiphase Fireball," in *22nd International Colloquium on the Dynamics of Explosions and Reactive Systems*, Minsk, 2009.

[23] A. D. Eisner and D. E. Rosner, "Experimental Studies of Soot Particle Thermophoresis in Nonisothermal Combustion Gases Using Thermocouple Response Techniques," *Combustion and Flame,* vol. 61, pp. 153-166, 1985.

[24] V. R. Stull and G. N. Plass, "Emissivity of Dispersed Carbon Particles," *Journal of the Optical Society of America,* vol. 50, no. 2, pp. 121-129, 1960.

[25] P. Lynch, H. Krier and N. Glumac, "Emissivity of Aluminum-Oxide Particle Clouds: Application to Pyrometry of Explosive Fireballs," *Journal of Thermophysics and Heat Transfer,* vol. 24, no. 2, pp. 301-308, 2010.

[26] T. Bazyn, P. Lynch, H. Krier and N. Glumac, "Combustion Measurements of Fuel-Rich Aluminum andMolybdenum Oxide Nano-Composite Mixtures," *Propellants, Explosives, and Pyrotechnics,* vol. 35, pp. 93-99, 20010.

[27] K. C. Gross, J. Wayman and G. P. Perramc, "Phenomenological Fireball Model for Remote Identification of High-Explosives," *Proceedings of SPIE,* vol. 6566, 2007.

[28] W. K. Lewis, C. G. Rumchik and M. J. Smith, "Emission Spectroscopy of the Interior of Optically Dense Post-Detonation Fireballs," *Journal of Applied Physics,* vol. 113, 2013.

[29] N. M. Laurendeau, Statistical Thermodynamics: Fundamentals and Applications, New York, New York: Cambridge University Press, 2005.

[30] A. Bohlin and C. J. Kliewer, "Direct Coherent Raman Temperature Imaging and Wideband Chemical Detection in a Hydrocarbon Flat Flame," *The Journal of Physical Chemistry Letters,* vol. 6, pp. 643-649, 2015.

[31] S. P. Kearney and D. J. Scoglietti, "Hybrid femtosecond/picosecond rotational coherent anti-Stokes Raman scattering at flame temperatures using a second-

harmonic bandwidth-compressed probe," *Optics Letters,* vol. 38, no. 6, pp. 833-835, 2013.

[32] R. K. Hanson, "Shock Tube Spectroscopy: Advanced Instrumentation with a Tunable Didode Laser," *Applied Optics,* vol. 16, no. 6, pp. 1479-1481, 1977.

[33] X. Zhou, X. Liu, J. B. Jeffries and R. K. Hanson, "Development of a Sensor for Temperature and Water Concentration in Combustion Gases Using a Single Tunable Diode Laser," *Measurement Science and Technology,* pp. 1459-1468, 21 July 2003.

[34] D. W. Mattison, Development and Application of Laser-Based Sensors for Harsh Combustion Environments, Stanford University, 2006.

[35] D. W. Mattison, C. M. Brophy, S. T. Sanders, L. Ma, K. M. Hinckley, J. B. Jeffries and R. K. Hanson, "Pulse Detonation Engine Characterization and Control Using Tunable Diode-Laser Sensors," *Journal of Propulsion and Power,* vol. 19, no. 4, pp. 568-572, July-August 2003.

[36] J. R. Carney, J. M. Lightstone, S. Pieucuch and J. D. Koch, "Water Temperature and Concentration Measurements Within the Expanding Blast Wave of a High Explosive," *Measurement Science and Technology,* vol. 22, 2011.

[37] J. D. Koch, J. R. Carney, J. M. Lightstone and S. R. Piecuch, "Use of a Fast Near-Infrared Spectrometer for Absoption and Emission Measurements within the Expanding Blast Wave of a High Explosive," in *AIP Conference Proceedings,* Chicago, IL, 2012.

[38] S. Evans, "The Arc Spectrum of Iodine," *Proceedings of the Royal Society of London. Series A, Containing Papers of a Mathematical and Physical Character,* vol. 133, no. 822, pp. 417-430, 1931.

[39] L. A. Turner, "Optical Dissociation of Iodine and Enhancement of Predissociation by Collisions," *Physical Review,* vol. 41, pp. 627-634, 1932.

[40] O. Spalek, "Gas and Chemical Lasers and Intense Beam Applications," Defense Technical Information Center, Czech Republic, 2002.

[41] D. S. Stromberg, L. A. Fockler, D. L. Carroll and W. C., "New simulations for

COIL lasers from the University of Illinois," in *Proceedings of SPIE,* St. Petersburg, 2001.

[42] K. Truesdell, C. Helms and G. Hager, "A History of Coil Development in the USA," in *Proceedings of SPIE,* Friedrichshafen, 1994.

[43] D. L. Carroll, W. C. Solomon, L. F. D. King, D. Stromberg, M. Sexauer, A. Milmoe and L. Sentman, "Advanced Mixing Nozzle Concepts for COIL," in *Proceedings of the International Conference on Lasers,* McLean, 2000.

[44] R. G. Derwent and B. A. Thrush, "The Radiative Lifetime of the Metastable Iodine Atom I(5 2P 1/2)," *Chemical Physics Letters,* vol. 9, no. 6, pp. 591-592, June 1971.

[45] R. Engleman, Jr., B. A. Palmer and S. J. Davis, "Transition Probability and Collision Broadening of the 1.3-μm Transition of Atomic Iodine," *Journal of the Optical Society of America,* vol. 73, no. 11, pp. 1585-1589, November 1983.

[46] S. J. Davis, P. A. Mulhall, M. Bachman, W. J. Kessler and P. B. Keating, "Measurements of Pressure-Broadening Coefficients for the F‘ = 3 ← F‘ ‘ = 4 Hyperfine Line of the 2P1/2 ← 2P3/2 Transition in Atomic Iodine," *The Journal of Physical Chemistry A,* vol. 106, no. 36, pp. 8323-8327, May 2002.

[47] G. C. M. II, T. L. Henshaw, T. J. Madden, J. M. Herbelin, B. D. Rafferty and G. D. Hager, "Characterizing Fluorine and Chlorine Atom Flow Rates Using Iodine Atom Spectrometry," *AIAA Journal,* vol. 39, no. 3, pp. 447-454, 2001.

[48] W. Kessler, P. Mulhall, J. Polex and S. J. Davis, "Ultra-sensitive diagnostic for small signal gain in COIL and AGIL lasers," in *Proceedings of SPIE,* San Jose, 2003.

[49] S. J. Davis, M. G. Allen, W. J. Kessler, K. R. McManus and M. F. Miller, "Diode laser-based sensors for chemical oxygen iodine," in *Proceedings of SPIE,* San Jose, 1996.

[50] J. Vanderover and M. A. Oehlschlaeger, "A Mid-Infrared Scanned-Wavelength Laser Absorption Sensor for Carbon Monoxide and Temperature Measurments from 900 to 4000 K," *Applied Physics B,* vol. 99, pp. 353-362, December 2009.

[51] X. Zhou, . J. B. Jeffries, R. K. Hanson, G. Li and E. J. Gutmark, "Wavelength-

Scanned Tunable Diode Laser Temeprature Measurements in a Model Gas Turbine Combustor," *AIAA Journal*, pp. 420-425, February 2007.

[52] S. R. Piecuch, *A Fast NIR Spectrometer for Examining Explosive Events: Emission of PETN Based Explosives and H2O Absorption Method Feasibility*, Milwaukee, Wisconsin: UMI ProQuest, 2009.

[53] I. E. Gordon, L. S. Rothman and C. Hill et al., "The HITRAN2016 Molecular Spectroscopic Database," *J Quant Spectrosc Radiat Transfer*, pp. 1-66, 2017.

[54] C. S. Goldenstein, V. A. Miller, R. M. Spearrin and C. L. Strand, "SpectraPlot.com: Integrated Spectroscopic Modeling of Atomic and Molecular Gases," *Journal of Quantitative Spectroscopy and Radiative Transfer*, vol. 200, pp. 249-257, October 2017.

[55] C. Hill, Learning Scientific Programming with Python; The Voigt profile, Cambridge: Cambridge University Press, 2015.

[56] F. Gao and L. Han, "Implementing the Nelder-Mead simplex algorithm with adaptive parameters," *Computational Optimization and Applications*, vol. 51, no. 1, pp. 259-277, 2012.

[57] E. Jones, E. Oliphant, P. Peterson and e. al., "SciPy: Open Source Scientific Tools for Python," [Online]. Available: http://www.scipy.org/. [Accessed 10 6 2018].

[58] J. e. a. Tennyson, "IUPAC critical evaluation of the rotational–vibrationalspectra of water vapor, Part III: Energy levels and transitionwavenumbers for H216O," *Journal of Quantitative Spectroscopy & Radiative Transfer*, vol. 117, pp. 29-58, 2013.

[59] R. D. J. III, "NIST Computational Chemistry Comparison and Benchmark Database," NIST Standard Reference Database Number 101, 19 April 2018. [Online]. Available: https://cccbdb.nist.gov/exp2x.asp?casno=7732185. [Accessed 2018].

[60] G. Herzberg, Electronic Spectra of Polyatomic Molecules, New York: Litton Educational Publishing Inc., 1966.

[61] P. Atkins and J. de Paula, Physical Chemistry, 7th ed., New York: W.H. Freeman

and Company, 2002.

[62] J. Fischer, R. Gamache, A. Goldman, L. Rothman and A. Perrin, "Total Internal Partition Sums for the Molecular Species in the 2000 Edition of the HITRAN Database," *Journal of Quantitative Spectroscopy and Radiative Transfer,* vol. 82, pp. 401-412, 2003.

[63] G. Herzberg, Infrared and Raman Spectra, New York: Litton Educational Publishing Inc., 1945.

[64] R. K. Hanson, R. M. Spearrin and C. S. Goldenstein, Spectroscopy and Optical Diagnostics for Gases, New York: Springer, 2016.

[65] R. Barber, J. Tennyson, G. Harris and R. Tolchenov, "A High-Accuracy Computed Water Line List," *Monthly Noticies of the Royal Astronomical Society,* vol. 386, pp. 1087-1094, 2006.

[66] C. E. Needham, Blast Waves, Springer, 2018, pp. 183-185.

[67] M. M. Ismail and S. G. Murray, "Study of the Blast Wave Parameters from Small Scale Explosions," *Propellants, Explosives, Pyrotechnics,* vol. 18, pp. 11-17, 1993.

[68] R. D. Zucker and O. Biblarz, Fundamentals of Gas Dynamics, 2nd ed., Hoboken: John Wiley and Sons, 2002.

[69] S. M. Gilbert, *A Model for the Effects of a Condensed Phase Explosion in a Built-Up Area,* Loughborough: Loughborough University Institutional Repository, 1994.

[70] J. W. Bransford and J. B. Gayle, "Fireball diameters and durations from propellant explosions," NASA Marshall Space Flight Center, Huntsville, 1965.

[71] V. D. R.W. and B. D.S., *Explosion Problems in the Chemical Industry,* Washington DC: The American Chemical Society, 1968.

[72] D. Stull, "Fundamentals of Fire and Explosion," *AlChE Monograph Series, No. 10, American Institute of Chemical Engineers,* vol. 73, p. 22, 1977.

[73] R. A.Strehlow and W. E.Baker, "The characterization and evaluation of accidental explosions," *Progress in Energy and Combustion Science,* vol. 2, no. 1, pp. 27-60, 1976.

[74] S. Bastea and L. E. Fried, "Chemical Equilibrium Detonation," *Shock Wave*

Science and Technology Reference Library, vol. 6, September 2011.

[75] S. Bastea, L. E. Fried, W. M. Howard, I. -F. W. Kuo, P. C. Souers and P. A. Vitello, *Cheetah 8.0,* Livermore, CA.: Energetic Materials Center, Lawrence Livermore National Laboratory.

[76] C. Murzyn, A. Sims, H. Krier and N. Glumac, "High Speed Temperature, Pressure, and Water Vapor Concentration Measurement in Explosive Fireballs Using Tunable Diode Laser Absorption Spectroscopy," *Optics and Lasers in Engineering,* vol. 110, pp. 186-192, 2018.

[77] R. Weinheimer, "Properties of Selected High Explosives," *Propellants, Explosives, Pyrotechnics,* 2002.

[78] P. W. Cooper, Explosives Engineering, New York: John Wiley and Sons, Inc., 1996.

[79] E. S. Shanley and G. A. Melhem, "The Oxygen Blance Criterion for Thermal Hazards Assessment," *Process Safety Progress,* vol. 14, no. 1, pp. 29-31, 1995.

[80] L. A. Kranendonk, A. W. Caswell, C. L. Hagen, C. T. Neuroth, D. T. Shouse, J. R. Gord and S. T. Sanders, "Temperature Measurements in a Gas-Turbine-Combustor Sector Rig Using Swept-Wavelength Absorption Spectroscopy," *Journal of Propulsion and Power,* vol. 25, no. 4, pp. 859-863, 2009.

[81] E. Bryner, M. G. Sharma, C. P. Goyne, J. C. McDaniel, M. Snyder, R. H. Krauss, E. F. Martin and G. S. Diskin, "Tunable Diode Laser Absorption Technique Development for Determination of Spatially Resolved Water Concentration and Temperature," in *48th AIAA Aerospace Sciences Meeting Including the New Horizons Forum and Aerospace Exposition*, Orlando, 2919.

[82] M. F. Modest, Radiative Heat Transfer, New York: McGraw-Hill, Inc., 1993.

[83] M. Beckstead, "A Summary of Aluminum Combustion," NATO Research and Technology Organisation, 2004.

[84] T. Bazyn, H. Krier and N. Glumac, "Evidence for the transition from the diffusion-limit in aluminum particle combustion," in *Proceedings of the Combustion Institute*, Heidelberg, 2007.

[85] J. R. Carney, J. M. Lightstone, T. P. McGrath II and R. J. Lee, "Fuel-Rich Explosive Energy Release: Oxidizer Concentration Dependence," *Propellants, Explosives, Pyrotechnics,* vol. 34, no. 4, pp. 331-339, 2009.

[86] M. Tischler, "High Accuracy Temperature and Uncertainty Calculation in Radiation Pyrometry," *Metrologia,* vol. 17, pp. 49-57, 1981.

[87] P. B. Coats, "Multi-Wavlength Pyrometry," *Metrologia,* vol. 17, pp. 103-109, 1981.

[88] I. Bonefacic and P. Blecich, "Two-Color Temperature Measurement Method Using BPW34 Pin Photodiodes," *Engineering Revieww,* vol. 35, no. 3, pp. 259-266, 2015.

[89] E. W. Spisz, A. J. Weigund, R. L. Bowmun and J. R. Juck, "Solar Absorbances and Spectral Reflectances of 12 Metals for Temperatures ranging from 300 to 500 K," NASA Technical Note, Clevland, 1969.

[90] M. Quazi, M. Fazal, A. Haseeb, F. Yusof, H. Masjuki and A. Arslan, "Laser-based Surface Modifications of Aluminum and its Alloys," *Critical Reviews in Solid State and Materials Sciences ,* vol. 41, no. 2, pp. 106-131, 2015.

[91] R. F. Tate, B. T. Anderson, P. B. Keating and G. D. Hager, "Diode-laser Zeeman Spectroscopy of Atomic Iodine," *Journal of the Optical Society of America,* vol. 17, no. 7, pp. 1271-1278, July 2000.

[92] V. S. Zuev, V. A. Katulin, V. Y. Nosach and O. Y. Nosach, "Investigation of the Luminescence Spectrum of Atomic Iodine," *Journal of Experimental and Theoretical Physics,* vol. 35, no. 5, pp. 870-873, November 1972.

[93] T. D. Padrick and R. E. Palmer, "Pressure Broadening of the Atomic Iodine 5^2P_1/2-5^2P_3/2 Transition," *Journal of Chemical Physics,* vol. 62, no. 8, pp. 3350-3352, April 1975.

[94] A. Kramida, Y. Ralchenko, J. Reader and NIST ASD Team, "NIST Atomic Spectra Database (ver. 5.5.1)," 2017. [Online]. [Accessed 22 December 2017].

[95] M. Simeckova, D. Jacquemart, L. S. Rothman, R. R. Gamache and A. Goldman, "Einstein A-coefficients and statistical weights for molecular absorption transitions in the HITRAN database," *Journal of Quantitative Spectroscopy and Radiative*

Transfer, vol. 98, pp. 130-155, 2006.

[96] M. D. Clemenson, *Dissertation,* University of Illinois at Urbana-Champaign, 2015.

[97] P. Speitz, J. C. Gomez Martin and J. P. Burrows, "Spectroscopic Studies of the I2/O3 Photochemistry Part 2. Improved Spectra of Iodine Oxides and Analysis of the IO Absorption Spectrum," *Journal of Photochemistry and Photobiology A: Chemistry,* vol. 176, pp. 50-67, 2005.

[98] M. E. Tucceri, D. H. lscher, A. Rodriguez, T. J. Dillon and J. N. Crowley, "Absorption Cross Section and Photolysis of OIO," *Physical Chemistry Chemical Physics,* vol. 8, pp. 834-846, 2006.

[99] J. M. Peuker, P. Lynch, H. Krier and N. Glumac, "On AlO Emission Spectroscopy as a Diagnostic in Energetic Materials Testing," *Propellants, Explosives, and Pyrotechnics,* vol. 38, no. 4, pp. 577-585, 2013.

[100] C. P. CG and J. Hornkohl, "Computation of AlO B2Σ+ → X2Σ+ emission spectra.," *Spectrochim Acta A Molecular Biomolecular Spectroscopy,* vol. 18, no. 1, pp. 404-411, 2011.

[101] C. Murzyn, *Masters Thesis: Experimental study of the interaction between aluminum and hydrogen fluoride in biocidal explosions,* Urbana: University of Illinois at Urbana Champaign, 2016.

[102] R. SKAGGS, R. DANIEL, A. MIZIOLEK, K. McNESBY, C. HERUD, W. R. BOLT and D. HORTON, "Diode Laser Measurements of HF Concentrations From Heptane/Air Pan Fires Extinguished by FE-36 And FE-36 PlusAmmonium Polyphosphate," in *Proceedings of the International Society for Optical Engineering: Photonics East,* 1999.

[103] G. B. Rieker, *Doctoral Dissertation: Wavelength Modulation Spectroscopy for Measurments of Gas Temperature and Concentration in Harsh Environments,* Stanford University, 2009.